
Transport phenomena in metal-halide lamps
a poly-diagnostic study

Tanya Nimalasuriya

Copyright © 2007 by T. Nimalasuriya

Printed by PrintPartners Ipskamp, Enschede.

This research was financially supported by the Dutch Technology Foundation STW (project ETF. 6093)

CIP-DATA LIBRARY TECHNISCHE UNIVERSITEIT EINDHOVEN

Nimalasuriya, Tanya

Transport phenomena in metal-halide lamps : a poly-diagnostic study / by Tanya Nimalasuriya.
- Eindhoven : Technische Universiteit Eindhoven, 2007. Proefschrift.

ISBN 978-90-386-1169-3

NUR 926

Trefw.: plasmafysica / gasontladingen / gasontladingslampen / lichtbronnen /
plasmadiagnostiek / spectroscopie.

Subject headings: gas discharges / metal-halide lamps / plasma diagnostics / plasma properties
/ x-ray fluorescence analysis / x-ray absorption / optical emission spectroscopy.

**TRANSPORT PHENOMENA
IN METAL-HALIDE LAMPS
A POLY-DIAGNOSTIC STUDY**

PROEFSCHRIFT

ter verkrijging van de graad van doctor aan de
Technische Universiteit Eindhoven, op gezag van de
Rector Magnificus, prof.dr.ir. C.J. van Duijn, voor een
commissie aangewezen door het College voor
Promoties in het openbaar te verdedigen
op dinsdag 18 december 2007 om 16.00 uur

door

Tanya Nimalasuriya

geboren te Amsterdam

Dit proefschrift is goedgekeurd door de promotoren:

prof.dr. J.J.A.M. van der Mullen
en
prof.dr.ir. M. Haverlag

Copromotor:
dr.ir. W.W. Stoffels

Contents

1	General Introduction	1
1.1	Gas Discharge lamps	2
1.1.1	Low-pressure discharge lamps	3
1.1.2	High pressure discharge lamps	3
1.2	The metal-halide lamp	4
1.2.1	General principles of operation	5
1.2.2	Influence of metal-halides in the discharge	6
1.2.3	Colour separation in the metal-halide arc lamps	7
1.3	Scope of Thesis	11
1.4	Thesis outline	12
1.5	The lamps	13
2	Radially resolved atomic state distribution functions of Dy and Hg	19
2.1	Introduction	20
2.2	Theory	22
2.2.1	The atomic state distribution function	22
2.2.2	The absolute line intensity	25
2.3	Experimental setup	26
2.4	Results and discussion	27
2.5	Conclusions	32
2.6	Acknowledgements	33
2.7	Measured lines and corresponding A values	33
3	Metal-halide lamps in the international space station	37
3.1	Introduction	38
3.2	Theory	39
3.2.1	Segregation	39
3.2.2	Emission of radiation	40
3.3	Experimental Setup	42
3.4	Results and Discussion	45
3.5	Conclusions	51
3.6	Acknowledgements	55

4	Metal-halide lamps under hyper-gravity conditions	59
4.1	Introduction	60
4.2	Theory	61
4.2.1	Segregation	61
4.2.2	Axial segregation	62
4.2.3	Emission of radiation	63
4.3	Experimental Setup	65
4.4	Results and discussion	67
4.5	Conclusions	70
4.6	Acknowledgements	74
5	Metal-halide lamps at microgravity, experiments and model	77
5.1	Introduction	78
5.2	De-mixing	79
5.3	The experiment	81
5.4	The model	82
5.4.1	Geometry of the problem	83
5.4.2	Basic equations	83
5.5	Results and discussion	87
5.6	Conclusions	94
6	X-ray induced fluorescence measurement of segregation	101
6.1	Introduction	102
6.2	Theory	103
6.3	The experiment	107
6.3.1	The Lamp	107
6.3.2	X-ray induced fluorescence	107
6.4	Results and Discussion	108
6.5	Conclusions	116
6.6	Acknowledgements	116
7	X-ray absorption of the mercury distribution in metal-halide lamps	119
7.1	Introduction	120
7.2	Theory	121
7.2.1	Image processing and reconstruction	121
7.2.2	Fitting procedure	123
7.2.3	Tikhonov regularized Abel inversion	126
7.3	Experimental setup	127
7.3.1	X-ray source	128
7.3.2	CCD camera	129
7.3.3	The lamp	129
7.4	Results and Discussion	129
7.4.1	Beam-hardening	130

7.4.2	Tikhonov regularisation parameter μ	131
7.4.3	Scattering of x-rays	132
7.4.4	Temperature distribution	133
7.5	Conclusions	135
7.6	Acknowledgments	135
8	X-ray absorption of the mercury distribution in a commercial metal-halide lamp	139
8.1	Introduction	140
8.2	Theory	141
8.3	Experimental setup	142
8.3.1	The lamp	143
8.4	Results and Discussion	143
8.5	Conclusions	149
8.6	Acknowledgments	151
9	Conclusions	155
9.1	Introduction	155
9.2	Overview of the thesis	155
9.2.1	Optical emission spectroscopy	155
9.2.2	Comparison with the numerical model	157
9.2.3	X-ray diagnostics for MH lamps	158
9.2.4	LTE validation	159
9.3	General outlook	160
	Summary	163
	Related publications	165
	Acknowledgements	169
	Curriculum Vitae	171

General Introduction

Life without light is unimaginable.

In these modern times artificial light allows us to extend our activities, such as working, travel and entertainment, beyond the daylight hours. Factories and office buildings are designed with no possibility of ever being adequately illuminated by daylight. Worldwide communication would be impossible if half the world could not dispel the darkness by turning on the light at the flick of a switch.

Turning on the light comes at a price. In fact, the biggest item of cost in producing light is the cost of electric power needed to operate the lamp. Worldwide about 20% of all electricity is used for lighting, making power efficiency one of the most important criteria for lamp design [1]. A second, almost as important, criterium is the aspect of colour rendering, which measures the ability of the light source to reproduce the colours of the illuminated object. The goal of colour rendering is to make the illuminated objects look as natural (i.e. as in daylight) as possible. A third important criterium in lamp design is the stability of the light source.

The search for a lamp that meets with all these criteria led to the the development of the high intensity discharge lamp (HID lamp). These are lamps that have high pressure (over 1 bar), small volume, high luminance and contain, in most cases, either mercury and/or sodium. A class of HID lamps are formed by the metal-halide lamps. These are high pressure mercury lamps containing one or more metal salts that produce a brilliant white light. They can display a power efficiency of nearly 40% which is quite staggering compared to the mere 4-6% of the incandescent lamp. This type of lamp seems to embrace all of the requirements mentioned above.

Unfortunately, the metal-halide lamp has certain issues that need to be dealt with such as instability, the need to operate the lamp in different orientations, and inhomogeneous colour. Complex transport phenomena result in non-uniformity of colours when the lamp is operated vertically. The lamp shows a bluish-white mercury discharge at the top of the lamp and a much brighter and whiter discharge from the additives at the bottom of the lamp [2]. Segregation of colours, or de-mixing, causes the illumination of an object to

result in strange colouring of the object, making the object look different than it really is. It also has a negative effect on the lamp's power efficacy. In order to improve these lamps the de-mixing phenomenon needs better understanding.

The research presented in this thesis aims at making a contribution to the ongoing process of understanding the fundamental processes going on in the metal-halide discharge lamp. This is expected to lead to an improvement of lamp design in terms of efficiency and colour rendering.

1.1 Gas Discharge lamps

Nearly all lamps that are used for general illuminating purposes are based on plasma technology. The exceptions are the highly inefficient incandescent (halogen) lamps and the relatively new LED's. The latter may, in the near future, prove to be a good alternative in some cases, especially as a replacement for incandescent and possibly fluorescent lamps. However, even if LED technology is advancing as rapidly as predicted, electrical discharges will have to supply the major share of light sources for at least another two decades [3] [4] [5]. In any case it is expected that the gas-discharge lamps are mostly qualified for the general illumination of large areas such as sports arenas, buildings and roads.

One of the major developments in the last century within the lamp industry is realized by the introduction of the gas discharge lamp. A unique advantage of the gas discharge lamp is the ability to select the atoms that radiate in the visible part of the spectrum. Combined with the fact that discharges radiate from regions with much higher temperature, a much higher efficiency can be reached than with the solid filament of the incandescent lamp. Another advantage of gas discharge lamps with respect to the incandescent lamp is that they can have a much longer lifetime.

The principle of a gas discharge lamp is based on the conversion of electric power into radiation by means of an electrical discharge in the gas medium in the lamp. In such lamps a weakly or moderately ionized plasma is created. A plasma is an ionized gas and consists of electrons, ions, neutrals and excited particles and is on average neutral. The gas is located, in general, in a discharge tube with two electrodes. [6]

The basic process that occurs in the discharge can be described as follows. The electrons are accelerated by an externally imposed electric field, their directed velocity will be scattered into random directions by elastic and inelastic collisions with heavy particles. The result of this ohmic heating is a high electron temperature. In the case of inelastic collisions, part the kinetic energy of the electrons is transformed into the internal energy of atoms. These inelastic collisions are essential for chemical processes, such as excitation, ionization and dissociation and the generation of radiation. The internal energy of the atoms is released as electromagnetic radiation as the atoms relax back to their lower energy states.

Generally, two groups of discharge lamps can be distinguished: low pressure and high pressure discharge lamps. Low pressure discharge lamps have a pressure of below 10^{-3} bar, are generally large in volume, low in luminance and power densities and the plasma

conditions in these lamps are far from equilibrium. High pressure discharge lamps generally have a small volume (a few mm³ or cm³), high pressure (more than 1 bar), high luminance, a large variety in power settings (10 W to 18 kW) while the plasma in these lamps are close to local thermal equilibrium (LTE). Due to their high intensity these lamps are often denoted by high intensity discharge (HID) lamps. [7]

Also, the energy transformation of the electrons, obtained from the electric field between the electrodes, into excitation, ionisation or dissociation of atoms or molecules and heat, is different in low-pressure and high-pressure discharge lamps. [7]

1.1.1 Low-pressure discharge lamps

In low pressure discharge lamps, the interaction frequency of electrons with heavy particles is low so that the electrons can attain a high temperature while the heavy particles, being in contact with the wall, remain relatively 'cool'. The most probable excitations are from the ground-state to the first excited states. These excited atoms emit resonance radiation. [7] The optimum pressure of metal vapour is around 1 Pa in low-pressure discharge lamps, but additionally a buffer gas with a high ionisation energy is added in order to contain the electrons and reduce the degradation of the electrodes.

In many cases mercury is the metal of choice since it has a high vapour pressure and can be easily excited. It generates light in the UV (254 nm and 185 nm), which can be converted into white visible light by phosphors, which is the case with the tubular fluorescent tube and its cousin the compact fluorescent lamp. Mercury is a highly efficient radiator, but half the photon energy is lost in the phosphor where a UV photon is converted into a visible one. Low pressure sodium lamps has a slightly lower efficiency, but the sodium resonant line at 590 nm coincides with the maximum sensitivity of the eye-sensitivity curve. Therefore no phosphors are needed, yielding a very efficient lamp, which unfortunately is monochromatic and thus of limited use. The application of the low pressure sodium lamp is restricted to road lighting, where colour distinction is considered to be less important [5].

In a low-pressure discharge lamp, the electron temperature is considerably higher than the heavy-particle temperature (temperature of atoms and ions). This is caused by the more effective energy gain of electrons compared to heavy particles in the discharge. The electric field accelerates ions and electrons, but the ions lose a substantial part of this kinetic energy at each elastic collision with another heavy particle due to the equal mass of the collision partners. The electrons lose only a very small percentage of their kinetic energy during elastic collisions with heavy particles due to the tremendous mass difference between electrons and heavy particles. Moreover, the electrons often excite atoms during inelastic collisions. If these excited atoms emit the energy as radiation, the kinetic energy of the atom does not increase, causing the heavy-particle temperature to stay low. [7]

1.1.2 High pressure discharge lamps

At a pressure higher than 1 bar the energy transformation process is different than for low pressure discharges. The mean free path of electrons decreases with increasing pressure,

which also increases the number of collisions. Although the electron passes only a small percentage of its kinetic energy to heavy particles during elastic collisions, the huge number of collisions ensures a considerable energy transfer from electrons to heavy particles. This results in an increasingly heavy-particle temperature with a simultaneously decreasing electron-temperature. In high pressure discharge lamps the electrons and heavy particles have temperatures between 1400 K and 8000 K. At these temperatures, the excitation of atoms is sufficiently high, resulting in radiation from transitions from excited states to the ground state and from excited states to other excited states. [7]

The resulting spectral power distribution of high-pressure discharge lamps consists therefore not only of resonance lines but also of spectral lines due to transitions between excited states. In fact, the resonance lines are even missing in high-pressure discharge lamps of sufficiently high pressure, because they are most probably reabsorbed in the outer regions of the plasma in the discharge tube. This is caused by the high density of metal atoms in high-pressure discharge lamps, which is even higher in the colder plasma regions. Since these atoms are mostly in the ground-state it is very likely that the absorption of resonance radiation takes place [7].

Typical high-pressure discharge lamps contain at least mercury or sodium. The advantage of sodium is, as with the low pressure discharge lamps, the wavelength of the resonance lines, which lie very close to the maximum of the sensitivity curve of the human eye. The advantages of mercury are the high vapour pressure, i.e. mercury is very volatile, and the high resistance of a mercury plasma due to the large cross-section for collisions between electrons and heavy particles. The latter makes it possible to operate the lamp on low currents and high voltages, which is desirable with respect to efficiency and also to low strain and long lifetime of the electrodes. The high pressure leads to large electric field strengths up to 600 V cm^{-1} . Thus high electrical power input into small discharge volumes is possible, which led to the development of the High Intensity Discharge (HID) lamp. [7]

Since the end of last century often metal-halide salts like TlI, NaI, DyI₃, HoI₃ etc are added to the mercury HID lamp in order to increase efficiency and colour properties. These lamps, containing both mercury and one or a combination of metal-halide salts, is called the metal-halide lamp.

1.2 The metal-halide lamp

In 1912 Charles Steinmetz was granted a patent [8] for a new light source. By adding small amounts of sodium, lithium, rubidium and potassium iodides he was able to modify the light output from 'an extremely disagreeable colour' to 'a soft, brilliant, white light'. It was not until much later, however, that a commercially viable lamp was produced along the same principles. In 1964 General Electric introduced a metal-halide lamp at the world trade fair in New York. [9]

Modern metal-halide lamps today operate under the same principles. They typically consist of a small burner about a centimeter in diameter and a centimeter or more in length surrounded by a larger protective outer bulb. The burner is made from poly-crystalline

alumina or quartz and is filled with noble gases, mercury (about 10 mg) and salt additives (a few milligram). Under operating conditions the mercury in the inner burner evaporates raising the pressure to several tens of bar. The advantages of metal-halide lamps remain much the same as in Steinmetz' original patent; they combine high luminous output across a broad spectrum of the visible range with good efficacy as compared to other light sources.

Despite all these advantages the growth in use of these lamps has been hampered by a number of limitations. For example the lamps can only be operated in a specified position e.g. vertically and when it can be operated in different orientations, the colour point is not the same. This non-uniform light-output reduces the design space for such lamps, and reduces its power efficiency. The lamp can become unstable which results in a disturbing flickering. It needs to cool down -the mercury vapour needs to condensate- before it can be re-ignited which is impractical in some cases. These limitations are caused by discharge physics, which is still relatively poorly understood. This section describes the principles of operation of metal-halide lamps, details the influence of the metal iodides and addresses the unwanted segregation of colours and how the study of these lamps under different gravity conditions can deepen our understanding of the complex transport phenomena and the overall energy balance of the lamp.

1.2.1 General principles of operation

The burner contains a rare gas for starting and a large quantity of mercury, acting as a buffer-gas, plus one or more of the additive metal-halides (usually iodides). In common with other HID lamps, the starting of metal-halide lamps has three distinct phases. First, the starting gas, usually a noble gas such as argon, is converted from a non-conductive to a conductive state. The inert gas is needed to start the lamp, because the vapour pressure of the mercury is too low at room temperature. The gas heats up the discharge tube to get the solid or liquid metal vaporised. This phase is rapidly followed by a period of anomalous glow discharge which heats the electrodes, producing the final phase of an arc discharge [6].

In operation, all of the mercury is vaporised, resulting in a high pressure, wall-stabilised arc at several bars of pressure. The additives also evaporate, additive molecules diffusing into the high temperature arc column, where they dissociate. The metal atoms are ionised and excited, giving off their characteristic myriad of spectral lines.

As metal atoms diffuse back to the walls, they encounter iodine atoms in the cooler gas near the walls and recombine to reform the iodide molecules. Because the average excitation potential of the metals (less than 4 eV) is much less than that of mercury (about 7.8 eV), the total power radiated in the added metal spectrum substantially exceeds that of the mercury spectrum, even though the mercury pressure is 100 times greater than the metal pressure. The spectrum, therefore, consists predominantly of the spectrum of the additives with the mercury spectrum superposed.

Because the additives show a considerable amount of lines distributed over the entire visible part of the spectrum, this in contrast to mercury whose spectrum contains almost no wavelengths longer than 579 nm, the metal-halide lamps have a vastly improved colour rendition over mercury lamps. Another advantage is the increase of luminous efficacy. For

a pure mercury arc only about 23 percent of the total radiation is in the visible part of the spectrum; in some of the iodide additives more than 50 percent of the total radiant energy can be visible. The net result is a lamp whose luminous efficacy can be over 120 lm/W whereas for mercury this is 55 lm/W. [1]

1.2.2 Influence of metal-halides in the discharge

Arc constriction

Unfortunately, additive metals may have an unwanted effect on the stability of the discharge. Metal additive atoms have many energy levels, a number of which are quite low-lying, so that the average excitation potential is quite low relative to the ionisation potential. This results in radiation loss near the flanks of the discharge, where most of the additive atoms are present, which then results in a contracted arc. This could give rise to constricted arc temperature profiles. Constricted arc profiles are poorly wall-stabilized. [10]

A wall-stabilized arc has a relatively steep temperature gradient at the wall. If the arc axis should move off centre toward one side, the temperature gradient on the other side would become less steep, resulting in less heat conduction loss, which would cause the temperature to rise in that region. The effect of the changes in the heat-conduction loss therefore partly cancel the initial motion of the arc column, thereby stabilising the arc against motion in the tube. [1]

However, the presence of sizeable quantities of metal additives in the arc can lead to constricted, poorly wall-stabilised arcs. A relatively large motion of the arc core in the tube causes little or no change in heat-conduction loss, and the walls exert no stabilizing influence on the arc. The arc position is therefore strongly affected by convection, turbulence, acoustic resonances, and (self-induced) magnetic forces. The arc of the lamp operated in vertical position can wander around periodically in the burner under the influence of convection currents, resulting in a flickering effect that is quite disturbing. The latter is also known as helical instability. Contraction of the arc is studied in various chapters of this thesis.

Arc broadening

Fortunately there are metals that can be added to the metal iodide arc that have exactly the opposite effect, they tend to broaden the arc. These are the alkali metal iodides: lithium, sodium, potassium, rubidium and cesium. The arc containing these species is wall-stabilized because of the larger diameter of the arc. [1]

The major effect of the alkali addition must be due to the low ionization potential of the alkali atom, which causes many more free electrons to be available in the low temperature region of the arc. The presence of these free electrons then allows for the electrical current flow, which leads to power dissipation and more heat generation in these low-temperature regions. This raises the temperature bringing about an increase in the diameter of the high temperature region of the arc and of the electrically conducting region. [1]

Radiation and absorption also influences the arc-broadening. Radiation emitted at the core is absorbed in the cooler outer regions of the discharge, adding to the energy to be dissipated as heat which causes the temperature to increase. Therefore, atoms with strong pressure-broadened resonance lines combining considerable absorption at the line core with considerable transport of energy in the line wings also have arc-broadening effects. For example, the addition of thallium iodide results in an increase in arc diameter because of radiation transport and absorption of the 377-nm thallium line [1]. Broadening of the arc is investigated in chapter 8.

The function of mercury in metal-halide lamps

It is not essential for the operation of the iodide cycle in a metal-halide lamp for mercury (Hg) to be present. However, there are several functions of mercury in the lamp mixture which are exceptionally useful.

1. Mercury makes it possible to achieve a high total pressure for operation while still having a low pressure at ignition, so that reasonable starting voltages can be obtained. Efficient operation of metal-halide lamps with a relatively high-pressure metal vapour requires a high total pressure filling to prevent rapid diffusion of dissociated metal and iodine atoms from the arc core to the tube wall. If dissociation took place primarily in the arc core and recombination took place primarily at the wall, the loss of energy due to the dissociation process would be very high, resulting in an inefficient lamp. [1]
2. An excess of mercury can react with excess iodine to form HgI_2 . If any free I_2 vapour is present in the lamp at ignition, starting voltages are very high. This is because the strong electron-attaching properties of I_2 interfere with the avalanche formation. The presence of mercury in excess then ensures that only HgI_2 is present at starting. Although HgI_2 is also an electron-attaching gas, its vapour pressure is substantially lower than that of I_2 and causes only a moderate increase in starting voltage. Another aspect of the HgI_2 is the effect on light emission. Excess iodine by itself tends to form I_2 near the walls and I_2 is strongly light absorbing. HgI_2 is relatively unstable and transparent. Excess iodine in the form of HgI_2 is as accessible as free iodine for preventing condensation of metals on the wall. [1]
3. Mercury has low thermal conductivity as opposed to alternatives such as zinc
4. Mercury causes the red flank of Na to broaden which results in a much better production of the colour red that is otherwise difficult to achieve.

1.2.3 Colour separation in the metal-halide arc lamps

Transport phenomena in metal-halide lamps: radial and axial segregation

A metal-halide lamp with colour separation has different colours along its axis. Figure 1.1(a) shows an example of colour separation in a lamp containing DyI_3 . Whereas the

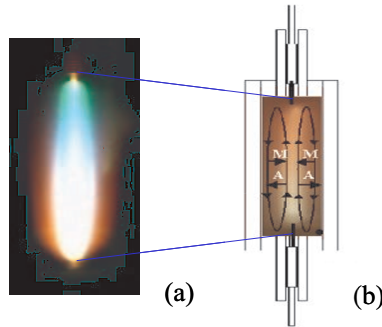


Figure 1.1: (a) Colour separation in an metal-halide lamp burner. The colours reproduced by the camera are not the actual colours, the top of the lamp is in fact bluish-white. (b) Schematic view of an metal-halide lamp; diffusion and convection of atoms (A) and molecules (M) are indicated by arrows.

bottom of the lamp is white with a reddish glow around it, the top is white-bluish. The cause is a complex interplay of diffusion and convection resulting in a non-homogeneous distribution of the radiating metals.

Let us concentrate on the radial direction and the role of diffusion. There are large temperature gradients across the radius of the lamp. Going from the wall at about 1200 K to the arc core at 6000 K metal-halide molecules will first dissociate and then ionize at the hot centre. The resultant density gradients cause strong diffusion fluxes, which are counteracted by the back-diffusion of other species: near the wall molecules diffuse inwards and atoms outwards, while near the centre atoms move inwards as the ions diffuse out. The diffusion speed of the molecules is significantly smaller than that of the atoms due to their size and mass difference. Ions and atoms have similar masses, but the ions at the centre diffuse faster due to ambipolar diffusion. In a steady state with equal in and outward fluxes, a lower speed is balanced by a higher partial pressure. The total effect is called radial segregation and results in a lowering of the partial metal pressure (in any chemical form) near the lamp centre [5].

In addition to diffusion, there is also convection in the lamp. In vertically operating lamps, convection causes an upward flow in the hot central arc region, which returns downwards along the cooler walls. The minority metal species follow the dominant mercury convection flow. However, radial segregation causes the metal, that rises in the centre and diffuses outwards to the wall, to be dragged downwards. The combined effect of convection and radial segregation is a decreased metal density in the upper part of the lamp, see figure 1.1 (b). Such axial segregation results in a non-homogeneous emission, called colour separation.

Depending on the competition with diffusion, the convection flow can have two opposite effects on the axial segregation. For relatively small convection flows we will find that an increase in convection will cause an increase of the axial segregation. On the other hand, in case of a high convection flow, we find that a further increase reduces the axial segregation

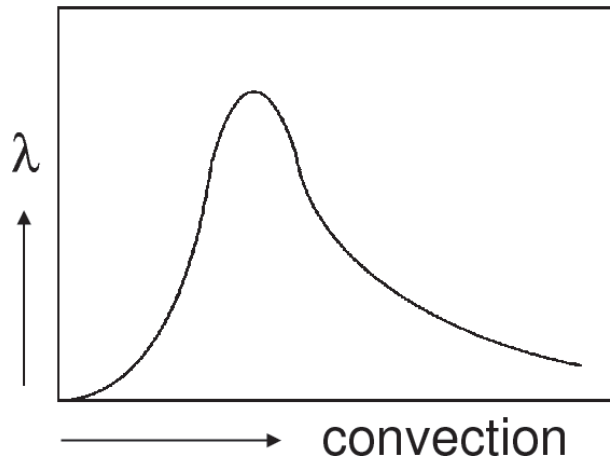


Figure 1.2: The Fischer curve [12] which represents the dependence of the axial segregation parameter λ on convection, or g .

as the species are better mixed in the lamp. By realizing that the convection is proportional to the total pressure it can be understood that there is one pressure for which the axial segregation reaches a maximum, see figure 1.2. Fischer characterized axial segregation with a segregation parameter λ such that [12]

$$p_{\{\alpha\}}(z) = p_{\{\alpha\}}(0) \exp(-\lambda_{\{\alpha\}}z), \quad (1.1)$$

where z is the axial position relative to the tip of the lower electrode and $\lambda_{\{\alpha\}}$ is called the segregation parameter for the element α .

Elemental density and elemental pressure

Elemental density is defined as the density that contains all molecular, atomic and ionic contributions of a particular element. For example, for element α (denoted with $\{\}$), the number density of a particular element n_{α} is the sum over all species containing that element,

$$n_{\{\alpha\}} = \sum_i R_{i\alpha} n_i \quad (1.2)$$

The stoichiometric coefficient $R_{i\alpha}$ counts the number of α -nuclei in the compound or species i . For example for DyI_3 the elemental density of Dy ($\alpha = \text{Dy}$) in a lamp containing DyI_3 can be described as

$$n_{\{\text{Dy}\}} = [\text{Dy}] + [\text{Dy}^+] + [\text{DyI}] + [\text{DyI}_2] + [\text{DyI}_3] + 2[\text{Dy}_2\text{I}_6] + 3[\text{Dy}_3\text{I}_9] + \dots \quad (1.3)$$

The stoichiometric coefficient of DyI_3 equals for Dy $R_{i\alpha}=1$, while for I $R_{i\alpha}=3$ for the molecule DyI_3 . The summation of equation 1.2 runs over all species. In an analogue way we can determine elemental pressure $p_{\alpha}=n_{\alpha}kT$, for Dy the elemental pressure $p_{\{\text{Dy}\}}=n_{\{\text{Dy}\}}kT$. Elemental densities are shown in chapter 6.

Gravity and segregation

Above we have seen that the axial segregation is caused by the combination of convection and diffusion. The convection is the result of gravity and thus directly related to the value of the free fall acceleration $g = 9.8 \text{ m/s}^2$. By varying the acceleration of the lamp the gravity conditions can be varied, making it possible to separate the role of either diffusion or convection in the segregation phenomenon. It is possible to create two extreme situations by varying the gravity conditions.

1. No convection. Under micro-gravity conditions, the convection velocity is very small so that diffusion is dominant. On top of the density decrease caused by the temperature, we are still able to observe radial de-mixing; i.e. the concentration of the radiating species will still be lower in the centre of the lamp as compared to the regions near the wall.

2. High convection. Under hyper-gravity conditions, the convection velocity increases so that the concentration of the additives in the lamp becomes well mixed; any radial de-mixing caused by diffusion will be eradicated by convection. This can be achieved by placing the lamp under high acceleration conditions.

Both micro- and hyper-gravity conditions were realized during parabolic free falls in an Airbus airplane of the European Space Agency (ESA). There the gravity varied between 0- g and 2- g . The lamps were designed such that de-mixing is at a maximum at 1- g . These experiments revealed that at both 0- g and 2- g de-mixing was dramatically reduced. However, the period (almost 20 s) of zero- g during parabolic flights is too short to stabilize the plasma.

It is therefore that the experiments were repeated at the international space station ISS where micro-gravity is sustained. The experiments were done in the week of April 24th, 2004 by the Dutch astronaut André Kuipers. The results of these experiments are shown in chapter 3. In order to create an environment of prolonged hyper-gravity and to enhance the dynamical range of the experiments to higher gravity values, a centrifuge was built that accelerates from 1 to 10 g . The results of these experiments are presented in chapter 4.

Experiment and model

It is currently beyond our capabilities to fully understand and model a commercial metal-halide lamp with complex shape and chemistry [12]. Therefore, the measurements have been performed on a reference lamp with simple geometry and chemistry. The absence of convection under micro-gravity conditions greatly simplifies the problem. The measurements reveal a great deal about lamp behaviour, which needs to be reproduced by any valid lamp model. Qualitatively the lamp behaviour is well understood and the measurements supply ample data for quantitative model validation. A comparison between experiment and model is presented and discussed in chapter 5. Obviously, changing gravity is not a practical solution, but it helps to identify how to optimize discharge parameters, so we can illuminate our world using less energy.

A simple model based on an assumed parabolic temperature profile and long aspect

ratios was published in [12]. More advanced models have since been made [15] [16]. A numerical model was constructed by Beks [14] that uses less assumptions on the nature of the discharge, calculating more of the lamp properties from first principles than earlier models. This model should calculate all essential properties self-consistently. This involves, amongst others, calculating the convection and diffusion of species throughout the discharge region, calculating the emission and absorption of light and accurately describing the energy balance in the lamp. To build this model we have at our disposal the plasma simulation package Plasimo [17] [18] developed at the Eindhoven University of Technology by a succession of graduate students and researchers over the past 15 years.

1.3 Scope of Thesis

The work presented in this thesis is aimed at obtaining a better understanding of the segregation phenomena in metal-halide lamps by means of experimental investigation. This PhD project is part of a larger project for the understanding of the energy balance of metal-halide lamps and the plasma transport processes that are responsible for segregation phenomena in these lamps. Qualitatively the mechanism is understood, but quantitatively the disagreement between theoretical models and experiment is often large. Therefore more in-depth studies are needed and quantitative data from experiments are required to validate models. The final goal is to set up a complete theoretical model to fully understand the energy balance and transport processes in such chemically complex plasmas. This grand model can then be used to design lamps with high efficiency and good colour rendering. The primary objective of this project is to use poly-diagnostic tools in order to study the plasma properties such as the density of species and temperature in the metal-halide lamp.

Metal-halide lamps contain a chemically complex discharge. The spectrum of such a discharge contains a myriad of lines. We have used Optical Emission Spectroscopy (OES) to analyse these lines which yielded, after calibration and inversion, the radially resolved atomic state distribution function (ASDF). The ASDF yields a wealth of information regarding the species distribution and temperature. It is assumed by most researchers that the discharge in these lamps are in local thermodynamic equilibrium (LTE). This implies that only one temperature field is needed to describe all the processes. However the important question remains whether this LTE assumption is valid or not. If LTE is not established, this would imply that the local chemical composition, the radiation generation and transport processes are determined by a multitude of temperatures. This would make the description of the system very complex. The validation of the LTE assumption requires different temperature measurements. The ASDF can give insight about a possible departure from LTE.

It is known from theory that segregation, which is governed by the competition between diffusion and convection, is strongly influenced by convection, and therefore gravity. It is therefore of great interest to study the lamp under various gravity conditions ranging from micro-gravity to hyper-gravity. At micro-gravity diffusion of species can be exclusively studied as there is no convection. At hyper-gravity convection dominates the transport of

species in the lamp. Previously the lamp was studied under the micro-gravity conditions of the space shuttle [19] [20] and under micro to hyper-gravity during parabolic flights [21]. The former experiments yielded no information regarding the density or temperature distribution, the latter did not have sustained gravity conditions for more than 20s, which is not enough to stabilize the arc.

In the research described in this thesis we used the gravity-free environment of the international space station ISS for the micro-gravity experiments and a centrifuge that imposes hyper-gravity of up to 10 g on the lamp. We have used optical emission spectroscopy to study segregation under these varying gravity conditions. The experiments yielded the major plasma parameters such as species distribution and temperature.

The absence of convection under micro-gravity conditions greatly simplifies the problem. The measurements reveal a great deal about lamp behaviour, which needs to be reproduced by any valid lamp model. Qualitatively the lamp behaviour is well understood and the measurements supply ample data for quantitative model validation. Modelling investigations were performed by Beks [14]; results of the comparison between experiment and model are included in this thesis.

It is of interest to study the discharge with x-ray techniques that allow for measurements anywhere in the lamp, in contrast to optical methods which are limited to the core or regions close to the core. Two types of x-ray technique were used: x-ray induced fluorescence (XRF) and x-ray absorption spectroscopy (XRA).

An extensive quantitative study of the arc constituents was done by means of x-ray induced fluorescence (XRF). Synchrotron radiation from the Advanced Photon Source of the Argonne National Laboratory was used to excite fluorescence of the various species of the discharge, allowing for the direct measurement of the elemental densities, some of which are optically inaccessible.

The primary observable of the XRA is the Hg density distribution, which by means of the ideal gas law $p = nkT$ can be translated into a heavy-particle temperature distribution (assuming isobaric conditions). XRA has very high spatial resolution which is very important in these lamps because of the fact that the discharge has a very steep temperature gradient. The comparison of the gas temperature with the electron (excitation) temperature as deduced from OES measurements gives insight in potential deviations from LTE.

1.4 Thesis outline

In order to obtain a large amount of data that can be used for both model validation and cross-comparison among the individual experiments, a poly-diagnostic approach was chosen for the lamp experiments.

OES is performed on lamps under normal- micro- and hyper-gravity conditions. Also a comparison is made between the modelling investigations done by Beks [14] and the micro-gravity results. The lamp is also investigated using x-ray techniques that can penetrate all parts of the lamp, namely XRF and XRA. XRF was used to measure the spatial

distributions of the arc constituents. XRA was used to determine the temperature profile. Lamps containing different types of lamp filling are also studied by XRA.

Chapter 2 deals with OES at normal-gravity. Here the spectrum of the metal-halide lamp in question is introduced and after intensity calibration and radial transformation the ASDF, which provides the density distribution of the atoms, ions and electrons of Dy and Hg, is constructed. A comparison is made between different data-sets for the transition probabilities. The validity of LTE is briefly investigated.

Chapter 3 deals with the study of segregation at micro-gravity. It is clear that no axial and only radial segregation exists in a micro-gravity environment. Density distributions of atoms and ions at different powers are shown, together with temperature profiles. A comparison is made between the measurements done at normal and micro-gravity. For this purpose temperature profiles, intensity and concentration profiles are compared at different lamp powers.

Chapter 4 is a follow up of the micro-gravity experiments and deals with hyper-gravity. The lamp and OES setup are placed in a rotating gondola. The resultant gravity can be varied continuously from 1 to 10 g. The result of the increased gravitational acceleration is an enhanced convection flow within the lamp. Webcam images are presented that clearly show the behaviour of the discharge at increased gravity. Line-of-sight intensity profiles are used to investigate the effects of the increase in gravity. The results are used to recreate the curve produced by the theoretical model of Fischer.

The results of the micro-gravity experiments from chapter 3 are compared with modelling investigations of Beks [14]. The density and temperature profiles together with the concentration profiles are compared. This can be found in chapter 5.

Chapter 6 shows the results from the XRF measurements of the arc constituents Hg, Dy and I. A simplified theoretical description of radial fluxes is presented and is used for the comparison between the OES and the XRF results.

Chapter 7 shows temperature profiles measured with XRA with an improved data analysis that shows dramatically different results from experiments reported previously by Zhu [13]. Comparisons are made between the temperature distribution obtained with OES and XRA.

Lamps with different fillings which include NaI, TII, Dy₃ and a commercial lamp containing a combination of these are measured with XRA and presented and discussed in chapter 8.

1.5 The lamps

Because of the need to simplify the complex commercial metal-halide lamp for the experiment and model, almost all the measurements have been performed on a reference lamp [22] with a simple geometry and chemistry, see figure 1.3. Table 1.1 shows the various lamps and lamp geometries and the various experiments that used them. All burners were made of quartz except for the XRA experiments in chapter 8 (XRA II), here PCA burners were used, see figure 1.4.



Figure 1.3: A COST reference lamp [22] used for most experiments in this thesis. The burner is made of quartz



Figure 1.4: One of the lamps used for the XRA experiments. This type of lamp has either quartz COST burners (as in chapter 7) or PCA burners (as in chapter 8 and depicted here). The outer bulb geometry for both chapter 7 and 8 is the same.

Experiment	D_{in}	D_{out}	L_{arc}	m_{Hg}	salt	power	chapter
OES normal- <i>g</i>	8	20	18	10	DyI ₃	100	2
OES micro- <i>g</i>	8	20	18	10	DyI ₃	70-150	3,5
OES micro- <i>g</i>	8	20	18	10	-	70-150	3,5
OES hyper- <i>g</i>	8	20	18	5, 7.5, 10	DyI ₃	130	4
OES hyper- <i>g</i>	4	20	20	0.75, 2.5	DyI ₃	130	4
XRF	8	20	18	10	DyI ₃	145	6
XRA I	8	120	18	10	DyI ₃	145	7
XRA I	8	120	18	10	-	145	7
XRA II	8	120	18	10	DyI ₃ , TII, NaI, mix	70	8

Table 1.1: Lamps used for this study. The diameters D_{in} and D_{out} are inner and outer diameter and are given in mm. The arc length L_{arc} is also given in mm. The power is given in W and the Hg mass in mg. Wall thickness of both burner and jacket is 1 mm, except for the PCA burners in chapter 8 that have a thickness of 0.55 mm. All lamp burners are shaped as cylinders.

Bibliography

- [1] J. Waymouth, *Electric discharge lamps*, MIT press, Cambridge, 1971
- [2] Zollweg R J, 1975 IES J. **4** 12-18
- [3] Solid-State Lighting Research and Development Portfolio, Navigant Consulting, 2006
- [4] M. Krames, *Progress in High power light-emitting diodes for solid state lighting*, Proc. 11th Int. Symp on the Science and Technol. of Light Sources, May 2007, Shanghai, ed. M.Q. Liu and R. Devonshire, p571-573
- [5] Stoffels W W, Nimalasuriya T, Flikweert A J, Mulders H C J, 2008 Plasma physics and controlled fusion, special issue, invited papers form the 34th european physical society conference on plasma physics, Warsaw, Poland, 2-6 July 2007, accepted for publication.
- [6] Coaton J R, Marsden A M, *Lamps and Lighting*, Arnold, London, 4th edition, 1997
- [7] Flesch P, *Light and light sources High intensity discharge lamps*, Springer-verlag, Berlin Heidelberg, 2006
- [8] Steinmetz C P, *Means for producing light* , U.S. Patent 1 025 932, 1902.
- [9] Beks M L, van Dijk J, Hartgers A, van der Mullen J J A M, IEEE *accepted for publication*
- [10] Elenbaas W 1951 *The high pressure mercury vapour discharge*, 1st ed., (North-Holland publishing company)
- [11] Fischer E 1978 *Influences of External and Self-Magnetic Fields on the behaviour of discharge lamps*, Philips GmbH Forschungslaboratorium Aachen Lobornotiz nr 13/78.
- [12] Fischer E, 1976 J. Appl Phys. **47** 2954
- [13] X. Zhu *Active spectroscopy of metal-halide lamps* PhD Thesis Eindhoven University of Technology (2005)
- [14] Beks M L, Hartgers A, van der Mullen J J A M, 2006 JPhysD **39** 4407
- [15] Dakin J T *et al* 1989 J. Appl. Phys. **66** 4074
- [16] Hashiguchi S, Hatase K, Mori S and Tachibana K 2002 J. Appl Phys. **92** 45
- [17] Benoy D A, 1993 *Modelling of Thermal Argon Plasmas* PhD Thesis Eindhoven University of Technology, the Netherlands
- [18] van Dijk J 2001 *Modelling of plasma light sources* PhD Thesis Eindhoven University of Technology, the Netherlands

- [19] Bellows A H, Feuersanger A E, Rogoff G L, and Rothwell H L, 'HID convection studies: a space shuttle experiment,' 1984 Illuminating Engineering Soc. Meeting
- [20] Bellows A H, Feuersanger A E, Rogoff G L, and Rothwell H L, 'Convection and Additive segregation in High pressure lamp arcs: Early results from a space shuttle experiment,' 1984 Gaseous electronics Conf., 1985 Bull. Amer. Phys. Soc. Vol **30**, p 141
- [21] Flikweert A J, van Kemenade M, Nimalasuriya T, Haverlag M, Kroesen G M W and Stoffels WW 2006 J.Phys.D **39**, 1599
- [22] Stoffels W W, Flikweert A J, Nimalasuriya T, van der Mullen J J A M, Kroesen G M W, Haverlag M, 2006 Pure Appl. Chem. **78** No 6
- [23] J.A.M. van der Mullen, Phys. Rep. **191** 109 (1990)
- [24] Curry J J, Sakai M and Lawler J E 1998 J. Appl. Phys. **84**, 3066
- [25] Lister G G, Lawler J E, Lapatovich W P and Godyak V A 2004 Rev. Mod. Phys. **76**, 541
- [26] Stoffels W W, Haverlag M, Kemps P C M, Beckers J and Kroesen G M W 2005 Appl. Phys. Lett. **87** 1
- [27] Mitchner M and Kruger Jr C H 1973 *Partially ionized gases* ,1st ed., (John Wiley and Sons).
- [28] Flikweert A J, Nimalasuriya T, Stoffels W W, Kroesen G M W 2007, PSST **16** 606

Optical emission spectroscopy of metal-halide lamps: Radially resolved atomic state distribution functions of Dy and Hg

Abstract. Absolute line intensity measurements are performed on a metal-halide lamp. Several transitions of atomic and ionic Dy, and atomic Hg are measured at different radial positions from which we obtain absolute atomic and ionic Dy intensity profiles. From these profiles we construct the radially resolved Atomic State Distribution Function (ASDF) of the atomic and ionic Dy and atomic Hg. From these ASDFs several quantities are determined as a function of radial position, such as the (excitation) temperature, the ion ratio Hg^+/Dy^+ , the electron density, the ground state and total density of Dy atoms and ions. Moreover, these ASDFs give us insight about the departure from equilibrium. The measurements show a hollow density profile for the atoms and ionization of atoms in the centre. In the outer parts of the lamp molecules dominate.

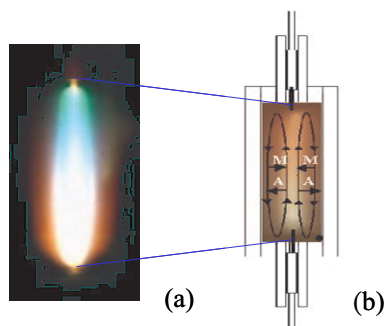


Figure 2.1: (a) Colour separation in a metal-halide lamp burner. (b) Schematic view of a metal-halide lamp; diffusion and convection of atoms (A) and molecules (M) are indicated by arrows. See figure 1.1 for full colour.

2.1 Introduction

The search for a compact high-intensity light source with high luminous efficacy and good colour rendering properties has led to the development of the metal-halide lamp [1]. This type of lamp contains a buffer gas of Hg and a relatively small amount of a mixture of additives such as Dy, Ce or Na salts, these act as the prime radiators. More than two salt components are necessary for a good color rendering index, therefore mixtures such as (NaI + ScI₃), (NaI + TlI + InI) or (NaI + TlI + DyI₃ + HoI₃ + TmI₃) are commonly used in the metal-halide lamp. Because of radial diffusion and convection these additives are non-uniformly distributed over the lamp resulting in the undesirable segregation of colours [2], see figure 2.1. In this study a lamp with an Hg buffer gas and one salt, namely DyI₃, is used. This lamp has a relatively simple salt system and therefore the results are easier to compare with a numerical model. Transport phenomena in this chemically complex plasma are not yet fully understood.

The aim of this work is to improve understanding of the plasma properties and transport phenomena in this type of lamps. The lamp is investigated using absolute line intensity measurements. The intensity of the lines are calibrated using a ribbon lamp with known spectral radiance. The spectrum of Dy contains a large abundance of lines, see figure 2.2, making wavelength calibration a complicated task. After intensity and wavelength calibration, these measurements yield absolute radial density distributions of several excited states of the additive Dy and the buffer gas Hg. From these the atomic state distribution functions (ASDF) are constructed for atomic and ionic Dy; and atomic Hg. From the ASDF several plasma properties can be determined such as the temperature, the ground state densities and the electron density. Moreover, the results may give an indication of a departure from equilibrium. This could be induced, for example, by transport phenomena such as segregation.

The few milligrams of the DyI₃ additive do not entirely evaporate leaving a liquid salt pool at the coldest spot of the burner wall. The cold spot determines the vapour pressure

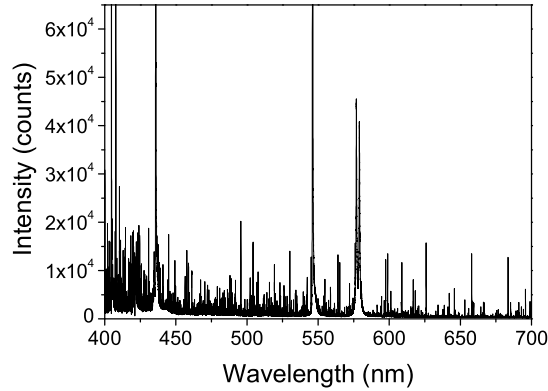


Figure 2.2: Spectrum of a metal-halide lamp containing Hg as a buffer gas and the additive DyI_3 . The saturated lines are Hg.

of the additive in the immediate vicinity of the salt pool. Because of the large temperature gradient between the wall (~ 1200 K) and the centre of the burner (~ 6000 K) [3] a multi-step process of dissociation of DyI_3 molecules towards the centre and association of atoms into molecules near the wall takes place. The reaction chain can be described as follows, increasing with temperature to the right,



At the hot center Dy atoms ionize and Dy ions are created,



Two mechanisms influence the distribution of particles in the plasma. First, there is a high temperature in the centre rapidly decreasing toward the wall, because of $p = nkT$, this results in a hollow profile of the mass distribution over the lamp. Second, there is the difference between the diffusion velocities of the atoms and molecules. The smaller and lighter Dy atoms diffuse faster than the larger and heavier molecules (DyI , DyI_2 , DyI_3). This difference in diffusion velocity results, in a steady-state, in an even more hollow profile of the elemental density of Dy; this is called radial segregation. Elemental density includes contributions from all molecular, atomic and ionic species of a particular element.

Convection in the lamp causes the hot gas to move upwards in the centre of the arc and downwards along the cool wall. This movement drags the high concentration of Dy near the wall downwards resulting in a high density of elemental Dy in the bottom of the arc. This is called axial segregation [2]. The combination of axial and radial segregation is shown in figure 2.1(b).

This chapter is organized as follows, section 2.2 deals with the theory of the atomic state distribution function and the absolute line intensity. Section 2.3 deals with the lamp

and the experimental setup used for the optical emission spectroscopy measurements. In section 2.4 the atomic state distribution function for different radial positions and its derived quantities are presented and discussed. It includes the radial density profiles of Dy atoms, ions and Hg atoms, and the radial profiles of electron density and temperature. We also study the effects of the large presence of Hg on the plasma.

Results of this work will aid the validation of the numerical models meant to simulate transport phenomena in metal-halide lamps.

2.2 Theory

2.2.1 The atomic state distribution function

A plasma region is said to be in Local Thermal Equilibrium (LTE) when, at a certain specific location, all the material particles are in equilibrium with each other. This means that for any collisional reaction the number of forward processes equals that of the corresponding backward processes [4]. However, photons can in principle escape from a plasma region in LTE, therefore emission is not necessarily compensated by the inverse process of absorption. By measuring the intensity of light-emitting atoms and ions, the density of these species can be determined, in case of optically thin lines. When in LTE, the atomic state distribution functions (ASDF) can be constructed from the density, these obey the distribution function as described by Boltzmann and Saha [4].

Another aspect of LTE is that the kinetic temperature of the electrons is the same as that of the heavy particles, i.e. $T=T_e = T_h$.

Figure 2.3 gives a sketch of the ASDF in LTE of two subsequent systems. Such a graph is expected for the atomic state distribution function (ASDF) of the atomic and ionic system of the additive in the lamp. It can be expressed by the Saha equation [5]

$$\eta_p = \eta_e \eta_r^+ \left(\frac{h^2}{2\pi m_e k T} \right)^{3/2} \exp(I_{pr}/k_B T), \quad (2.3)$$

where m_e , k , T_e , are the mass of the electron, the Boltzmann constant and the electron temperature respectively. I_{pr} is the energy difference between the atomic level p and ionic level r . In case of $r = 1$, which is the ground level of the ionic system, we have $I_{p1} \equiv I_p$, where I_p is the ionization energy. η_p is the corresponding state density defined as $\eta = n/g$, the number density n of an atom in a level p divided by the statistical weight g of that level. In the same way we can define $\eta_r^+ = n_r^+/g_r^+$, the state density of the ion and the state density of the free electron $\eta_e = n_e/g_e$ where $g_e = 2$, the number of the spin states of the free electron. When we use the Saha equation to find the relation between the atomic and the ionic ground state in Dy we need to insert the ionization potential of atomic Dy which equals $I_p = 5.93$ eV.

Two atomic levels that are in Saha relation with the ionic ground state are related to each other by Boltzmann's law, see figure 2.3. This can be understood by applying the

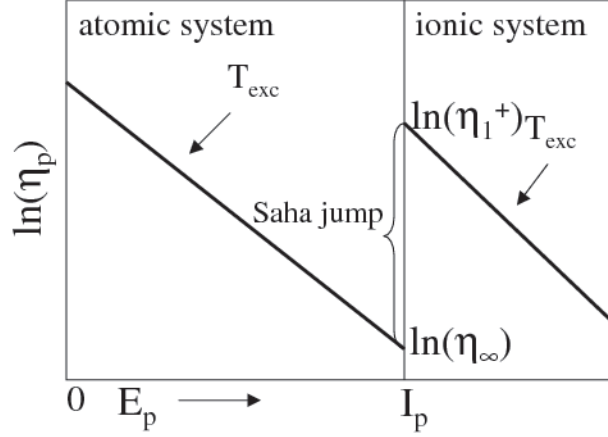


Figure 2.3: The ASDF of two subsequent atomic stages of one element (e.g. Dy) for a plasma in LTE. At the transition from the atomic to the ionic system the state density η shows a discontinuity. This is the so-called Saha jump and depends on the electron temperature and density, see equation 2.6. Note that there are two ways to indicate the energy position of an atomic level ‘p’, the excitation energy E_{1p} and the ionization potential I_{pr} . Going to the left along the energy axis I_{pr} will increase whereas E_{1p} decreases. [5]

Saha relation to two levels p and q and dividing the obtained expressions. This gives

$$\eta_q = \eta_p \exp(-E_{pq}/k_B T), \quad (2.4)$$

where $E_{pq} = I_p - I_q$, see figure 2.3. When the whole ASDF is consistent with Saha (and thus Boltzmann), the plasma region is said to be in Local Thermal Equilibrium [5].

We study the various features of the ASDF as shown in figure 2.3 with the aim to deduce essential plasma properties from it. Since figure 2.3 is a semi-log plot it is instructive to take the logarithm of the corresponding equation i.e. the Saha equation (2.3) which gives

$$\ln \eta_p = \frac{I_p}{k_B T} + \ln(\eta_\infty), \quad (2.5)$$

where

$$\eta_\infty = \eta_e \eta_1^+ \left(\frac{h^2}{2\pi m_e k_B T} \right)^{3/2}. \quad (2.6)$$

This near-continuum value of the atomic state density can be obtained by extrapolating η_p towards $I_p=0$. Other important densities are the atomic ground state density η_1 and the ionic ground state density η_1^+ . These can be obtained by extrapolating the ASDF towards $E_{1p}=0$ and $I_{p1}=0$ respectively.

The total ion density is found by taking the sum of all (excited) ions using the following expression:

$$n^+ = \sum_q n_q^+, \quad (2.7)$$

where

$$n_q^+ = \eta_1^+ g_q \exp\left(\frac{-E_q}{k_B T}\right), \quad (2.8)$$

where η_1^+ is the ionic ground state density. Rewriting equation 2.7 gives

$$n^+ = \eta_1^+ \sum_q g_q \exp\left(\frac{-E_q}{k_B T}\right) = \eta_1^+ Q(T). \quad (2.9)$$

$Q(T)$ is the partition function depending only on temperature and considered species [4]. The total atomic density of Dy can be calculated by means of the same expression in which the ionic ground state density is replaced by that of the atom and the partition function for the atom is used. In contrast to the Hg system, where we can replace the partition function by the g -value of the ground level ($g_1=2$) without loss of accuracy, the partition function must be taken into account for the Dy system. For instance the value for $Q(T)$ for Dy ions at $T = 5900\text{K}$ is 69 and for Dy atoms is 59 [12] whereas g_1 of Dy atoms and g_1 of Dy ions are 17 and 18 respectively.

We now introduce step-by-step how to extract information from the semi-log plot of figure 2.3.

1. The temperature value can be determined from the slope of the ASDF. This temperature can be indicated as the excitation temperature T_{exc} , which in LTE should be the same as the electron temperature T_e and heavy particle temperature T_h , see figure 2.3. Since we construct an ASDF for different species, namely Hg atoms, Dy atoms and ions, we will find T_{exc} values for each of these species. If the temperatures are equal to each other, within the estimated error margins, one of the necessary demands of the LTE assumption is satisfied.
2. By extrapolating the line in the atomic system toward the ground state (that is $E_{1p}=0$) we find the value of the atomic ground state density. As we can only measure the visible spectrum we cannot measure lines from low energy levels, therefore extrapolation is necessary.
3. By extrapolating the line in the atomic system toward the continuum (that is $I_p = 0$) we find the value of η_∞ . By extrapolating the line in the ionic system toward the continuum, we find the value of the ionic ground state η_1^+ , see figure 2.3.
4. The electron density n_e can be calculated from the Saha jump, which is the difference between the occupation of the highly excited state η_∞ and the ionic ground state η_1^+ . By determining η_∞ , η_1^+ (both by extrapolation) and T_e (from the slope), n_e can be calculated.

We recall that in a mixture, such as the composition of Hg and DyI_3 , the electrons present are supplied by both Hg and Dy, and are indistinguishable. Due to charge neutrality we may expect that the relation $n_e = n_i(\text{Hg}) + n_i(\text{Dy})$ holds. It will be shown that Hg is dominant in the lamp we studied.

The ionic ground state densities of Dy is determined with two different methods. One method ('Boltzmann method') calculates the ionic ground state density from the extrapolation of the ionic Dy lines in the Boltzmann plot to the ionization potential see equation 2.3. The other method ('Saha method') combines the value for η_∞ from the atomic Dy system with the electron density calculated using Hg (assuming $n_i = n_e$).

2.2.2 The absolute line intensity

In order to construct an ASDF we need to relate the intensity of Dy and Hg lines measured in the experiment to the absolute densities. If the plasma is optically thin, the radiation can escape the plasma as absorption can be neglected. The corresponding integrated emission coefficient of a particular transition j_{pq} [$\text{Wm}^{-3}\text{sr}^{-1}$], is defined as

$$j_{pq} = (1/4\pi)n_p A(p, q) E_{pq} \quad (2.10)$$

where n_p is the density of the upper level p, $A(p, q)$ the transition probability, $E_{pq} = E_{1p} - E_{1q} = h\nu_{pq}$, the energy of the emitted photon. This equation shows that the population density n_p of level p is proportional to the integrated emission coefficient j_{pq} ,

$$n_p = 4\pi \frac{j_{pq}}{A(p, q) E_{pq}} \quad (2.11)$$

The calibrated intensity I_{pq} [$\text{Wm}^{-2} \text{sr}^{-1}$] is determined by calibrating the line intensity of the metal-halide lamp with a tungsten ribbon lamp at the line of sight, over a plasma column of length D, and is given by

$$I_{pq} = \int_0^D j_{pq} ds. \quad (2.12)$$

j_{pq} is not necessarily constant over the length of the column, but could vary over the radial distance. Line intensities are measured at the line of sight. This means that the intensity of the spectral line is measured laterally, which is in our case along the horizontal cross-section of the burner. A lateral profile constitutes the integrated spectral line intensity as function of lateral position. Radial information can be extracted from a set of lateral measurements by the Abel inversion technique [7]. The radial intensity profile j_{pq} is approximated by means of a polynomial series [8],

$$j_{pq}(r) = a_0 + \sum_{n=2}^{\infty} a_n r^n. \quad (2.13)$$

The term $a_1 r$ is omitted because the derivative of the dysprosium density at the axis of the burner should be zero due to symmetry. Applying a least squares fitting procedure to the lateral profile the coefficients a_n are obtained and a radial profile is constructed.

After selecting a number of Dy and Hg lines from the measured spectrum of 400 to 800 nm, based on [9], the lateral profile of the corresponding emitting species can be

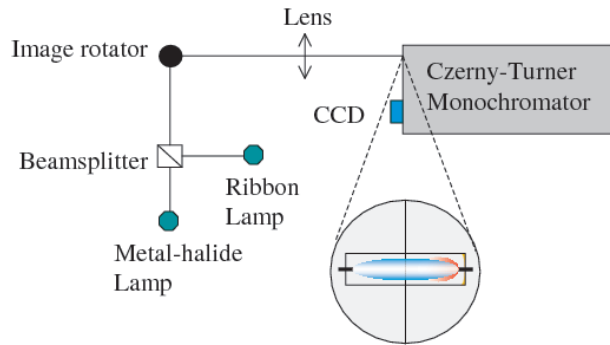


Figure 2.4: Setup consisting of a Czerny-Turner 1-meter monochromator, image rotator, beam splitter, and ST-2000 CCD camera. The CCD camera records the 2-D image of the light after being dispersed into different wavelengths by the grating of the monochromator. The wavelengths of the various atomic and ionic transitions are found on the horizontal scale. The image rotator optically rotates the image of the burner 90 degrees so it is projected horizontally onto the entrance slit, yielding a CCD image of the cross section of the burner on the vertical scale.

constructed. The radial profiles are then used to construct the ASDF for several radial positions. Measurements were done at different axial positions in the lamp, the results reported here were found at 3 mm above the bottom electrode with a $50 \mu\text{m}$ resolution in height.

2.3 Experimental setup

In the present experiment, emission spectroscopy is performed on a metal-halide lamp. The lamp consists of a quartz burner of 20 mm in length and 8 mm inner diameter and a transparent low-expansion quartz vacuum jacket. The burner is made of quartz in order to make the arc optically accessible. Because quartz does not withstand high temperatures, the chosen power is low, causing less of the additives to be present in the arc vapour than in commercially available lamps. The distance between the electrodes is approximately 18 mm. The lamp is dosed with 10.0 mg of Hg and 4.08 mg of DyI_3 . It is driven by a ballast with a 80 Hz square wave voltage, and operated with an average input power of 100 W.

The metal-halide lamp [6] is mounted on an optical rail in vertical position together with a beamsplitter, image rotator and a lens (focal length 200 mm), which focuses the lamp-image onto the entrance slit of the spectrometer, see figure 2.4. The Czerny-Turner 1-meter monochromator contains a 1200 lines per mm grating for wavelength separation and an ST-2000 CCD camera for 2-D imaging. This CCD chip is 1600 pixels wide and 1200 pixels high. The pixel size is $7.4 \mu\text{m}$ by $7.4 \mu\text{m}$. The image rotator rotates the lamp image 90° so that a horizontal cross-section of the lamp is imaged onto the vertical slit of the monochromator and then on the CCD camera. As the wavelength dispersion is in the horizontal direction we obtain, at one axial position, a complete lateral profile in one measurement. The two-

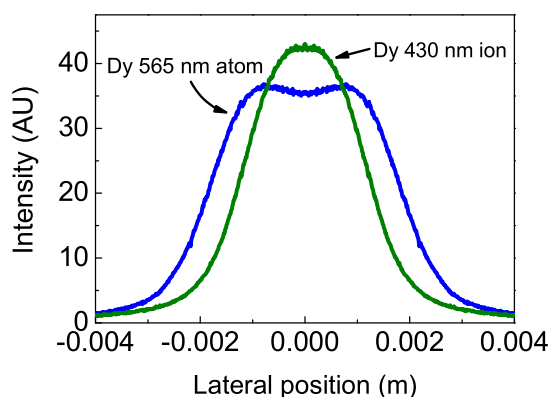


Figure 2.5: Lateral intensity profiles of atomic (at 565 nm) and ionic Dy (at 430 nm). The profiles are symmetrized with regard to the axis of the arc. The lines are measured 3 mm above the bottom electrode, the lamp power is 100 W.

dimensional CCD image therefore contains in the vertical direction the cross-section of the lamp and in horizontal direction the wavelengths of different atomic and ionic transitions. The intensity of the Dy and Hg lines are calibrated with a Tungsten ribbon lamp with known spectral intensity. The ribbon lamp is placed such that its calibrated light follows an optical path that is almost identical to that of the metal-halide lamp.

2.4 Results and discussion

Because the lateral profiles are not entirely symmetrical and cylinder symmetry is assumed, the lateral profiles are symmetrized with regard to the axis of the arc. The temperature at the axis is highest and the axis can therefore be found there where the intensity of Hg is highest. An example of the symmetrized lateral profiles in figure 2.5 shows the different lateral distributions of atomic and ionic species of Dy. Ions are at the centre, surrounded by atoms, which are in turn surrounded by (invisible) molecules near the wall. This is even more evident when looking at the radial intensity profiles in figure 2.6 derived from figure 2.5 using the previously described Abel inversion technique. There is a small dip in the centre of ionic Dy, this is most likely a temperature effect, as the temperature in the centre of the lamp is highest. It may also be caused by the Abel inversion technique, which is very sensitive for errors in the centre of the lateral profile.

From the radial profiles the ASDFs can be constructed for different radial positions. Figure 2.7 shows the ASDF at the axis of the lamp, 3 mm above the bottom electrode. Transition probabilities A from two different sources were used, Lawler [11] and Kurucz [9]. The measured lines and corresponding A values and relative errors are listed in the appendix.

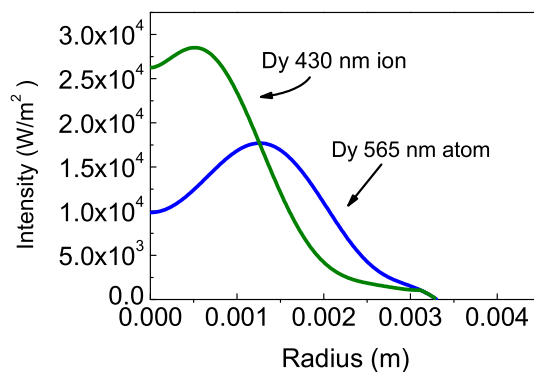


Figure 2.6: Calibrated radial intensity profiles of atomic (at 565 nm) and ionic Dy (at 430 nm). The lines are measured 3 mm above the bottom electrode, the lamp power is 100 W.

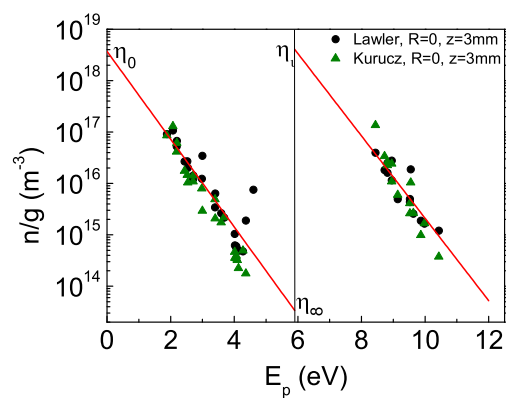


Figure 2.7: ASDF for Dy in the wavelength range of 400 to 700 nm. Emission lines are measured at the centre of the lamp 3 mm above the electrode. These results have been Abel inverted. The atomic and ionic transition probabilities are taken from Lawler [11] and Kurucz [9].

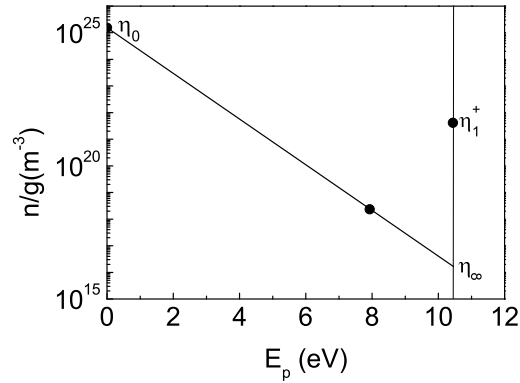


Figure 2.8: ASDF for Hg emission lines that are measured at the centre of the lamp 3 mm above the electrode. The ionization potential of Hg is at 10.44 eV. The ground state density is calculated from $p = nkT$. The intensity profile of the 407.8 nm line, with $A = 4 \cdot 10^6$ [11], at $E_p = 7.92$ eV has been Abel inverted.

The temperature for atomic Dy using the Lawler values is 5900 K and for ionic Dy it is 6300 K. The temperature for atomic Dy using the Kurucz values is 4700 K and for ionic Dy 4400 K. The Lawler values for A were found using an experimental technique that consists of a combination of fluorescent lifetime measurements of different levels and the determination of branching fractions by Fourier Transform Spectroscopy. The values of Kurucz were determined by estimation of the line intensity. Further results described in this paper make use of the Lawler values for A as we assume that the method used to determine them is more reliable. It is clear however that the errors in the A values are a strong limitation for the interpretation of our measurements. From the ASDF at different radial positions a radial temperature profile can be constructed for ionic and atomic Dy.

We now examine the Hg system. Only a small number of atomic Hg lines was observed, of which the energy levels were very close so that no accurate slope of the ASDF could be determined. This can be resolved by taking the absolute density of the ground state into account. First we calculate the ground state density of the Hg atom using the ideal gas law $p = nkT$. Due to the Hg dominance, n can be replaced by n_{Hg} density. As the pressure is constant over the lamp, nT is a constant over the whole plasma. We determine the pressure by calculating the total density of Hg inside the burner. This is done using the dimensions and Hg content of the lamp, which is 20 mm in height and 8 mm in diameter and contains 10 mg Hg, together with the assumption that the effective temperature equals 3000 K [10]. We then assume LTE and use the temperature profile for atomic Dy in combination with the calculated pressure to find the ground state density of Hg as function of the radius. It must be stated that the initial choice of temperature has limited effect on the results. In order to construct the ASDF we determine the absolute density at one line, at 407.8 nm, see figure 2.8. We can now calculate the temperature as a function of the radius.

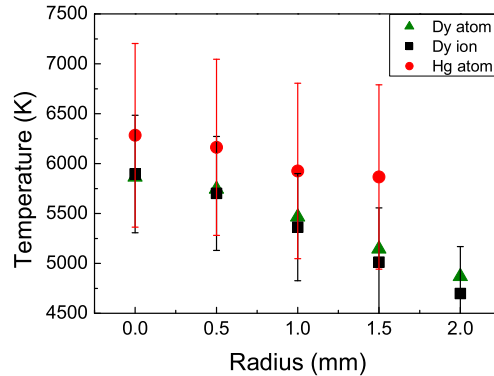


Figure 2.9: Temperature profiles for different radial positions, 3 mm above the bottom electrode. The lamp power is 100 W. The transition probabilities were taken from Lawler [11].

Figure 2.9 shows that the temperature profiles for atomic and ionic Dy and Hg are similar when taking the error of the linear fit of the scattered data points into account which, due to large scatter of the data points, is relatively high and about 10 to 14 percent.

Now that the temperature is known we calculate the ground states of atoms and ions as well as the electron density, and the total atomic and ionic density of Dy. From figure 2.7 and figure 2.8 it can be deduced that Hg is the dominant ion. Therefore the ratio between the Hg ion and the Dy ion has been calculated from these measurements. The ratio of Hg^+/Dy^+ ions is shown as function of the radius in figure 2.10, proving that Hg ions dominate over the Dy ions up to $R = 1.7$ mm. Because Hg ions are the leading system in the centre of the lamp, the bulk of the electrons are supplied by Hg. The electron density n_e was determined by calculating η_∞ by means of extrapolation of the atomic Hg ASDF and assuming $n_i = n_e$ for the inner region. The results are shown in figure 2.11.

Total atomic and ionic densities are also shown in figure 2.11. Dy atoms ionize into Dy ions in the hot centre of the lamp, causing a depletion of Dy atoms. The atomic density decreases toward the cooler wall making room for molecules. The atomic ground state density found by extrapolating the atomic ASDF is of the order $n_1 = 10^{20} \text{m}^{-3}$ (taking $g_1=17$). Flikweert *et al* [8] measured the atomic ground state density at different powers (at 113W and 151W), by means of laser absorption spectroscopy of a lamp of the same type. It was found that the value for the atomic ground state rapidly increases as function of power. An extrapolation to 100 W from these results leads to a similar value for the atomic ground state density.

The ratio between the ‘Saha method’ and the ‘Boltzmann method’ is depicted in figure 2.12. It shows that when moving away from the centre we see an increasing discrepancy between the two extrapolated ionic ground state densities. The ionic system is underpopulated with respect to the atomic system. This is what we expect as the ionic system suffers more loss of radiation than the atomic. This means that the Boltzmann balance of

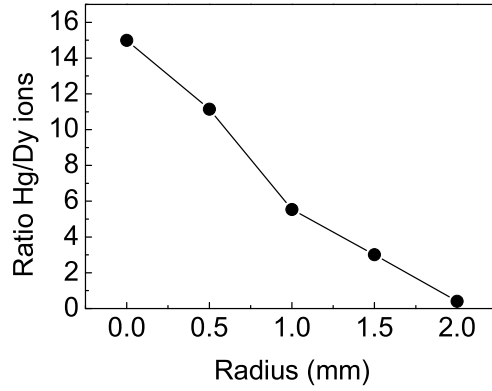


Figure 2.10: The ratio of Hg^+/Dy^+ ions for different radial positions. The total ionic density n^+ is calculated by combining the expression for η_∞ (equation 2.6) with the expression for n^+ (equation 2.9). η_∞ is found by means of extrapolation of the ASDF of Dy and Hg at different radial positions.

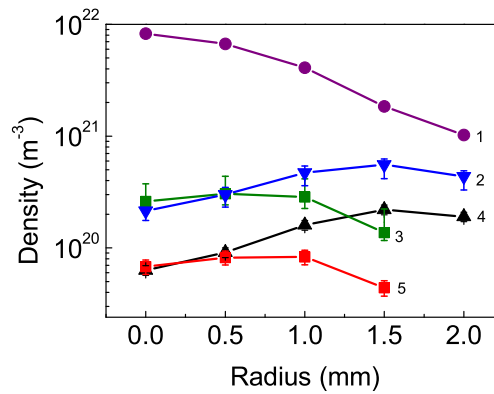


Figure 2.11: (1) electron density determined from the Hg ASDF. Total atomic (2) and ionic densities (3) for Dy. Atomic (4) and ionic (5) ground state densities for Dy.

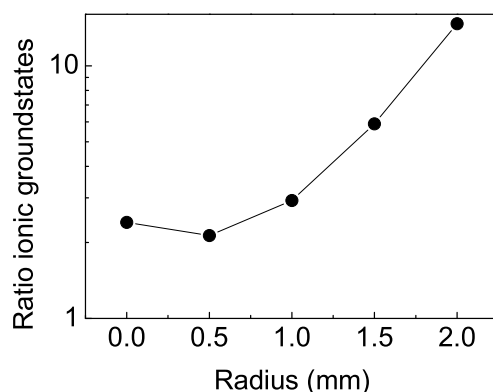


Figure 2.12: The ratio between the ionic ground state density calculated using the value for η_∞ , combined with the electron density calculated using the Hg density (assuming $n_i = n_e$); and the ionic ground state density calculated from the extrapolation of the ASDF for the Dy ion.

excitation and de-excitation is no longer in equilibrium and the assumption of LTE is no longer valid.

2.5 Conclusions

A radially resolved ASDF has been constructed for Dy and Hg for the metal-halide lamp. Radial intensity profiles of Dy show a clear separation between atomic and ionic regions in the plasma, the ionic region is in the hot centre, the atomic region surrounds it. The radial temperature profile constructed from the ASDF of atomic Dy shows a temperature of 5900 K in the centre of the lamp. The ionic and atomic temperature profile for Dy and the atomic Hg temperature profile are all equal within the error margins. Error margins are about 10 percent due to the large scatter in the data points, this can be remedied with better A values.

In this lamp driven at 100 W, Hg ions predominate in the centre of the discharge and contribute largely to the total electron density of the discharge. At the centre of the lamp there seems to be LTE, toward the wall there is a deviation of LTE with respect to the population of the Dy ionic system.

Future studies should include the measurement of the density distributions at different axial positions.

2.6 Acknowledgements

This research is supported by Technologiestichting STW (project ETF. 6093) and COST (project 529).

2.7 Measured lines and corresponding A values

Table I contains the A values for atomic Dy lines and Table II contains the A values for ionic Dy lines. A values are listed from Lawler [11] and Kurucz [9].

line (nm)	A value Lawler ($\times 10^6 \text{ s}^{-1}$)	A value Kurucz ($\times 10^6 \text{ s}^{-1}$)
402.371	29.0 $\pm 5\%$	58.55
411.305	23.4 $\pm 5\%$	92.10
412.608	0.92 $\pm 5\%$	73.1
413.035	1.76 $\pm 5\%$	1.84
414.606	195.0 $\pm 5\%$	347.8
419.802	108.0 $\pm 5\%$	214
423.202	79.0 $\pm 5\%$	146.8
423.985	94.0 $\pm 5\%$	145
424.591	118.0 $\pm 5\%$	178.9
429.196	2.28 $\pm 5\%$	6.159
448.436	4.65 $\pm 6\%$	10.48
456.509	0.66 $\pm 5\%$	0.864
457.778	1.96 $\pm 5\%$	2.448
488.016	0.520 $\pm 5\%$	0.7924
488.808	4.97 $\pm 5\%$	6.098
502.212	1.27 $\pm 5\%$	1.504
504.264	6.9 $\pm 5\%$	6.065
507.067	4.59 $\pm 5\%$	6.303
507.767	0.41 $\pm 8\%$	0.621
563.950	0.49 $\pm 8\%$	0.6007
565.201	0.446 $\pm 5\%$	0.4491
598.856	0.561 $\pm 5\%$	0.4636
616.843	0.81 $\pm 5\%$	1.702
657.937	0.77 $\pm 10\%$	0.8212

Table 2.1: A values used for the calculation of the density of atomic Dy. A values and relative errors from Lawler are given in [11]. Values from Kurucz [9] are based on data provided by either Gorshkov *et al* [13], where the relative error is estimated to be less than 50%; or by Meggers *et al* [14] from which the A values are determined from the estimated intensity.

line (nm)	<i>A</i> value Lawler ($\times 10^6 \text{ s}^{-1}$)	<i>A</i> value Kurucz ($\times 10^6 \text{ s}^{-1}$)
395.039	25 $\pm 6\%$	53.90
397.856	49.9 $\pm 5\%$	68.91
399.669	16.3 $\pm 6\%$	18.51
400.045	25.4 $\pm 5\%$	23.63
403.633	1.73 $\pm 8\%$	3.563
407.312	12.1 $\pm 7\%$	20.09
411.134	2.84 $\pm 5\%$	2.983
412.463	7.2 $\pm 5\%$	11.77
414.310	8.1 $\pm 8\%$	9.82
425.633	0.79 $\pm 5\%$	0.9048
430.863	2.78 $\pm 5\%$	1.71
444.970	1.97 $\pm 5\%$	1.062
446.814	0.451 $\pm 5\%$	0.4441
495.735	1.38 $\pm 5\%$	0.4011

Table 2.2: *A* values used for the calculation of the density of ionic Dy. *A* values and relative errors from Lawler are given in [11]. Values from Kurucz [9] are based on data provided by either Gorshkov *et al* [13], where the relative error is estimated to be less than 50%; or by Meggers *et al* [14] from which the *A* values are determined from the estimated intensity.

Bibliography

- [1] Lister G G, Lawler J E, Lapatovich W P and Godyak V A 2004 Rev. Mod. Phys. **76**, 541
- [2] Fischer E (1976) J. Appl. Phys. **47**, 2954
- [3] Zhu X 2005 Ph.D. thesis *Active spectroscopy on HID lamps*, Eindhoven University of Technology
- [4] Mitchner M and Kruger Jr CH 1973 *Partially ionized gases*, 1st ed., John Wiley and Sons
- [5] Van der Mullen J A M 1990 Phys. Rep. **191** 109
- [6] Stoffels W W, Kroesen G M W, Groothuis C H J M, Flikweert A J, Nimalasuriya T, Van Kemenade M, Kemps P, Bax M, Van den Hout F H J, Van den Akker D, Schiffelers G, Beckers J, Dekkers E, Moerel J, Brinkgreve P, Haverlag M, Keijser R and Kuipers A 2005 *Proceedings of the XXVIIth International Conference on Phenomena in Ionised Gases Eindhoven (16-342), july 17-22, E.M. Van Veldhuizen, Eindhoven University of Technology*
- [7] Curry J J, Sakai M and Lawler J E 1998 J. Appl. Phys. **84**, 3066
- [8] Flikweert A J, Nimalasuriya T, Groothuis C H J M, Kroesen G M W, and Stoffels W W, 2005, J. Appl. Phys. **98** 073301
- [9] Kurucz R L and Bell B 1993 *Atomic Line Data CD-ROM No 23* (Cambridge, MA: Smithsonian Astrophysical Observatory)
- [10] Elenbaas W 1951 *The high pressure mercury vapour discharge*, 1st ed., (North-Holland publishing company)
- [11] Wickliffe M W and Lawler J E 2000 J. Quant. Spectrosc. Radiat. Transfer **66**, 363
- [12] http://www.thespectroscopynet.com/Theory/Partition_Functions.asp
- [13] Gorshkov V N, Komarovskii V A, Oserovich A L, Penkin N P and Khefferlin R 1980 Opt. Spectrosk. **48**, 657-661
- [14] Meggers W F, Corliss C H and Scribner B F 1975 *Tables of Spectral-line intensities Part 1-Arranged by elements*, 2nd ed., (National Bureau of Standards)

Metal-halide lamps in the international space station ISS

Abstract. Optical emission spectroscopy was performed on a metal-halide lamp under the micro-gravity conditions of the international space station (ISS). Several transitions of atomic and ionic Dy, and atomic Hg have been measured at different lateral positions from which we obtained atomic and ionic Dy and atomic Hg intensity profiles. After Abel inversion, the calibrated radial intensity profile of Hg was used to calculate a radial temperature profile. By combining the radial temperature profile with the calibrated radial intensity profile of the additive, the absolute radial density profile of the total atomic and ionic density of Dy was obtained. The measurements showed a hollow density profile for the atoms and ions in the centre. In the outer parts of the lamp molecules were found to dominate. Lamps containing Dy showed contraction of the arc, which increased for higher powers. Measurements were duplicated at 1-*g* and showed less radial segregation than for 0-*g*. As the power was increased, the difference between 0-*g* and 1-*g* of the radial intensity, density and temperature profile were diminished.

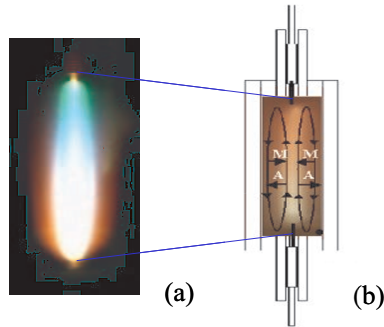


Figure 3.1: (a) Colour separation in a metal-halide lamp burner. (b) Schematic view of a metal-halide lamp; diffusion and convection of atoms (A) and molecules (M) are indicated by arrows. See figure 1.1 for full colour.

3.1 Introduction

The need for compact high-intensity light sources with high luminous efficacy and good colour rendering properties has led to the development of the metal-halide lamp [1]. This type of arc lamp contains a buffer gas of Hg and a relatively small amount of a mixture of additives such as DyI_3 , CeI_3 or NaI salts, which supply the prime radiators. More than two salt components are necessary for a good colour rendering index, therefore mixtures such as $(\text{NaI} + \text{ScI}_3)$, $(\text{NaI} + \text{TlI} + \text{InI})$ or $(\text{NaI} + \text{TlI} + \text{DyI}_3 + \text{HoI}_3 + \text{TmI}_3)$ are commonly used in metal-halide lamps.

Due to the competition between diffusive and convective processes these additives are non-uniformly distributed over the lamp, resulting in the undesirable segregation of colours [2], see figure 3.1. This means that lamp performance is strongly dependent on burning orientation (vertical and horizontal). Since the convective processes are induced by gravity, placing the arc lamp in a gravity-free environment would aid the understanding of the transport processes resulting in this so-called de-mixing. Previous efforts to observe the arc and its characteristics in micro-gravity include the relatively straightforward emission measurements aboard the space shuttle [3] [4], and the optical emission spectroscopy measurements during the parabolic flights [5] [6]. During the parabolic flights, however, micro-gravity was obtained for a period of only 20 to 25 seconds. This is not enough time for the arc to adjust to the micro-gravity conditions. The international space station (ISS), on the other hand, provides a gravity-free environment where stable arc conditions are ensured.

In this paper we present and discuss experiments performed on HID lamps in the ISS in 24th and 25th April in 2004 by André Kuipers. There the lamps were subjected to extended micro-gravity conditions in order to separate and help clarify the role of convection and other transport mechanisms in the arc of the lamp. For the purpose of this study the lamp was filled with an Hg buffer gas and one salt, namely DyI_3 . This lamp has a relatively simple salt system and therefore the results are easier to compare with the results of a numerical

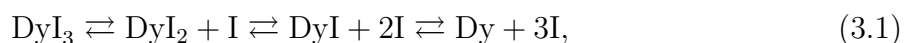
model. For comparison, lamps containing pure Hg were also studied. The lamp was investigated by means of optical emission spectroscopy, which yields line intensities of the species Hg and Dy [7]. From calibrated Hg line intensity we constructed radial temperature profiles. By combining the temperature profile with the calibrated line intensities for Dy we obtained absolute radial density distributions for these species. All measurements were done for different powers ranging from 70 to 150 W.

This chapter is organized as follows. Section 3.2 describes the segregation phenomenon and the method used to determine the temperature of the arc and atomic and ionic densities. Section 3.3 describes the arc lamps used in the experiments and the experimental setup. Results from the experiments are presented and discussed in section 3.4. These results constitute radial profiles of the arc temperature and absolute atomic and ionic densities of Dy for different lamp powers. Finally, section 3.5 offers conclusions and recommendations for future work.

3.2 Theory

3.2.1 Segregation

The main light emitting species, Dy atoms and ions, are brought into the plasma by evaporation of the liquid DyI_3 , molecules of which then dissociate into atoms and ions. Whereas the Hg evaporates completely, the few milligrams of the DyI_3 additive do not entirely evaporate, leaving a liquid salt pool at the coldest spot of the burner wall. The cold spot determines the vapour pressure of the additive in the immediate vicinity of the salt pool. Because of the large temperature gradient between the wall (~ 1200 K) and the centre of the burner (~ 6000 K) [8], a multi-step process of dissociation of DyI_3 molecules towards the centre and association of atoms into molecules near the wall takes place. The reaction balances chain can be described as follows,



the temperature increasing to the right. At the hot centre Dy atoms ionize and Dy ions are created,



Three mechanisms influence the distribution of particles in the plasma. First, there is a high temperature in the centre, which rapidly decreases towards the wall. Because of $p = nkT$ this high temperature results in a hollow profile of the density distribution over the lamp. Second, there is the difference between the diffusion velocities of atoms and molecules. The smaller and lighter Dy atoms diffuse faster outward than the larger and heavier molecules (DyI , DyI_2 , DyI_3) diffuse inward. This difference in diffusion velocity results, in steady-state, in an even more hollow profile of the elemental density of Dy; this is called radial segregation [2]. Elemental density is defined as the density that contains all molecular, atomic and ionic contributions of a particular element.

The third mechanism, convection, causes the hot gas to move upwards in the hot centre of the arc and downwards along the cool wall of the lamp. This movement of the bulk gas drags the high concentration of Dy near the wall downwards. Whereas, the lower concentration of Dy in the centre, caused by the radial segregation, is dragged upwards. As a consequence, high density of elemental Dy accumulates at the bottom of the arc, a phenomenon which is known as axial segregation [2]. The combination of axial and radial segregation is shown in figure 3.1(b).

One way to study radial segregation of Dy exclusively is to prevent the formation of axial segregation. By placing the metal-halide lamp in a gravity-free environment, no convection can take place and therefore no axial segregation occurs. This gravity-free environment is realised in the international space station ISS.

In most HID lamps, the discharge contracts toward the axis of the arc tube, creating a dark annular space between the discharge and the tube wall [9]. The gas temperature profile in such a contracted discharge can be described by an expression proposed by Fischer for high pressure discharges [10]

$$T(r) = T_{wall} + T_1 \left(1 - \left(\frac{r}{R}\right)^2\right) + T_2 \left(1 - \left(\frac{r}{R}\right)^2\right)^\gamma, \quad (3.3)$$

with r the radius and R the total radius of the arc tube, γ is a measure for the amount of contraction of the discharge. T_1 and T_2 are fitting parameters that determine the maximum temperature in the centre of the discharge ($r=0$), together with the value of γ . The wall temperature T_{wall} is estimated to be about 1200 K at the midplane of the lamp [8] that was investigated in this study.

3.2.2 Emission of radiation

One way to study the effect of radial segregation is to determine the radial density profiles of the additives. If the discharge is in LTE (Local Thermal Equilibrium), the density of the additives can be determined by measuring the intensity of light emitted by atoms and ions.

For an optically thin line, the radiant power U_{pq} [Wm^{-3}] emitted by a spectral line is

$$U_{pq} = A(p, q)h\nu_{pq}n_p, \quad (3.4)$$

where $A(p, q)$ is the transition probability of the transition, $h\nu_{pq}$ the energy of the emitted photon, and n_p the number density of an emitting atom or ion in upper energy level p . Under LTE conditions, the Boltzmann relation [11] can be used to link the number density n_p to the total number (system) density n_s of the atom or ion

$$n_p = n_s \frac{g_p}{Q(T)} \exp\left(\frac{-E_p}{kT}\right), \quad (3.5)$$

where g_p is the statistical weight of upper level p , T is the temperature and k the Boltzmann constant. $Q(T)$ is the partition function of the considered atomic or ionic system

$$Q(T) = \sum_i g_i \exp\left(\frac{-E_i}{kT}\right). \quad (3.6)$$

We can now determine the total number density of particles of a particular atomic system from the radiant power

$$n_s = \frac{U_{pq}Q(T)}{g_p A(p, q) h \nu_{pq}} \exp\left(\frac{E_p}{kT}\right), \quad (3.7)$$

where U_{pq} is determined experimentally, while $Q(T)$, g_p , $A(p, q)$ can be found in literature [12–14]. What is needed for the calculation of the density using equation (3.7) is the radially resolved radiant power $U_{pq}(r)$, which is acquired by the line intensity measurement of the optically thin line of the species in question, and the arc temperature $T(r)$ as a function of radial position.

The radiant power $U_{pq}(r)$ of an optically thin line is deduced from the lateral (i.e. line-of-sight) measurement of the arc. The wavelength integrated intensity of the chosen spectral line is determined as a function of lateral position. This yields the lateral intensity profile. A lateral profile constitutes the integrated spectral line intensity as a function of lateral position. Radial information can be extracted from a set of lateral measurements by the Abel inversion technique [15]. The technique used approximates the radial intensity profile j_{pq} by means of a polynomial series [16],

$$j_{pq}(r) = a_0 + \sum_{n=2}^{\infty} a_n r^n. \quad (3.8)$$

The term a_{1r} is omitted because, due to symmetry, the derivative of the dysprosium density at the axis of the burner should be zero. By applying a least-squares-fitting procedure to the lateral profile, the coefficients a_n are obtained and a radial profile is constructed [7]. In this way the lateral intensity profile is converted into the radial intensity profile which, after calibration, yields $U_{pq}(r)$.

The radial temperature profile is calculated from the dominant species, in this case atomic Hg. The temperature is calculated using equation (3.7), for which $U_{pq}(r)$ and the total Hg density n_{Hg} are needed. $U_{pq}(r)$ is determined from the optically thin 579 nm Hg line, which is calibrated. The total Hg density n_{Hg} can be reformulated in terms of temperature using the ideal gas law $p = nkT$, assuming $p = p_{\text{Hg}}$ and is constant over the discharge, where p_{Hg} can be written as

$$p_{\text{Hg}} = n_{\text{Hg}} kT_{\text{eff}} = \frac{N_{\text{Hg}} kT_{\text{eff}}}{V} = \frac{m_{\text{effHg}} N_A kT_{\text{eff}}}{m_{\text{Hg}} \pi R^2 h}. \quad (3.9)$$

N_A is Avogadro's number, m_{Hg} the molar mass of Hg; and R and h the total radius and height of the burner respectively. N_{Hg} is the total amount of Hg in the discharge region,

and T_{eff} is the effective temperature. m_{effHg} is the total Hg dose in the discharge region, this is defined as the burner volume minus the electrode volume (the volume behind the tip of the electrodes). We need to take into account the amount of Hg which is located behind the electrodes. This is estimated to be $38 \pm 10\%$, the effective Hg dose is therefore estimated to be 62% of the total Hg dose [17]. The effective temperature T_{eff} can be calculated using

$$T_{eff} = \frac{p_{Hg}V}{N_{Hg}k} \quad (3.10)$$

which can be rewritten using

$$N_{Hg} = \int n_{Hg}dV = \frac{p_{Hg}}{k} \int \frac{1}{T(r)}dV. \quad (3.11)$$

Assuming cylinder-symmetry and combining equations (3.10) and (3.11), the effective temperature can now be written as

$$T_{eff} = \frac{V}{\int \frac{1}{T(r)}dV} = \frac{R^2}{2 \int_0^R \frac{r}{T(r)}dr}. \quad (3.12)$$

Combined with equation (3.7), $T(r)$ can be calculated numerically from the measured $U_{pq}(r)$ of the 579 Hg line using an iterative method. The 579 nm Hg line cannot, however, be accurately determined at radial positions beyond $r > 2$ mm. Therefore, the temperature profile is extrapolated using the expression for the radial temperature profile introduced by Fischer [10]. This expression is used to extrapolate the temperature from the inner part of the burner to the wall. The error in the temperature profile is estimated to be less than 10% over the whole range.

3.3 Experimental Setup

The spectrometer, used for the optical emission measurements of HID lamps, was exclusively designed for measurements in the ISS [18]. Accordingly, the spectrometer had to be compact, light weight, and robust. Ordinary spectrometers make use of the accurate movement of a dispersion grating for wavelength selection and are therefore not suitable for an experiment in space. They also tend to be relatively large, as large focal lengths are needed for the lenses in order to achieve a reasonable spectral resolution. The requirement for compactness is solved by using an Echelle grating with a high blaze angle (74°). Due to the high angle of incidence and the use of high orders, the dispersion is high and therefore the focal length of the lenses can be relatively small, allowing the spectrometer to be very compact. A disadvantage of Echelle-type spectrometers is that they have a relatively small free spectral range (FSR) at high orders, which results in wavelength overlapping of adjacent orders at a fixed position on the detector. By placing an interference filter in the optical system for the selection of a small wavelength interval, the problem of overlapping orders is avoided. As different filters can be selected for different wavelength intervals,

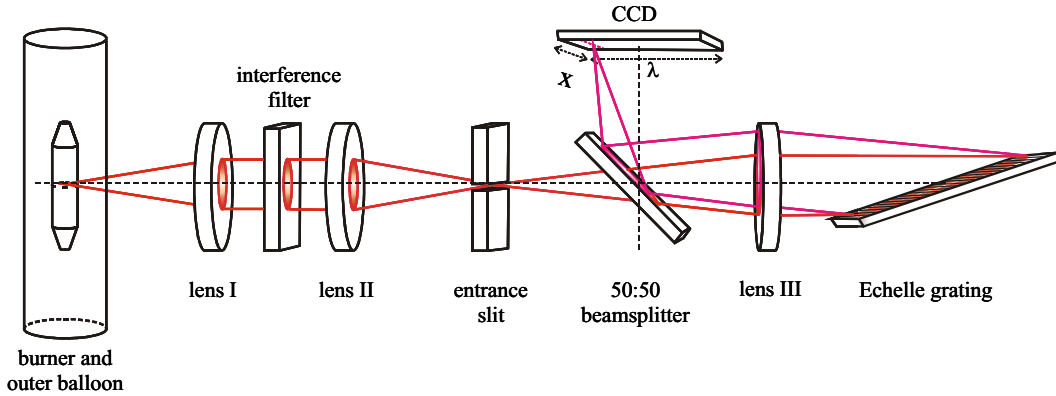


Figure 3.2: Setup used for the ISS measurements. It is an Echelle type spectrometer in Littrow configuration, the imaging lens (III) is used for the collimation of both the un-dispersed beam of light as well as the reflected dispersed beam of light.

the angle of the grating remains fixed. In this way, the requirement for robustness is also fulfilled, because no critically moving parts exist inside the spectrometer [18].

In the ISS experiment, emission spectroscopy was performed on a metal-halide lamp [16]. The lamp consists of a quartz burner of 20 mm in length and 8 mm in inner diameter and a transparent quartz vacuum outer bulb. The burner is made of quartz in order to make the arc optically accessible. The distance between the electrodes is approximately 18 mm. Table 3.1 shows the used lamps with the different dosages. It is driven by a Philips Dynavision ballast with a 83 Hz square wave current profile, and operated at different input powers ranging from 70 to 150 W in steps of 20 W.

Hg dose (mg)	additive	additive dose (mg)
10.00	DyI ₃	4.044
5.00	DyI ₃	4.011
10.00	-	0
10.00	DyI ₃	4.128
5.00	DyI ₃	3.953
10.00	-	0

Table 3.1: Lamps with dosages of Hg and the additive DyI₃. All lamp burners are shaped as cylinders.

A schematic of the Echelle-type spectrometer is shown in figure 3.2 [17] [18]. The light originating from the plasma forms a parallel beam after going through lens I (100 mm focal distance). A parallel beam is necessary for the proper functioning of the wavelength selection by the interference filter, which is situated between lens I and lens II (also 100 mm focal distance). Lens I and II combined with the interference filter form a 1:1 image of the burner on the horizontally placed entrance slit (10 mm x 10 μ m) of the desired

wavelength interval. The light emanating from the slit is the emission along the cross-section at the centre of the burner. It passes a 50:50 beam splitter and after being collimated by an achromatic doublet (Lens III), the light reaches the Echelle grating (96 mm x 46 mm) having 79.01 lines/mm and a 74.1° blaze angle. Lens III is positioned at its focal distance (150 mm) from the entrance slit to create a parallel beam of light on the Echelle grating. Then the light is back-reflected and dispersed with conservation of the spatial information. The angle of the reflected light with the optical axis of the system depends on the wavelength of the light. The reflected light is collimated by the same doublet (Lens III) and focused via the 50:50 beam splitter on the CCD-surface of the camera (SBIG ST-2000XM, 1600x1200 pixels of $7.4\mu\text{m} \times 7.4\mu\text{m}$). As the wavelength dispersion is in the horizontal direction, we obtain a complete lateral profile in one measurement. The two-dimensional CCD image therefore contains the lateral cross-section in the vertical direction of the lamp, measured at a position halfway between the two electrodes. In the horizontal direction the CCD image contains the wavelengths of different atomic and ionic transitions. As stated before, wavelength selection is done by selecting the interference filter that corresponds to the desired wavelength interval [18].

Only the intensity of the 579 nm Hg line was calibrated with the ISS setup, using a source with known spectral radiance. Lamp L05, which contains only Hg, was measured on earth with the Echelle spectrometer with the interference filter corresponding to the 579 nm line, and calibrated with a Tungsten ribbon lamp. The lines that were used are listed in table 3.2. After the experiments were completed, calibration of the 402 and the 642 nm Dy lines were done with a setup nearly identical to the ISS setup [19] at 1g using, again, a Tungsten ribbon lamp. This allowed for the calibration of the Dy lines which were then used to calculate the absolute density of atomic and ionic Dy.

species	line (nm)	A value	source A value
Dy I	642.19	$1.6 \times 10^5 \text{ s}^{-1}$	Kurucz
Dy II	402.44	$8.4 \times 10^6 \text{ s}^{-1}$	Wickliffe and Lawler
Hg I	579.07	$2.1 \times 10^7 \text{ s}^{-1}$	Derived from Benck and Lawler

Table 3.2: Lines measured with the Echelle spectrometer. *A* values used for the calculation of the density of atoms and ions of Dy, and Hg, are taken from Kurucz [12] and Wickliffe, Benck and Lawler [13]. The *A* value for the 579.07 nm Hg line is derived from the $g_p A$ value for the 576.96 nm line [20]. The intensity of the 579.07 nm line is 10% lower than that of the 576.96 nm line and both lines have nearly the same upper level. The $g_p A$ value of the 579.07 nm line is therefore taken as 10% less than that of the 576.96 nm line. With $g_p=5$ this gives an *A* value of $2.1 \times 10^7 \text{ s}^{-1}$ for the 579.07 nm line.

Calculation of the radial density profiles of the additive Dy is as follows. First the emission of the line of interest is measured as a function of lateral position. The total intensity of the line is then calculated, which yields the lateral intensity profile. This profile is then Abel inverted into a radial intensity profile. The next step depends on the species of which the emission line is measured.

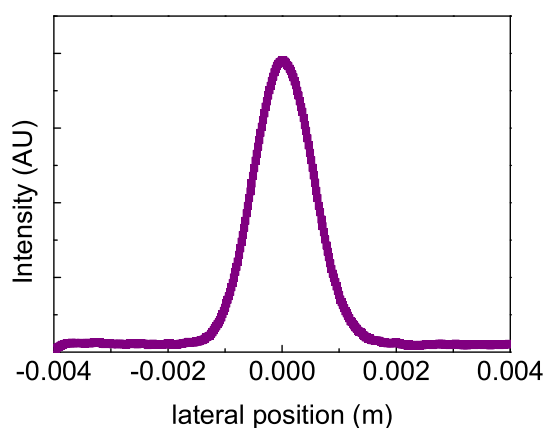


Figure 3.3: Lateral intensity profile of Hg at zero- g for a lamp containing 4 mg of DyI_3 and 10 mg of Hg operated at 150W.

In case of the 579 nm line of Hg, the intensity is calibrated and then the absolute radial intensity profile is used to numerically determine the temperature profile. If atomic or ionic lines of Dy are measured, the temperature profile is combined with the calibrated radial intensity profile of the additive into an absolute radial density profile as in equation (3.7).

3.4 Results and Discussion

In figure 3.3 the lateral intensity profile of atomic Hg is shown. The centre of the profile was determined by a parabolic fit, the maximum of which indicated the centre of the arc. Once the position of the centre was established, the Abel inversion technique was applied to transform the lateral intensity profile into a radial intensity profile of Hg. A typical result is given in figure 3.4.

After calibration, the radial intensity profile of Hg was used to calculate the temperature profile numerically, as described in the section 3.2.

Temperature profiles of a lamp containing 10 mg of Hg without Dy, are plotted for different lamp powers in figure 3.5. The temperature profile resembles a parabolic profile with a core temperature of about 5800 K for a lamp operated at 150W. The figure clearly shows that for increasing powers the temperature profile becomes broader.

Figure 3.6 shows the different lateral distributions of atomic and ionic species of Dy. The figure shows that ions are at the centre, surrounded by atoms. The atoms, in turn are surrounded by (non-detectable) molecules near the wall.

The lateral intensity profile for Dy does not go to zero near the edge of the arc, this is most probably caused by stray-light. In order for the Abel-fit to yield physical results, the fit was forced to zero near the edges of the lateral profile. Instead of covering the whole

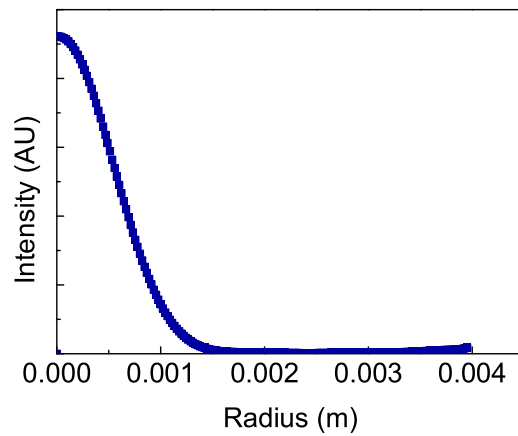


Figure 3.4: Radial intensity profile of Hg at zero- g for a lamp containing 4 mg of DyI_3 and 10 mg of Hg operated at 150W.

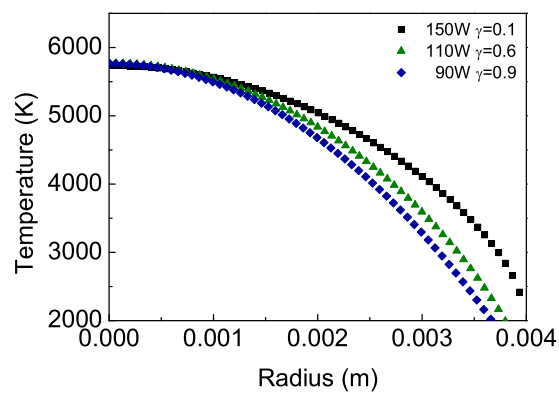


Figure 3.5: Radial temperature profiles at zero- g for a lamp containing 10 mg of Hg operated at different lamp powers. γ indicates the amount of contraction; $\gamma=1$ means there is no contraction. [10]

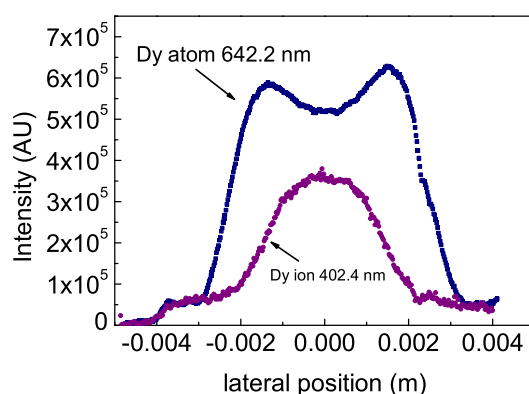


Figure 3.6: Lateral intensity profile of Dy at zero- g for a lamp containing 4 mg of DyI_3 and 10 mg of Hg operated at 150W.

range of the lateral profile (which is 8 mm wide), a slightly smaller fitting range (of about 6 mm wide) was chosen. This was done because atomic and ionic intensities are expected to go to zero near the wall, see figure 3.7. This caused a discrepancy in the fit near 3 mm, which was exacerbated by the exponent in the density calculation. The resulting density profile is therefore considered unreliable for $r > 3$ mm. Some of the density and intensity plots of Dy in this paper are therefore marked with a shaded area indicating the limit to which the plot can still be considered reliable.

From the lateral intensity profile, the radial intensity profile of atomic and ionic Dy (as shown in figure 3.8), was then constructed using the Abel inversion technique. To determine the total density of Dy atoms and ions, a radial temperature profile is required to be constructed for the lamp in question.

A typical example of a radial temperature profile of a lamp containing 10 mg of Hg and 4 mg of DyI_3 for different lamp powers is shown in figure 3.9. The axis temperature was about 6300 K for 150 W. It is clear that the arc contracted, especially at high powers such as 150W. The contraction can be quantitatively represented by the contraction parameter γ from equation 3.3. If $\gamma > 1$, the arc column is contracted. It was observed that $\gamma=0.1$ for a lamp operating at 150W with a pure Hg content, whereas for a lamp containing both Hg and Dy it was found that $\gamma=3.4$. Dy atoms are the main species responsible for radiation. Therefore, emission from the peripheral atomic Dy lines caused radiation loss at the flanks of the discharge, causing the arc to contract. The lamp was kept at constant power as the arc contracted, while the same amount of power went through a smaller volume. Therefore, if the radiation loss is small enough, the contraction caused the temperature to increase. When the power is increased the arc becomes more contracted, as more atomic Dy enters the arc, leading to an increase of radiation loss in the flank.

Combining the calibrated radial intensity profile with the radial temperature profile shown in figure 3.9, and using equation 3.7 we can calculate the radial density profile of

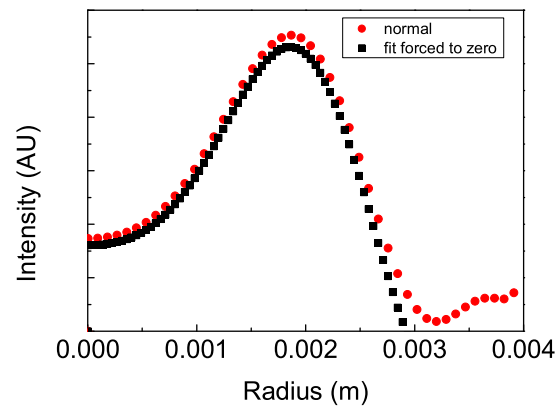


Figure 3.7: Two different Abel-fits at zero- g for a lamp containing 4 mg of DyI_3 and 10 mg of Hg operated at 150W. One fit is forced to zero near the edges of the lateral profile.

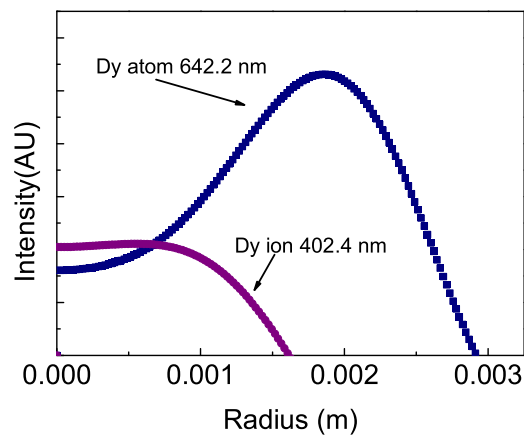


Figure 3.8: Relative radial intensity profile at zero- g for a lamp containing 4 mg of DyI_3 and 10 mg of Hg operated at 150W.

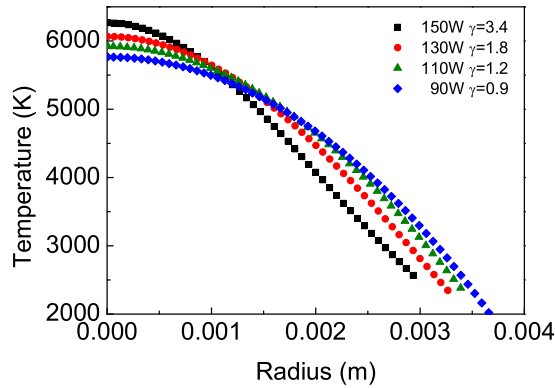


Figure 3.9: Radial temperature profiles at zero- g for a lamp containing 4 mg of DyI_3 and 10 mg of Hg operated at different lamp powers. γ indicates the amount of contraction, $\gamma=1$ means there is no contraction. [10]

the total atom or ion density. The radial density profiles of the total atom and ion Dy density are shown in figures 3.10 and 3.11 respectively. Dy atoms ionize into Dy ions in the hot centre of the lamp, causing a depletion of Dy atoms. The atomic density decreases toward the cooler wall making room for molecules. The contraction seen in the temperature profile can also be seen in these figures.

In order to determine which species dominated in the centre of the lamp, the ratio of Hg^1 and Dy ions has been calculated for a lamp operated at 150 W. The ratio of Hg^+/Dy^+ ions is shown in figure 3.12 as a function of the radius; it demonstrates that Hg ions are more abundant than the Dy ions up to $r = 1.5$ mm. In newer types of HID lamps, the burner is often made of PCA (poly-crystalline alumina). PCA can withstand much higher temperatures, allowing the temperature of the discharge, wall and salt pool to be higher than for a discharge contained by a quartz burner. Therefore, more Dy is expected to be in the discharge in a PCA burner than is the case for burners made of quartz.

All measurements that were planned for micro-gravity conditions were duplicated during normal gravity conditions before the setup was sent to the ISS. Radial temperature profiles for a lamp containing 10 mg of Hg and 4 mg of DyI_3 are shown in figure 3.13 (a,b,c) for powers ranging from 110-150W. The figure shows that the arc contracts more strongly for 0- g ($\gamma = 1.8$ for 110W) than for 1- g ($\gamma = 1.2$ for 110W).

Radial atomic intensity profiles are plotted for 1- g and 0- g for different powers in figure 3.14(a,b,c). These profiles clearly indicate a shift in the distribution of Dy atoms at 0- g . For 0- g there is less atomic Dy in the centre of the discharge and more near the wall. This phenomenon can be explained by the absence of convection at 0- g . As there is no convection, there is no axial segregation. Assuming the cold spot temperature is roughly

¹The Hg ion density was calculated from the Hg atom density using Saha [11], where $n_e = n_{\text{Hg}^+}$

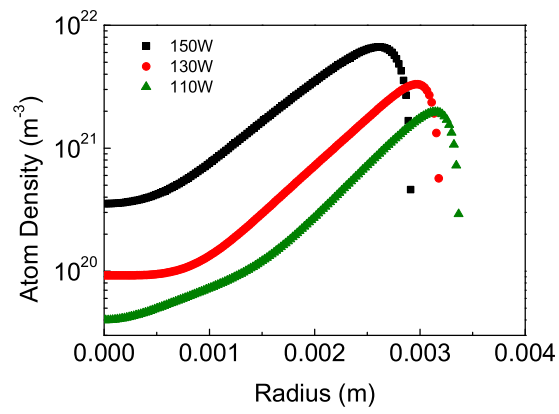


Figure 3.10: Radial density profile of atomic Dy at zero-*g* for a lamp containing 4 mg of DyI₃ and 10 mg of Hg.

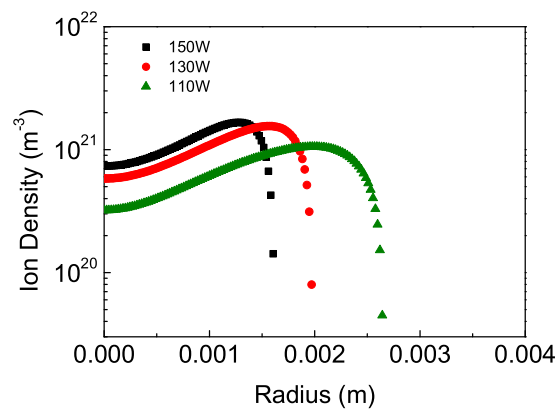


Figure 3.11: Radial density profile of ionic Dy at zero-*g* for a lamp containing 4 mg of DyI₃ and 10 mg of Hg.

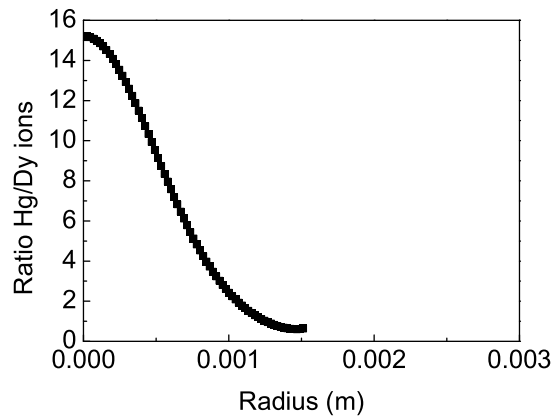


Figure 3.12: Ion ratio of Hg and Dy at zero- g for a lamp containing 4 mg of DyI_3 and 10 mg of Hg operated at 150 W.

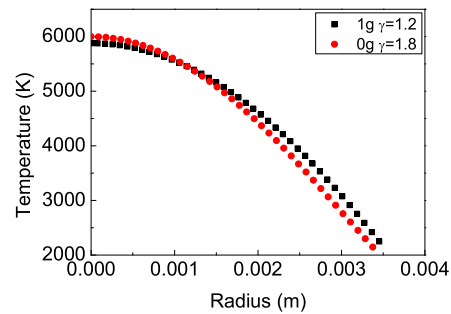
the same for 1- g as it is for 0- g , the absence of axial segregation at 0- g causes the Dy density to be distributed uniformly over the length of the lamp [5]. This results in an increase of Dy near the wall at the axial mid-point of the lamp. The stronger dip in the centre was caused by the increase of radial segregation as there is no mixing due to convection at 0- g . These effects cause the flank of the discharge to contain more Dy for 0- g than for 1- g , resulting in higher radiation loss at 0- g , leading to a stronger contraction at 0- g . The shift between 0- g and 1- g becomes less pronounced as the power increases. Both the temperature profiles and the intensity profiles show that at 150 W the discrepancy between 1- g and 0- g is diminished.

Scaled concentration profiles of the atomic density were calculated in order to eliminate temperature effects and the effects of axial segregation. The concentration was calculated by dividing the atom density by the total Hg density (acquired with $p = nkT$, assuming $T_{\text{eff}}=3000$ K). Then the 0- g concentration profile was scaled with the concentration profile of 1- g at 3 mm. The results are depicted in figure 3.15(a,b,c) for powers ranging from 110 to 150 W. As expected, more radial segregation occurs for 0- g than for 1- g , as there is no mixing due to convection in 0- g .

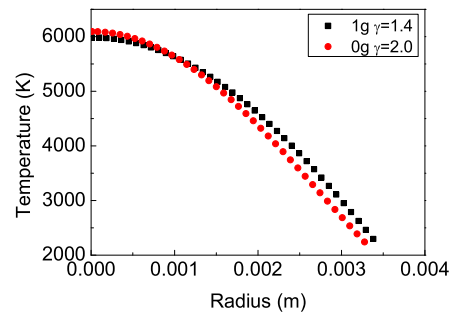
3.5 Conclusions

Absolute total atomic and ionic radial density profiles were constructed for lamps containing 10 mg of Hg and 4 mg of Dy under the micro-gravity conditions of the ISS. Radial density profiles of Dy show a clear separation between atomic and ionic regions in the plasma; the ionic region is in the hot centre, the atomic region surrounds it. Hg ions predominate in the centre of the discharge and contribute largely to the total electron density of the discharge.

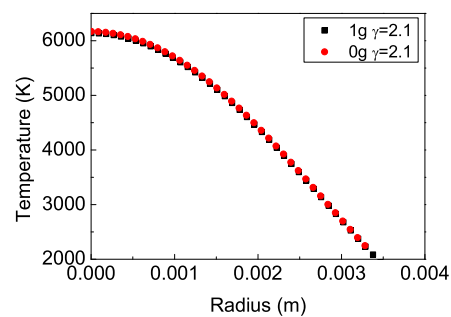
The radial temperature profiles were constructed from the lateral profile of atomic Hg



(a)

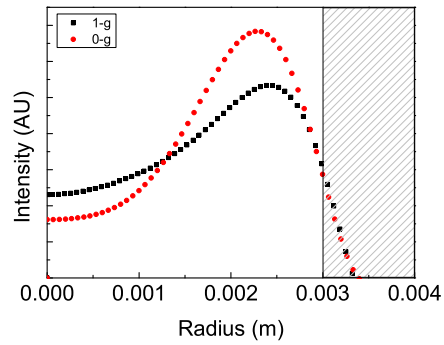


(b)

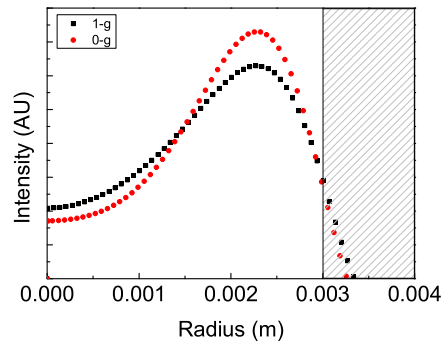


(c)

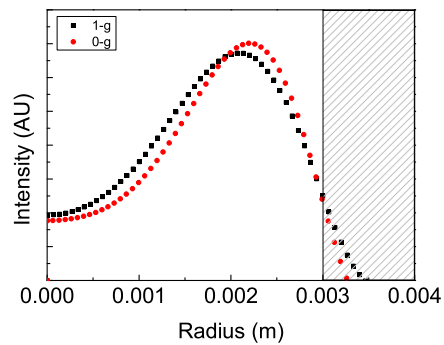
Figure 3.13: Radial temperature profiles for a lamp containing 4 mg of DyI_3 and 10 mg of Hg during normal and micro-gravity conditions at 110 W (a) 130 W (b) and 150 W (c). γ indicates the amount of contraction, $\gamma=1$ means there is no contraction. [10]



(a)

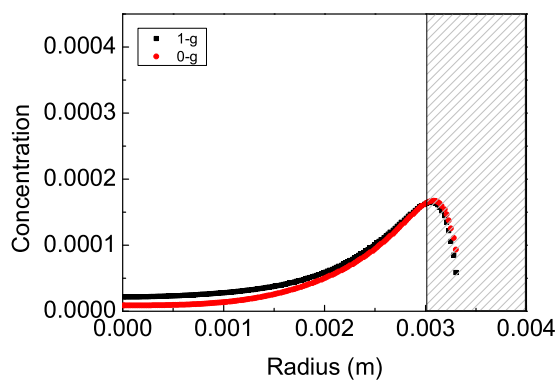


(b)

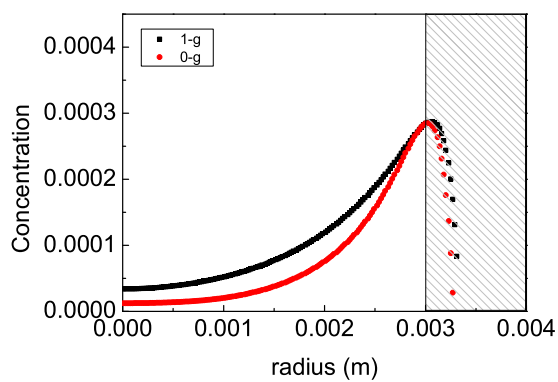


(c)

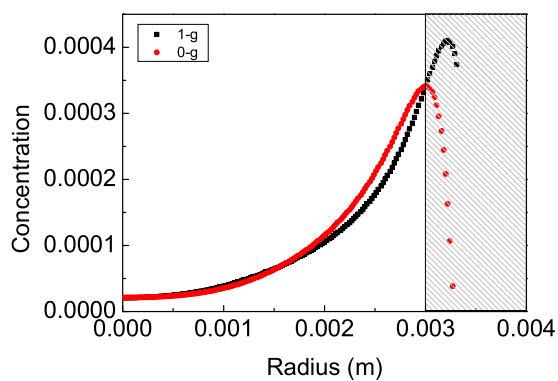
Figure 3.14: Intensity profile of atomic Dy for a lamp containing 4 mg of DyI_3 and 10 mg of Hg measured at normal and micro-gravity conditions for a lamp operated at 110 W (a) 130 W (b) and 150 W (c). The plots are considered to be reliable for $r < 3\text{mm}$, which is up to the shaded area.



(a)



(b)



(c)

Figure 3.15: Concentration profile of atomic Dy for a lamp containing 4 mg of DyI_3 and 10 mg of Hg measured at normal and micro-gravity conditions for a lamp operated at 110 W (a) 130 W (b) and 150 W (c). The plots are considered to be reliable for $r < 3\text{mm}$, which is up to the shaded area.

for different lamp powers. A lamp containing a pure Hg dose, operated at 150W, showed a temperature of 5800 K and a parabolic profile in the centre of the arc. The temperature profile of a lamp containing both Hg and Dy had a temperature of 6300 K at the axis of the lamp, in addition it showed a contracted profile, especially for higher powers.

Comparison between 0-*g* and 1-*g* showed, as expected, that there was more radial segregation at 0-*g*. The temperature profile of a lamp containing both Hg and Dy showed an axis temperature of 6100 K at 1-*g*, which is comparable to the axis temperature at 0-*g* within the error margin. The difference between 1-*g* and 0-*g* of the radial temperature, intensity and density profiles, decreased for high powers.

Absence of convection will facilitate the numerical study of the transport phenomena of the metal-halide lamp. Future study should include the comparison of the experimental results with the numerical model.

3.6 Acknowledgements

The authors wish to thank the ARGES team [22] [18], P.L.E.M. Pasmans and K.C. Kuiper for their contributions. The authors acknowledge the support from Philips Lighting, European Space Agency ESA, National Aerospace and Space Administration NASA, Russian Space Agency RSC Energia, SENTER, NOVEM, Space Research Organisation Netherlands SRON, the Netherlands Ministries for Education and Research and for Economic affairs, the executive board of the Eindhoven University of Technology, and Technologiestichting STW (project ETF. 6093), COST (project 529).

Bibliography

- [1] Lister G G, Lawler J E, Lapatovich W P and Godyak V A 2004 Rev. Mod. Phys. **76**, 541
- [2] Fischer E 1976 J. Appl. Phys. **47**, 2954
- [3] Bellows A H, Feuersanger A E, Rogoff G L, and Rothwell H L 1984 *HID convection studies: a space shuttle experiment* Illuminating Engineering Soc. Meeting
- [4] Bellows A H, Feuersanger A E, Rogoff G L, and Rothwell H L 1984 *Convection and Additive segregation in High pressure lamp arcs: Early results from a space shuttle experiment* Gaseous electronics Conf., 1985 Bull. Amer. Phys. Soc. Vol **30**, p 141
- [5] Flikweert A J, Van Kemenade M, Nimalasuriya T, Haverlag M, Kroesen G M W and Stoffels W W 2006 J.Phys.D **39**, 1599
- [6] Stoffels W W, Haverlag M, Kemps P C M, Beckers J and Kroesen G M W 2005 Appl. Phys. Lett. **87** 1
- [7] Nimalasuriya T, Pupat N B M, Flikweert A J, Stoffels W W, Haverlag M and Van der Mullen J J A M 2006 J. Appl. Phys. **99** 053302 **see chapter 2**
- [8] Zhu X 2005 Ph.D. thesis *Active spectroscopy on HID lamps*, Eindhoven University of Technology
- [9] Elenbaas W 1951 *The high pressure mercury vapour discharge*, 1st ed., (North-Holland publishing company)
- [10] Fischer E 1978 *Influences of External and Self-Magnetic Fields on the behaviour of discharge lamps*, Philips GmbH Forschungslaboratorium Aachen Lobornotiz nr 13/78.
- [11] Mitchner M and Kruger Jr C H 1973 *Partially ionized gases*, 1st ed., (John Wiley and Sons).
- [12] Kurucz R L and Bell B 1993 *Atomic Line Data CD-ROM No 23* (Cambridge, MA: Smithsonian Astrophysical Observatory)
- [13] Wickliffe M W and Lawler J E 2000 J. Quant. Spectrosc. Radiat. Transfer **66**, 363
- [14] http://www.thespectroscopynet.com/Theory/Partition_Functions.asp
- [15] Curry J J, Sakai M and Lawler J E 1998 J. Appl. Phys. **84**, 3066
- [16] Flikweert A J, Nimalasuriya T, Groothuis C H J M, Kroesen G M W and Stoffels W W 2005, J. Appl. Phys. **98** 073301
- [17] Kemps P C M, 2004 Master's thesis *An experimental study of the radial additive density and plasma temperature profiles, and the effect of this on the integral light output of metal halide lamps as a function of gravity* Eindhoven University of Technology

- [18] Kroesen G M W, Haverlag M, Dekkers E, Moerel J, de Kluijver R, Brinkgreve P, Groothuis C H J M, Van der Mullen J J A M, Stoffels W W, Keijser R, Bax M, Van den Akker D, Schiffeleers G, Kemps P C M, Van den Hout F H J, Kuipers A 2005 Microgravity sci. technol. XVI-1
- [19] Nimalasuriya T, Thube G M, Flikweert A J, Haverlag M, Kroesen G M W and Stoffels W W 2007 J.Phys.D 40, 2839 **see chapter 3**
- [20] Benck E C, Lawler J E and Dakin J T 1989 J. Opt. Soc. Am. B **6**, 11
- [21] Van der Mullen J J A M 1990 Phys. Rep. **191** 109
- [22] Stoffels W W, Kroesen G M W, Groothuis C H J Mv, Flikweert A J, Nimalasuriya T, Van Kemenade M, Kemps P C M, Bax M, Van den Hout F H J, Van den Akker D, Schiffelers G, Beckers J, Dekkers E, Moerel J, Brinkgreve P, Haverlag M, Keijser R and Kuipers A 2005 Proceedings of the XXVIIth International Conference on Phenomena in Ionised Gases Eindhoven (16-342), july 17-22, 2005, E.M. Van Veldhuizen, Eindhoven University of Technology.

Axial segregation in metal-halide lamps under gravity conditions ranging from 1 to 10 g

Abstract. Axial segregation in metal-halide lamps is caused by a complex interaction between convection and diffusion and is not yet fully understood. By enhancing convection, by placing the lamp in a centrifuge, the effect of convection on axial segregation was studied. The centrifuge caused the lamp to be accelerated between 1 and 10 g . Optical emission spectroscopy was performed on a metal-halide lamp while placed in the centrifuge. Several transitions of atomic and ionic Dy, and atomic Hg have been measured at different lateral positions from which we obtained atomic and ionic Dy and atomic Hg intensity profiles. Atomic lateral profiles of Dy at different axial positions in the lamp were used for the calculation of Fischer's axial segregation parameter. The theoretical model of the Fischer curve, which shows the axial segregation parameter as a function of convection, was verified along the full range by measuring lamps of different filling and geometry. Moreover, the radial temperature profile of the arc for the different accelerations was determined.

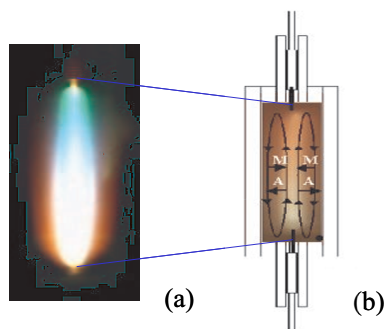


Figure 4.1: (a) Colour separation in a metal-halide lamp burner. (b) Schematic view of a metal-halide lamp; diffusion and convection of atoms (A) and molecules (M) are indicated by arrows. See figure 1.1 for full colour.

4.1 Introduction

The wish for compact high-intensity light sources with high luminous efficacy and good colour rendering properties has led to the development of the metal-halide lamp [1]. This type of arc lamp contains a buffer gas of Hg and a relatively small amount of a mixture of metal-halide additives such as DyI_3 , CeI_3 or NaI salts, which supply the prime radiators. At least two salt components are necessary for a good colour rendering index, therefore mixtures such as (NaI + ScI_3), (NaI + TlI + InI) or (NaI + TlI + DyI_3 + HoI_3 + TmI_3) are commonly used in metal-halide lamps.

Due to the competition between diffusive and convective processes these additives are non-uniformly distributed over the lamp, resulting in the undesirable segregation of colours [2], see figure 4.1. Since the convective processes are induced by gravity, excluding or increasing the effects of gravity on the arc allows for a better understanding of the segregation phenomenon in the metal-halide lamp. During experiments at the international space station (ISS) the lamp operated under micro-gravity conditions [3], thereby eliminating the convective processes in the arc.

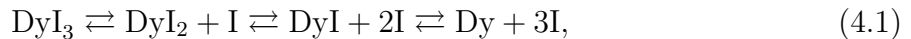
Both micro and hyper-gravity conditions were obtained during parabolic flights [4] [5] where micro-gravity and hyper-gravity up to $2g$ was obtained for 20 to 25 seconds. More time, however, is needed for the arc to stabilize. Also, it would be of interest to subject the lamp to g 's higher than 2. Therefore, a centrifuge was built that allows for an acceleration ranging from 1 to $10g$. In the centrifuge the lamps were subjected to extended hyper-gravity conditions in order to separate and help clarify the role of convection and other transport mechanisms in the arc of the lamp. For the purpose of this study the lamp was filled with an Hg buffer gas and one salt, namely DyI_3 . In this way a relatively simple salt system was achieved allowing for the experimental results to be easily compared with the results of numerical modelling. The lamp was investigated by means of optical emission spectroscopy, which yields line intensities of the species Hg and Dy [6]. From calibrated Hg line intensities we constructed radial temperature profiles.

This chapter is organized as follows. Section 4.2 describes the segregation phenomenon and the method used to determine the temperature of the arc. Section 4.3 describes the arc lamps used in the experiments and the experimental setup. Results from the experiments are presented and discussed in section 4.4. These results constitute lateral intensity profiles at different axial positions, the axial segregation parameter as a function of g and radial profiles of the arc temperature. Finally, section 4.5 offers conclusions and recommendations for future work.

4.2 Theory

4.2.1 Segregation

The main light emitting species, Dy atoms and ions, are brought into the plasma by evaporation of the liquid DyI_3 , these Dy molecules dissociate into atoms and ions. Whereas the Hg evaporates completely, only a fraction of the few milligrams of the DyI_3 additive evaporates. The rest of the DyI_3 remains as a liquid salt pool at the coldest spot of the burner wall. The cold spot determines the vapour pressure of the additive in the immediate vicinity of the salt pool. Because of the large temperature gradient between the wall (~ 1200 K) and the centre of the burner (~ 6000 K) [7], a multi-step dissociation process of DyI_3 molecules towards the centre and association of atoms into molecules near the wall takes place. The chain of reaction balances can be described as follows,



where the temperature increases to the right. At the hot centre Dy atoms ionize and Dy ions are created,



Three mechanisms influence the distribution of particles in the plasma. First, there is a high temperature in the centre, which rapidly decreases towards the wall. Because of $p = nkT$ this high temperature results in a hollow profile of the density distribution over the lamp. Second, there is the difference between the diffusion velocities of atoms and molecules. The smaller and lighter Dy atoms diffuse faster outward than the larger and heavier molecules (DyI , DyI_2 , DyI_3) diffuse inward. This difference in diffusion velocity results, in steady-state, in an even more hollow profile of the elemental density of Dy. This phenomenon is called radial segregation [2]. Elemental density is defined as the density that contains all molecular, atomic and ionic contributions of a particular element. For example, for Dy the elemental density (denoted with $\{\}$) can be described as

$$\{n_{\text{Dy}}\} = [\text{Dy}] + [\text{Dy}^+] + [\text{DyI}] + [\text{DyI}_2] + [\text{DyI}_3]. \quad (4.3)$$

The third mechanism, convection, causes the hot gas to move upwards in the hot centre of the arc and downwards along the cool wall of the lamp. This movement of the bulk gas drags the high concentration of Dy near the wall downwards. Moreover, the lower

concentration of Dy in the centre, caused by the radial segregation, is dragged upwards. As a consequence, high density of elemental Dy accumulates at the bottom of the arc, a phenomenon which is known as axial segregation [2]. The combination of axial and radial segregation is shown in figure 4.1(b).

4.2.2 Axial segregation

Fischer theoretically described the diffusion-convection mechanism for axial segregation in vertically operated lamps [2]. In his model of axial segregation of additives of metal-halide lamps he assumed that the arc temperature profile is parabolic and independent of axial position. The convection profile (which is governed completely by the buffer gas in all metal-halide lamps) can be calculated using the Navier-Stokes equation:

$$\frac{\partial p}{\partial z} + \rho_m \tilde{g} - \frac{1}{r} \frac{\partial}{\partial r} \left(r \eta \frac{\partial v_z}{\partial r} \right) = 0 \quad (4.4)$$

with the boundary conditions

$$\left. \frac{\partial v_z}{\partial r} \right|_{r=0} = 0 \quad v_z = 0 \Big|_{r=R} \quad (4.5)$$

where r is the radial position, R the radius of the arc tube, ρ_m the buffer gas mass density, η the viscosity of the buffer gas, v_z the axial velocity (the radial velocity is assumed to be zero) and \tilde{g} the acceleration. Normally, \tilde{g} stands for gravitational acceleration, in this case this stands for the acceleration caused by the centrifuge. In this paper the amount of acceleration is given in terms of $g = 9.8m/s^2$. The axial velocity can be described as [16]

$$v_z \sim \frac{p_{Hg} R^2 \tilde{g}}{\eta} \quad (4.6)$$

This equation shows that the axial velocity, which equals the convection speed, is proportional to the acceleration \tilde{g} . The axial segregation can therefore be directly influenced by \tilde{g} .

Fischer described axial segregation by showing that the density declines along the axis exponentially [2]

$$n_i(z) = n_{i,0} \exp(-\lambda z), \quad (4.7)$$

where λ is the axial segregation parameter for species i , z the height and $n_{i,0}$ the density at the bottom of the arc. There are two extreme cases. At high values for the buffer gas pressure p_0 , burner radius R and g the axial segregation parameter can be approximated by

$$\lambda \approx p_0^2 R^2 g \quad (4.8)$$

and for low values of the buffer-gas pressure, burner radius and g by

$$\lambda \approx (p_0^2 R^2 g)^{-1} \quad (4.9)$$

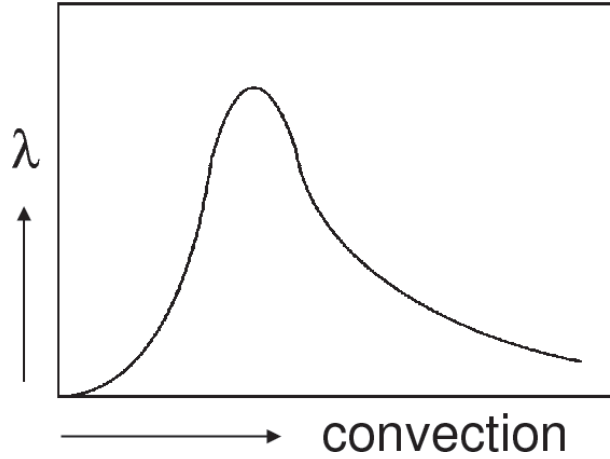


Figure 4.2: The Fischer curve [2] which represents the dependence of the axial segregation parameter λ on convection, or g .

The region in-between has a maximum, see figure 4.2. This curve that shows the axial segregation parameter λ as a function of convection is called the Fischer curve. On the left-hand side λ increases as a function of g and therefore as a function of convection. On the right-hand side λ decreases as a function of convection. By placing the lamp in a centrifuge and by using lamps with a different buffer gas pressure the full curve can be covered experimentally.

4.2.3 Emission of radiation

One way to study the effect of radial and axial segregation is to determine the radial density profiles of the additives. If the discharge is in LTE (Local Thermodynamic Equilibrium) [8], the density of the additives can be determined by measuring the intensity of light emitted by atoms and ions.

For an optically thin line, the radiant power $U_{pq}(\mathbf{r})$ [Wm^{-3}] emitted by a spectral line is

$$U_{pq}(r) = A(p, q)h\nu_{pq}n_p, \quad (4.10)$$

where $A(p, q)$ is the transition probability of the transition between the upper energy level p and the lower level q , $h\nu_{pq}$ the energy of the emitted photon, and n_p the number density of an emitting atom or ion in upper energy level p .

The radiant power $U_{pq}(\mathbf{r})$ of an optically thin line is deduced from the lateral (i.e. line-of-sight) measurement of the arc. First the spectral intensity $I_\lambda(\lambda, x)$ is measured as a function of lateral position x and calibrated with a ribbon lamp with known spectral intensity. Then these absolute spectral intensities are subsequently integrated over the transition giving $I_{pq}(x)$. The integrated spectral line intensity $I_{pq}(x)$ as a function of lateral position x is called the lateral profile. Finally, radial information can be extracted from the lateral profile by the Abel inversion technique [9]. Abel inversion of $I_{pq}(x)$ gives the transition

integrated emission coefficient $j_{pq} = A(p, q)h\nu_{pq}n_p/(4\pi)$ from which $U_{pq}(r) = A(p, q)h\nu_{pq}n_p$ can be determined.

Once $U_{pq}(r)$ is known the radial temperature profile can be calculated from the dominant species, in this case atomic Hg [3, 10]. Rewriting equation 4.10 using $n_p = n_{total} g_p \exp(-E_p/kT)/Q(T)$ [11], the temperature can be calculated from the following equation

$$n_{Hg} = \frac{U_{pq}(r)Q(T)}{g_p A(p, q)h\nu_{pq}} \exp\left(\frac{E_p}{kT}\right), \quad (4.11)$$

where n_{Hg} is the total number (system) density of particles of atomic Hg, $U_{pq}(r)$ is determined experimentally, while the partition function $Q(T)$, g_p , $A(p, q)$ can be found in literature [12] [13] [14]. $U_{pq}(r)$ is determined from the calibrated optically thin 579 nm Hg line. The total Hg density n_{Hg} can be reformulated in terms of temperature using the ideal gas law $p = nkT$, assuming that $p = p_{Hg}$ and that the pressure is constant over the discharge, where p_{Hg} can be written as

$$p_{Hg} = n_{Hg} kT_{eff} = \frac{N_{Hg}kT_{eff}}{V} = \frac{m_{effHg}N_AkT_{eff}}{m_{Hg}\pi R^2h}. \quad (4.12)$$

N_A is Avogadro's number, m_{Hg} the molar mass of Hg; and R and h the total radius and length of the burner respectively. N_{Hg} is the total amount of Hg in the discharge region, T_{eff} the effective temperature and m_{effHg} the total Hg dose in the discharge region. Assuming cylinder symmetry, the effective temperature T_{eff} can be written as [3]

$$T_{eff} = \frac{R^2}{2 \int_0^R \frac{r}{T(r)} dr}. \quad (4.13)$$

Combined with equation (4.11), $T(r)$ can be calculated numerically from the measured $U_p(r)$ of the 579 Hg line using an iterative method [3].

The 579 nm Hg line cannot, however, be accurately determined at radial positions beyond $r > 2$ mm. Therefore, the temperature profile is extrapolated using the expression for the radial temperature profile introduced by Fischer [15]

$$T(r) = T_{wall} + T_1 \left(1 - \left(\frac{r}{R}\right)^2\right) + T_2 \left(1 - \left(\frac{r}{R}\right)^2\right)^\gamma, \quad (4.14)$$

with r the radial position and R the total radius of the arc tube, γ is a measure for the amount of contraction of the discharge. Equation 4.14 is used to extrapolate the temperature from the inner part of the burner to the wall. In most HID lamps, the discharge contracts toward the axis of the arc tube, creating a dark annular space between the discharge and the tube wall [16]. The gas temperature profile in such a contracted discharge can be described by an expression proposed by Fischer for high pressure discharges [3, 15] T_1 and T_2 are fitting parameters that determine the maximum temperature in the centre of the discharge ($r=0$), together with the value of γ . The wall temperature T_{wall} is measured to be about 1200 K at the midplane of the lamp [7] that was investigated in this study. The error in the temperature profile is estimated to be less than 10% over the whole range.

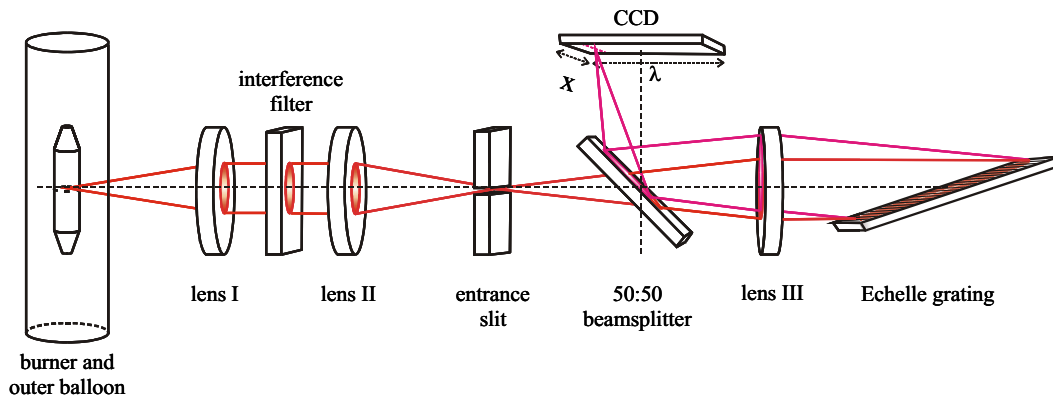


Figure 4.3: Setup [3,10] used for both the ISS and centrifuge measurements. It is an Echelle type spectrometer in Littrow configuration, the imaging lens (III) is used for the collimation of both the un-dispersed beam of light as well as the reflected dispersed beam of light.

4.3 Experimental Setup

The spectrometer is attached to the arm of a centrifuge, see figure 4.4. The arm is 1.0 m long and the centrifuge is about 2 m high. The maximum speed is 13.8 m/s, when this is reached the resultant acceleration, that is parallel to the lamp axis, equals 10 g . A schematic representation of the acceleration of the lamp is shown in figure 4.5.

The design for the spectrometer used for the optical emission measurements of HID lamps, was at first used for measurements in the ISS [3]. As the spectrometer had to be compact, light weight, and robust, it was an ideal design for the spectrometer on the centrifuge.

A schematic of the Echelle-type spectrometer is shown in figure 4.3 [3,10]. The light originating from the plasma forms a parallel beam after going through lens I (100 mm focal distance). A parallel beam is necessary for the proper functioning of the wavelength selection by the interference filter, which is situated between lens I and lens II (also 100 mm focal distance). Lens I and II combined with the interference filter form a 1:1 image of the burner on the horizontally placed entrance slit (10 mm x 10 μm) of the desired wavelength interval. The light emanating from the slit is the emission along the lateral cross-section at one axial position of the burner. It passes a 50:50 beam splitter and after being collimated by an achromatic doublet (Lens III), the light reaches the Echelle grating (96 mm x 46 mm) having 79.01 lines/mm and a 74.1° blaze angle. Lens III is positioned at its focal distance (150 mm) from the entrance slit to create a parallel beam of light on the Echelle grating. Then the light is back-reflected and dispersed with conservation of the spatial information. The angle of the reflected light with the optical axis of the system depends on the wavelength of the light. The reflected light is collimated by the same doublet (Lens III) and focused via the 50:50 beam splitter on the CCD-surface of the camera (SBIG ST-2000XM, 1600x1200 pixels of 7.4 μm x 7.4 μm). As the wavelength dispersion is imaged in the horizontal direction and the lateral position in the vertical, we obtain a complete

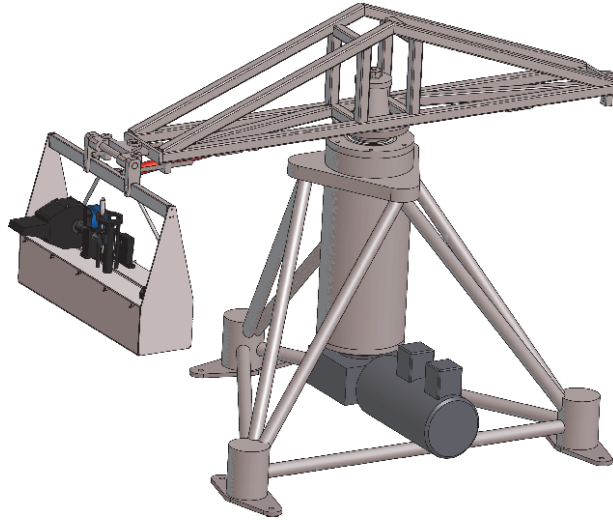


Figure 4.4: The centrifuge with the spectrometer attached to the arm.

lateral profile in one measurement. The two-dimensional CCD image therefore contains, in the vertical direction, the lateral cross-section of the lamp, measured at one axial position. Moving the lamp vertically allows for measurements at different axial positions. In the horizontal direction the CCD image contains the wavelengths of different atomic and ionic transitions. A broad wavelength selection is done by selecting the interference filter that corresponds to the desired wavelength interval [3].

All lines were calibrated, using a ribbon lamp that was placed at exactly the same position as the metal-halide lamp in the centrifuge setup.

species	line (nm)	A value	source A value
Dy I	642.19	$1.6 \times 10^5 \text{ s}^{-1}$	Kurucz [12]
Dy II	402.44	$8.4 \times 10^6 \text{ s}^{-1}$	Wickliffe and Lawler [13]
Hg I	579.07	$2.1 \times 10^7 \text{ s}^{-1}$	Derived from Benck and Lawler [17]

Table 4.1: Lines measured with the Echelle spectrometer. The A value for the 579.07 nm Hg line is derived from the $g_p A$ value for the 576.96 nm line [3,17].

In the centrifuge experiment, emission spectroscopy was performed on a metal-halide lamp [18,19]. The lamp consists of a quartz burner of 20 mm in length and 8 mm in inner diameter and a transparent quartz vacuum outer bulb. Measurements were also performed on a lamp of 22 mm length and 4 mm diameter. The burner is made of quartz in order to make the arc optically accessible. It is driven by a Luxmate Dimtronics 150 ballast with a 120 Hz square wave voltage.

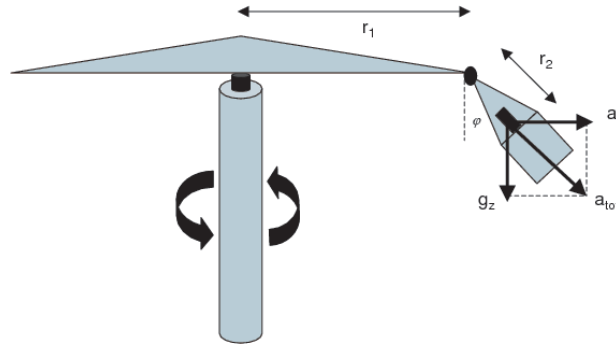


Figure 4.5: Schematic representation of the acceleration applied to the lamp when the centrifuge is spinning. a_r is the centrifugal acceleration, g_z the gravitational acceleration and a_{tot} is the resultant acceleration which is expressed in terms of g .

4.4 Results and discussion

The vertically burned lamps were subjected to an acceleration from 1 to 10 g , during which the emission spectroscopy measurements were done. The lamp was also monitored with a webcam, figure 4.6 shows webcam images for a lamp containing 5 mg Hg and 4 mg DyI₃. These images clearly show how the blueish-white light, caused by Dy atoms, is being more evenly distributed over the lamp as g becomes higher. As is typical for a lamp on the right side of the Fischer curve, this is caused by the mixing which is increased as the convection is increased, leading to a decrease in axial segregation. It needs to be mentioned that although the webcam causes the actual colours to distort, this does not hinder qualitative analysis.

This is also apparent when we look at the lateral profiles constructed at different axial positions in the lamp of atomic Dy, see figure 4.7, and of ionic Dy, see figure 4.8. Figures 4.7 and 4.8 show the lateral profiles near the bottom, the centre and near the top of the lamp containing 10 mg Hg and 4 mg DyI₃. As expected the ion density is highest on the axis of the central region of the arc, while a dip in the radial distribution of the Dy atoms is found. From the lateral profile near the bottom, we see that at higher g -values the amount of Dy atoms and ions decline, whereas at the top the amount of Dy atoms and ions increase as g increases.

The decrease of Dy near the bottom at higher g could be caused by the decrease of the cold spot temperature as g is increased. This can happen in two ways. First, as g is increased, convection increases, causing the arc to contract. Contraction of the arc means that the surrounding wall becomes cooler, this causes the cold spot temperature to decrease, thereby releasing less Dy into the arc. This contraction can also be seen in figures 4.7(a) and 4.8 (a) at higher g . Second, the power is being distributed more evenly over the arc as Dy is being more mixed, therefore the reduced power density at the bottom causes the cold spot temperature to decline. It needs to be mentioned that when comparing the lateral profiles at the top and the bottom of the lamp, there is always more Dy at the

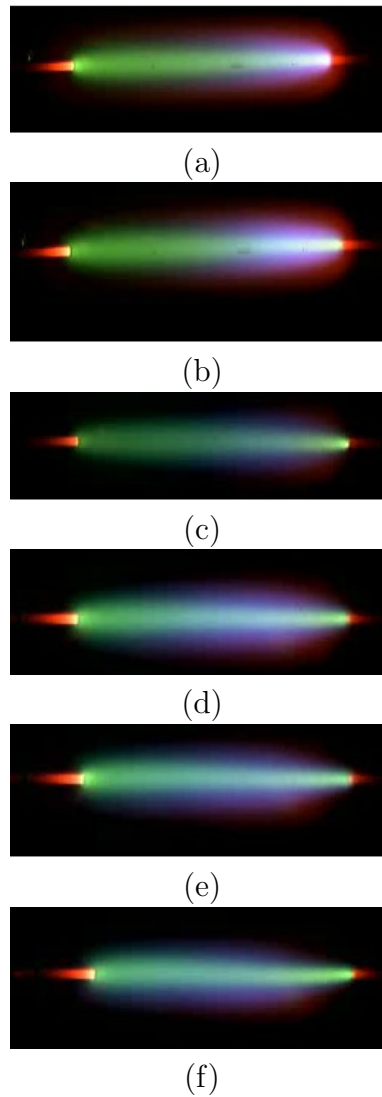
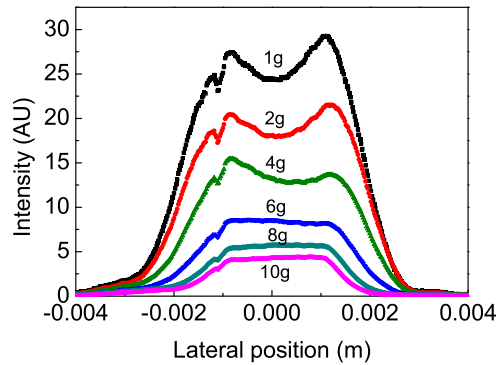
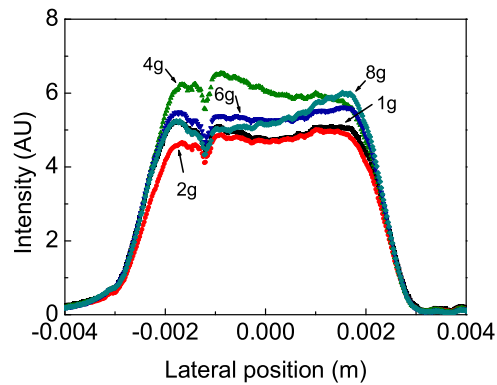


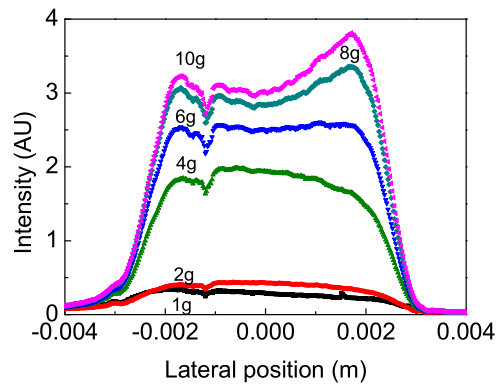
Figure 4.6: Webcam images for a lamp containing 5 mg Hg and 4 mg DyI₃. Figure (a) is the lamp at 1*g*, (b) at 2*g*, (c) at 4*g*, (d) at 6*g*, (e) at 8*g* and (f) at 10*g*. The lamp was burned vertically, this means the acceleration coincides with the central axis, the bottom of the lamp is on the right-hand side of the images.



(a)



(b)



(c)

Figure 4.7: Atomic lateral profiles for the atomic Dy line at 642.19 nm. The lamp filling was 10 mg Hg and 4 mg DyI₃, the measurements were done at three different axial positions z , (a) near the bottom at $z/Z=27,5\%$ (b) at the centre at $z/Z=50\%$ (c) near the top at $z/Z=72.5\%$ where $Z=20\text{mm}$. Although the intensity was not calibrated, the measurements done at the same wavelength are absolute with respect to each other.

bottom than at the top, so the axial segregation remains.

Near the top of the lamp it is clear that for higher g -values more Dy atoms reach the top of the lamp. Figure 4.7(c) shows that there is no change in contraction and figure 4.8(c) shows in fact that there is a broadening of the arc.

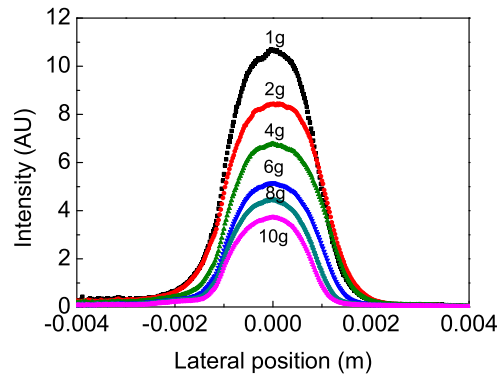
The axial segregation parameter λ can be calculated in different ways, either using the radial density or the lateral intensity as a function of axial position. Both of these were examined as a function of g , yielding the Fischer curve, this is shown in figure 4.9. The curves are identical within the error margin and shows the same shape as figure 4.2. Apparently it does not matter whether the radially resolved density or the lateral emission intensity is used for the calculation of λ . Using the lateral intensity instead of the density is preferable as no Abel inversion is needed, thereby reducing the error in the calculations of λ .

The whole Fischer curve as shown in figure 4.2 was reproduced by determining λ from 1 to 10 g for lamps with different fillings and geometry, see figures 4.10 and 4.11. The lamps with a burner radius of 8 mm, a burner height of 20 mm and a Hg filling ranging from 5 mg to 10 mg, are predominantly on the right side of the Fischer curve (see figure 4.10). As g increases, the axial segregation parameter λ decreases, the experiments show that this decrease is proportional to $1/g$, which is consistent with theory. The lamp with a burner radius of 4 mm, a burner height of 22 mm and a Hg filling of 2.5 mg, are clearly on the left side of the curve (see figure 4.11) as the pressure is lower and the radius narrower. A lamp containing 0.73 mg of Hg, not shown in figure 4.11, shows an axial segregation parameter that is about a factor 10 less than the parameter found for the 2.5 mg Hg lamp. This is in agreement with equation 4.9. As g increases, the axial segregation parameter λ increases for the longer, thinner lamp, with no maximum occurring before 10 g .

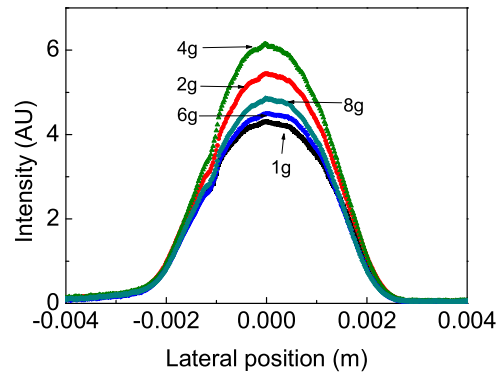
After calibration with a ribbon lamp, the radial intensity profile of Hg was used to calculate the temperature profile numerically, as described in the section 4.2. Figure 4.12 shows temperature profiles from 4 g to 10 g near the bottom of the lamp. The axis temperature is about 6500 K at 10 g . The arc clearly contracts at high g -values due to the increase of convection. The lateral profiles near the bottom of the arc shown previously indicate that the amount of Dy decreases as g is increased. Dy is largely responsible for radiation loss and accompanied by contraction of the arc [3]. Despite the fact that the amount of Dy is decreasing, an increase of g still causes the contraction to increase. Apparently the convection predominates the radiation loss with regard to contraction at these high g -values. The contraction of the temperature profiles is also in agreement with the contraction as shown by the lateral profiles.

4.5 Conclusions

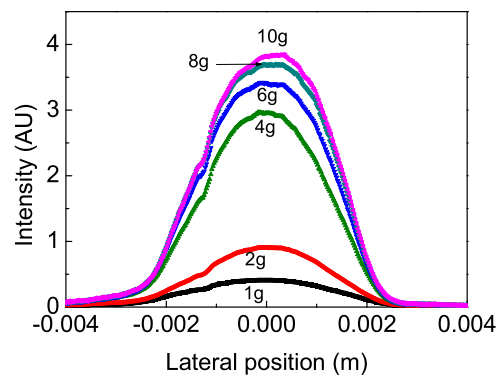
The whole Fischer curve was reproduced as the segregation parameter was determined for 1 to 10 g . The axial segregation parameter λ was calculated as a function of g from the atomic lateral profiles for lamps of different pressure and geometry. The experimental data follows the left and right side of the theoretical Fischer curve.



(a)



(b)



(c)

Figure 4.8: Ionic lateral profiles for the ionic line at 402.44 nm, The lamp filling was 10 mg Hg and 4 mg DyI₃ at three different axial positions. (a) near the bottom at $z/Z=27,5\%$, (b) at the centre at $z/Z=50\%$, (c) near the top at $z/Z=72,5\%$ where $Z=20\text{mm}$. Although the intensity was not calibrated, the measurements done at the same wavelength are absolute with respect to each other.

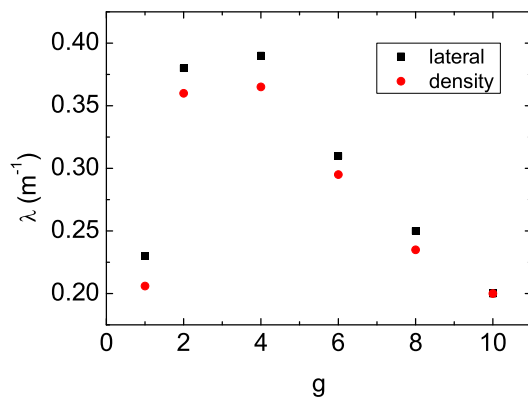


Figure 4.9: Fischer curve for a lamp containing 5 mg Hg 4 mg DyI₃ calculated using the lateral intensity profile and the radially resolved density profile.

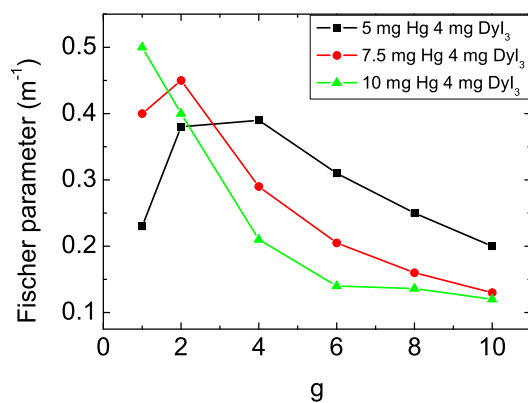


Figure 4.10: Fischer curve for lamps containing different Hg fillings, namely 5, 7.5 and 10 mg. In all cases DyI₃ = 4mg. Burner height is 20 mm and burner diameter is 8 mm.

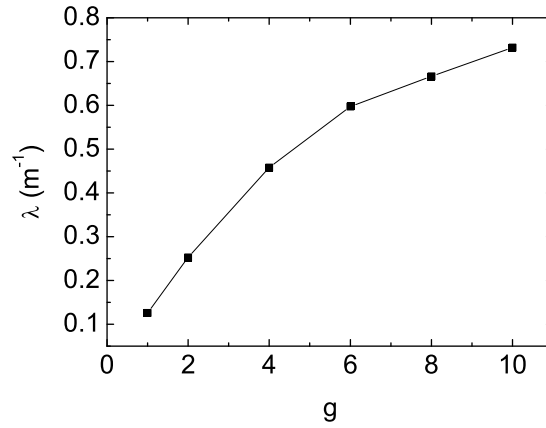


Figure 4.11: Fischer curve for a lamp containing 2.5 mg Hg and 2.5 mg DyI₃. Burner height is 22 mm and burner diameter is 4 mm.

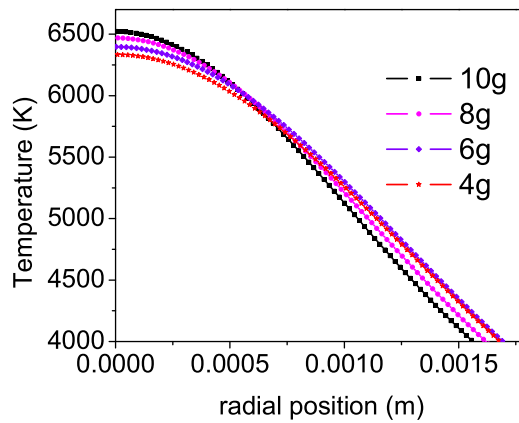


Figure 4.12: Radial temperature profile for a lamp containing 10mg Hg and 4 mg DyI₃ near the bottom, at the axial position of $z/Z=27.5\%$ of the lamp, where $Z=20$ mm.

Webcam pictures show that at higher g -values there is more mixing of the additives in the MH lamp due to an increase in convection. This is corroborated by atomic and ionic lateral profiles for lamps on the right side of the Fischer curve. The cold spot temperature decreases as g becomes higher. The increase of convection causes the arc to contract near the bottom of the lamp. Near the top of the lamp the arc broadens. Radial temperature profiles were determined from the Hg radial profiles for different g . Axis temperature at 10 g is about 6500 K . Contraction of the arc caused by convection predominates contraction caused by radiation loss near the bottom of the lamp.

Future work includes comparison of experimental results with a numerical model, the results provide excellent means for the testing of such a model.

4.6 Acknowledgements

T.N. acknowledges support from Technologiestichting STW (project ETF. 6093), ESA, NASA, COST (project 529), Senter Novem, SRON, the Dutch Ministries of Economic Affairs and Culture, Science and Education, Dutch Space, Verhaert, the executive board of the Eindhoven University of Technology and the Design and Engineering facilities of the Eindhoven University of Technology (GTD).

Bibliography

- [1] Lister G G, Lawler J E, Lapatovich W P and Godyak V A 2004 Rev. Mod. Phys. **76**, 541
- [2] Fischer E 1976 J. Appl. Phys. **47**, 2954
- [3] Nimalasuriya T, Flikweert A J, Haverlag M, Kemps P C M, Kroesen G M W, Stoffels W W and Van der Mullen J J A M 2006 *J. Phys D: Appl Phys* **39** 2993 **see chapter 3**
- [4] Flikweert A J, Van Kemenade M, Nimalasuriya T, Haverlag M, Kroesen G M W and Stoffels W W 2006 J.Phys.D **39**, 1599
- [5] Stoffels W W, Haverlag M, Kemps P C M, Beckers J and Kroesen G M W 2005 Appl. Phys. Lett. **87** 1
- [6] Nimalasuriya T, Pupat N B M, Flikweert A J, Stoffels W W, Haverlag M and Van der Mullen J J A M 2006 J. Appl. Phys. **99** 053302 **see chapter 2**
- [7] Zhu X 2005 Ph.D. thesis *Active spectroscopy on HID lamps*, Eindhoven University of Technology
- [8] Van der Mullen J J A M 1990 Phys. Rep. **191** 109
- [9] Curry J J, Sakai M and Lawler J E 1998 J. Appl. Phys. **84**, 3066
- [10] Kemps P C M, 2004 Master's thesis *An experimental study of the radial additive density and plasma temperature profiles, and the effect of this on the integral light output of metal halide lamps as a function of gravity* Eindhoven University of Technology
- [11] Mitchner M and Kruger C H Jr 1973 *Partially ionized gases*, 1st ed. (John Wiley and Sons).
- [12] Kurucz R L and Bell B 1993 *Atomic Line Data CD-ROM No 23* (Cambridge, MA: Smithsonian Astrophysical Observatory)
- [13] Wickliffe M W and Lawler J E 2000 J. Quant. Spectrosc. Radiat. Transfer **66**, 363
- [14] http://www.thespectroscopynet.com/Theory/Partition_Functions.asp
- [15] Fischer E 1978 *Influences of External and Self-Magnetic Fields on the behaviour of discharge lamps*, Philips GmbH Forschungslaboratorium Aachen Lobornotiz nr 13/78.
- [16] Elenbaas W 1951 *The high pressure mercury vapour discharge*, 1st ed., (North-Holland publishing company)
- [17] Benck E C, Lawler J E and Dakin J T 1989 J. Opt. Soc. Am. B **6**, 11
- [18] Stoffels W W, Baede A H F M, Van der Mullen J J A M, Haverlag M and Zissis G 2006 Meas. Sci. Technol. **17**, N67

- [19] Flikweert A J, Nimalasuriya T, Groothuis C H J M, Kroesen G M W and Stoffels W W
2005, J. Appl. Phys. **98** 073301

Metal-halide lamps at microgravity, experiments and model

Abstract. The results from optical emission spectroscopy experiments of metal-halide lamps under the micro-gravity conditions on board the international space station are compared to the results of a numerical LTE model constructed with the platform Plasimo. At micro-gravity there is no convection which allows for easier modelling and for a separate study of the diffusion-induced radial segregation effect, undisturbed by convection. The plasma parameters that were experimentally determined and compared to the model were the Dy atom and ion density, the Hg ion density and the temperature.

The model and experiments applied to a reference lamp burning on a plasma mixture of DyI₃ and Hg were found to be in reasonable agreement with each other. The cross-section for electron-Hg collisions was studied, it was found that the Rockwood values give the correct results. Experimental results guided a sensitivity analysis of the model for the Langevin cross-sections. The ratio of the ion densities Hg^+/Dy^+ was found to be extremely sensitive for the cross section of the elastic interaction $\sigma(Hg, Dy^+)$ between the Dy ion and the Hg atom. The sensitivity analysis suggests that equating $\sigma(Hg, Dy^+)$ to a value that is 10% higher than the Langevin cross-section is the best choice. We also found deviations from LTE in the outer regions of the plasma for relative radial positions of $r/R > 50\%$.

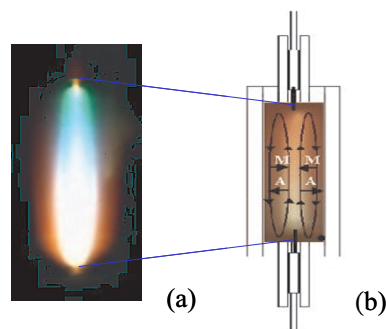


Figure 5.1: (a) Colour separation in a metal-halide lamp burner. (b) Schematic view of a metal-halide lamp; diffusion and convection of atoms (A) and molecules (M) are indicated by arrows. See figure 1.1 for full colour.

5.1 Introduction

The metal-halide lamp [1–3] combines the high luminous efficacy and good colour rendering of the fluorescent lamp with the compact and high-power characteristics of the high-pressure Hg lamps. The lamp contains a rare gas for starting and a Hg buffer gas plus a small amount of metal-halide additives such as DyI_3 , TlI , or NaI . Even though the additive density is much less than the mercury density, most light is emitted by the metals in the visible region, which results in a very high power efficiency (up to 40%). However, despite the clear advantages the growth of the metal-halide lamp has been hampered by a number of limitations. One of these is the segregation of colours [4] caused by the non-uniform distribution of the additives over the lamp due to the competition between diffusive and convective processes, see figure 5.1.

To be able to unravel the complex interaction between convection and diffusion, experiments under micro-gravity conditions have been performed at the international space station. In absence of gravity, convection is eliminated, so that the effect of diffusion can be studied exclusively and the problem is greatly simplified. The metal-halide lamp in micro-gravity is therefore easier to model. By comparing the model results to the experiments we can gain insight into the complex transport phenomena in the metal-halide lamp. The experiments verify the model results, whereas the model aids the interpretation of the experimental results. The experiments are part of a poly-diagnostic study [5–11] of the metal-halide lamp.

In this paper we present the comparison between the experiments performed on metal-halide lamps under micro-gravity conditions and a numerical model. The experiments were performed in the micro-gravity environment of the international space station (ISS). The lamp was investigated by means of optical emission spectroscopy, which yields line intensities of the species Hg, Dy and Dy^+ . From the calibrated Hg line intensity measurements we constructed radial temperature profiles. By combining the temperature profile with the calibrated line intensities for Dy we obtained absolute radial density distributions of the

Dy and Dy⁺ systems. All measurements were done for different powers ranging from 70 to 150 W. The results were reported in [9].

Metal-halide lamps come in various shapes and sizes. In order to cross-compare results of the various experiments done on metal-halide lamps and to compare the results from models to the experiments a reference lamp has been defined within the framework of the European project COST-529 [12]. The lamp was filled with an Hg buffer gas and one salt, i.e. DyI₃. This lamp has a relatively simple salt system and therefore the results are easier to compare with the results of the numerical model. We base our models on this lamp geometry. The simulation platform used to construct this model is called Plasimo and is described in [13–16]. The model simulated the lamp operating with the following conditions, an electrode distance of 18 mm, a power of 130 W and a Hg pressure of 12 bar.

There are a number of input-parameters that are not well known, such as the vapour pressure of the metal-halide salt at the cold-spot position, the transition probabilities and the cross-sections for the elastic collisions between charged and neutral particles. The latter is found to be determinative for the segregation phenomenon. The sensitivity of the model results for the elastic collisional cross-section for the Dy ion and Hg atom were tested. Because the cross-sections for the elastic collisions between the Dy ion and the Hg atom are unknown, the Langevin cross-section [17] was used. The sensitivity of this approximation is investigated.

This chapter is organized as follows. Section 5.2 describes the segregation phenomenon. Section 5.3 gives an account of the experiment. Section 5.4 illustrates the model. Results from both experiment and model are presented and discussed in section 5.5. These results include the comparison between model and experiment of the radial profiles of the arc temperature and absolute atomic and ionic densities of Dy. Finally, section 5.6 offers conclusions and recommendations for future work.

5.2 De-mixing

When the metal-halide lamp is operated, the Hg is entirely vaporised forming the buffer-gas, whereas the few milligrams of DyI₃ additive does not evaporate completely, leaving a liquid salt pool at the coldest spot at the burner wall. The additive molecules diffuse from the relatively cool wall (~ 1200 K) toward the hot region (~ 6000 K) of the arc where they dissociate. At the centre the atoms are ionised and excited. As Dy atoms diffuse back to the wall they encounter I atoms in the cooler gas near the walls and recombine back to molecules [1].

Three principal regions can therefore be identified within the radial density distribution of elemental Dy [10] (see Figure 5.2). These are 1) the region near the wall where DyI₃ molecules are predominant, 2) the mantle region between the wall and the arc core where Dy atoms predominate, and 3) the core where the Dy is almost completely ionized in the form of Dy⁺. The molecules DyI₂ and DyI are relatively unstable and do not have a dominant presence in any region of the discharge.

When burned vertically, the discharge emits light that is non-uniform in colour along it's

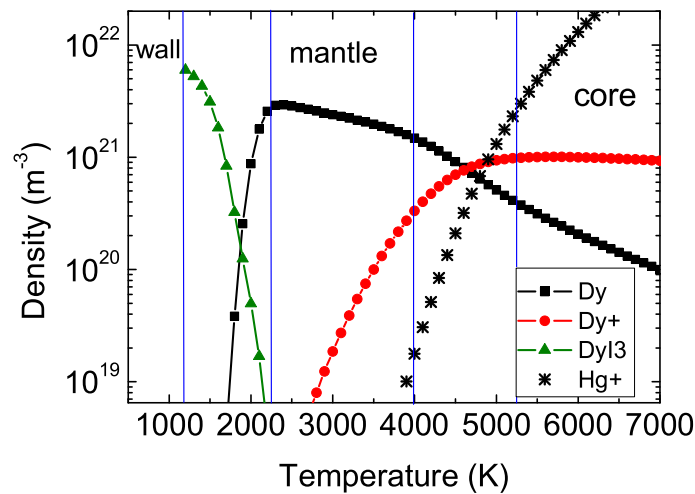


Figure 5.2: Theoretical density distribution of Dy atoms, ions and molecules, and Hg ions as a function of temperature at the midplane of a metal-halide lamp. For clarity, DyI₂ and DyI have been omitted.

axis. This colour segregation is caused by the interplay between convection and diffusion which ultimately determines the distribution of the plasma species. Let's first consider the radial distribution. The temperature profile, which is high in the centre and rapidly decreases towards the wall, leads to a hollow profile for the mass density distribution due to the ideal gas law. Another mechanism that influences the radial distribution of elemental Dy is diffusion. The atoms and molecules have different diffusion velocities. The smaller and lighter Dy atoms diffuse faster outward than the larger and heavier molecules (DyI, DyI₂, DyI₃) diffuse inward. This difference in diffusion velocity results, in steady-state, in an even more hollow profile of the elemental density of Dy; this effect is called radial segregation [4]. Ambipolar diffusion [19], in particular, causes the ions to diffuse out of the core faster than neutral atoms or molecules diffuse inwards.

The axial distribution of the species is dominated by convection, which causes the hot gas to move upwards in the hot centre of the arc and downwards along the cool wall of the lamp. This movement of the bulk gas drags the high concentration of elemental Dy near the wall downwards, whereas the lower concentration of Dy in the centre, caused by the radial segregation, is dragged upwards. As a consequence, a high density of elemental Dy accumulates at the bottom of the arc, a phenomenon which is known as axial segregation [4]. The combination of radial and axial segregation is shown in figure 5.1(b). The latter obviously only occurs in presence of convection. Since there is no convection under microgravity conditions axial segregation does not occur, but radial segregation does.

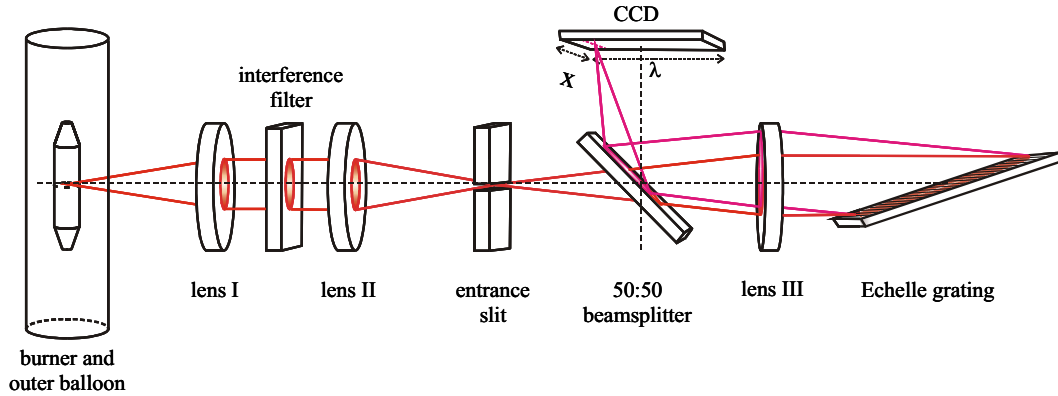


Figure 5.3: Setup used for the ISS measurements. It is an Echelle type spectrometer in Littrow configuration, the imaging lens (III) is used for the collimation of both the un-dispersed beam of light as well as the reflected dispersed beam of light.

5.3 The experiment

In the ISS experiment, emission spectroscopy was performed on a metal-halide lamp [12], which is, as mentioned above, a reference lamp. The lamp consists of a quartz burner of 20 mm in length and 8 mm in inner diameter and a transparent quartz vacuum outer bulb. The burner is made of quartz in order to make the arc optically accessible. The distance between the electrodes is approximately 18 mm. The lamp is driven by a 150 W Philips Dynavision DALI ballast with a 83 Hz square wave current profile, and operated at different input powers ranging from 70 to 150 W in steps of 20 W.

An Echelle-type spectrometer was used as there is need for a robust and compact setup with no moving parts for the experiments at micro-gravity. The downside is that only a few lines could be analysed. A schematic of the Echelle-type spectrometer is shown in figure 5.3 [9] [20]. Its main components are an Echelle grating with a high blaze angle (74°), an interference filter for the selection of the desired wavelength interval and a CCD camera for imaging. This spectrometer was used to measure the absolute intensity of three lines of three different systems. These are the 579.07 nm line of the atomic Hg system, the 642.19 nm and the 402.44 nm line of the atomic and ionic Dy system respectively; shortly denoted by the Dy and Dy^+ system. The Hg line is used for the determination of the radial temperature distribution, and combined with the lines of Dy and Dy^+ the densities of the Dy and Dy^+ systems can be determined.

The procedure is as follows, first the transition-integrated intensity of the line emitting species is determined as a function of lateral position. After Abel inversion this gives the radiant power of the transition

$$U_{pq}(r) = n_p(r)A(p, q)h\nu_{pq} \quad (5.1)$$

from which, $n_p(r)$, the radial distribution of the radiating level can be determined since the transition probability $A(p, q)$ and the photon energy $h\nu_{pq}$ of the transition are known.

The density of the system to which radiating level belongs can now be determined using the Boltzmann relation [9] [18]

$$n_s(r) = \frac{U_{pq}(r)Q(T(r))}{g_p A(p, q) h\nu_{pq}} \exp\left(\frac{E_p}{kT(r)}\right), \quad (5.2)$$

where n_s is the system density of an emitting atom or ion, g_p the statistical weight of upper level p , $A(p, q)$ is the transition probability of the transition, $h\nu_{pq}$ the energy of the emitted photon, E_p the excitation energy of the radiating level, k the Boltzmann constant and T is the temperature. $Q(T)$ is the partition function of the considered atomic or ionic system. U_{pq} is the radiant power and determined experimentally, while $Q(T)$, g_p , A can be found in literature [23–25].

In case of the 579 nm transition of Hg this expression can be used to find the radial distribution of the temperature $T(r)$. This is done by replacing the left-hand-side of equation 5.2 by $p/kT(r)$ which is justified since the atomic Hg system delivers the majority of particles in the lamp so that Daltons law, $p = \sum nkT$, reduces to $p = n_{Hg(r)}kT(r)$. This bulk pressure can be assumed to be constant over the lamp. Since $U_{pq}(r)$ is known as a function of radial position we can use equation 5.2 to determine the temperature as a function of radial position provided the pressure is known. Since this is not the case we follow an iterative procedure. First a guessed value of p is inserted which gives, using the measured $U_{pq}(r)$, a radial $T(r)$ distribution. In the second step we determine $n_{Hg}(r) = p/kT(r)$ which, integrated over the whole volume, gives the total number of mercury atoms N_{Hg} in the discharge. In the last step this number, multiplied with the mass of a Hg atom, thus $N_{Hg}m_{Hg}$, is compared to the filling mass M_{Hg} . The mismatch $M_{Hg}/N_{Hg}m_{Hg}$ is used to correct the pressure. With this new pressure-value we can repeat steps 1 till 3 again. This is done until convergence is reached.

Calculation of the radial density profiles is as follows. First the emission of the line of interest is measured as a function of lateral position. This profile is then Abel inverted into a radial intensity profile. The next step depends on the species of which the emission line is measured.

In case of the 579 nm line of Hg, the intensity is calibrated and then the absolute radial intensity profile is used to numerically determine the temperature profile. In case the atomic or ionic lines of Dy are measured, the temperature profile is combined with the calibrated radial intensity profile of the additive into an absolute radial system density profile using equation 5.2

5.4 The model

A description of the model has been published in [15] and [16] where it has been applied to a metal-halide lamp based on a mixture of Hg and NaI. In the following a brief summary is given in order to give an outline of the basic equations and to highlight changes made to the model since these publications. The most significant change is the substitution of NaI by DyI₃.

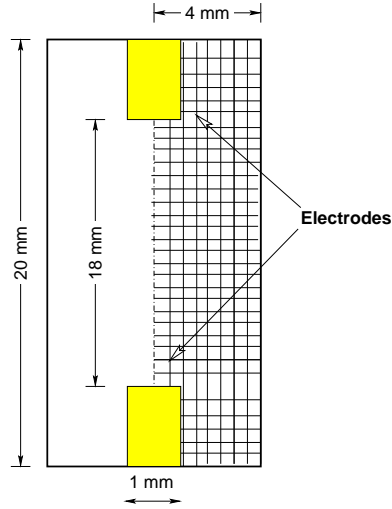


Figure 5.4: Schematic picture (not to scale) of the grid with respect to the inner burner.

5.4.1 Geometry of the problem

The model lamp has a distance between the electrodes of 18 mm, the length of the inner burner is 20 mm, and the diameter is 8 mm. We assume that the discharge is axially symmetric. The models thus uses a two dimensional rotationally symmetric grid. Figure 5.4 gives a schematic view of the geometry of the grid and the discharge. All equations are discretized on a structured finite volume mesh.

5.4.2 Basic equations

We will give a short overview of the basic equations solved in the model. More details are presented in [15] and [16]. The model assumes Local Thermal Equilibrium (LTE) [18]. The lamp is operated at a constant power of 130 W using a mixture of Hg and DyI₃.

Energy balance

All modules come together in the energy balance to calculate the plasma temperature. The temperature, in turn, strongly influences the transport coefficients, composition, flow and radiation. The temperature is given by

$$\nabla \cdot (C_p \mathbf{v} \nabla T) - \nabla \cdot (\lambda_c \nabla T) = P + Q_{rad}, \quad (5.3)$$

where C_p is the heat capacity at constant pressure, \mathbf{v} the bulk velocity, λ_c the thermal conductivity, $P = \sigma_{el} E^2$ the Ohmic dissipation, and Q_{rad} the energy source term due to radiation transport. Viscous energy source terms are neglected. The electrodes are assumed to have a surface temperature of 2900 K and the rest of the wall a temperature

of 1200 K. The term Q_{rad} is the result of 2D ray-tracing. We solve the equation for the radiation intensity I_ν [26]

$$\frac{dI_\nu}{ds} = j_\nu - \kappa I_\nu, \quad (5.4)$$

with j_ν the local emission coefficient and κ the local coefficient for absorption along rays passing through the discharge [16]. The radiation loss term is given by [26]:

$$Q_{rad} = \int_\nu \left(-4\pi j_\nu + \int_{4\pi} \kappa I_\nu d\Omega \right) d\nu, \quad (5.5)$$

with ν the frequency. For the precise form of Q_{rad} for a DyI₃-Hg mixture we refer to [35].

Particle transport

Since we assume LTE, the particle densities may be described by the local temperature, pressure and elemental composition. Elemental pressure is defined as the pressure that contains all molecular, atomic and ionic contributions of a particular element. The elemental pressure p_α for the element α can be written as

$$p_\alpha = \sum_i R_{i\alpha} p_i, \quad (5.6)$$

with p_i the partial pressure of the species i , and $R_{i\alpha}$ the stoichiometric coefficient [15]. We solve a conservation equation for the elemental pressure

$$\nabla \cdot \left(\frac{D_\alpha}{kT} \nabla p_\alpha + \frac{p_\alpha}{kT} \mathbf{c}_\alpha \right) = 0, \quad (5.7)$$

with an effective diffusion coefficient D_α [15]

$$D_\alpha = p_\alpha^{-1} \sum_i R_{i\alpha} D_i p_i \quad (5.8)$$

and a pseudo convective velocity c_α [15].

The diffusion coefficient D_i is calculated from the binary diffusion coefficients D_{ij} by

$$D_i = \left(\sum_{j \neq i} (p_j/p) / D_{ij} \right)^{-1}. \quad (5.9)$$

The binary diffusion coefficient for the diffusion of species i through species j is given by [36, page 486] and depends on the differential cross-section.

In-situ measurements of the elemental pressure at the walls under micro-gravity conditions are not possible, therefore we assume a Dy elemental pressure at the wall of 517 Pa and an I elemental pressure of 4268 Pa. These vapour pressures were determined with x-ray induced fluorescence measurements at 1g [10]. These are assumed to give a good estimation of the vapour pressure at the walls and used to fix the boundary conditions.

Ohmic heating

The power to the plasma is supplied by ohmic heating. We solve the Poisson equation in the form:

$$\nabla \cdot (\sigma_{el} \nabla \Phi) = 0, \quad (5.10)$$

with Φ the potential. From the potential Φ we can derive the electric field $\mathbf{E} = -\nabla\Phi$ and the current density $\mathbf{J} = \sigma_{el}\mathbf{E} = -\sigma_{el}\nabla\Phi$. The following boundary conditions are imposed:

1. There is no current through the walls, resulting in a homogeneous Neumann boundary condition ($\frac{\partial\Phi}{\partial n} = 0$).
2. One electrode is kept at zero potential, which leads to a Dirichlet condition $\Phi = 0$ at that electrode.
3. The potential of the other electrode is initially put at 100 V. This value is adjusted during the iteration process and determined by the fact that the power dissipated in the discharge equals 110 W. This is equivalent to the actual lamp power of 130 W of which 20 W is consumed by electrode losses and 110 W by ohmic dissipation of the discharge.

The selection of cross-sections

In the basic equations, summarized in the previous section, important roles are played by various transport coefficients, such as the diffusion coefficients D_i , the thermal conductivity λ_c and the electrical conductivity σ_{el} . These transport properties are calculated from collision integrals that are based on differential cross sections [27].

Ideally, one would like differential cross-sections for every possible collision between particles in the plasma. In practice such data is difficult to gather or calculate since for only a few interactions energy-dependent integral cross-sections σ_{ij} are available. When available these are used in the model. For collisions for which such data cannot be found approximations have to be used. The collisions can be classified along the following categories:

1. Charged - charged collisions; in this case the shielded Coulomb cross-sections is a good and generally applicable approach [19, page 55],
2. Neutral - neutral collisions; there where dedicated cross-section values are not available these interactions are described as hard sphere collisions,
3. Charged - neutral collisions; this category is the most complicated since, in principle, a full quantum mechanical (QM) treatment is needed in which, for instance, the effect of the Ramsauer minimum has to be taken into account. For each pair of interacting particles the QM aspects are different. If results of experiments or QM calculation

are not available the use of the Langevin cross-section is the only option. The formula for the Langevin cross-section reads [17]

$$\sigma_{ij} = \sqrt{\frac{\pi \alpha_p q^2}{\mu_{ij} \epsilon_0 (|\mathbf{v}_i - \mathbf{v}_j|)}}, \quad (5.11)$$

with α_p the dipole polarizability of the neutral species, q the charge of the charged species, ϵ_0 the permittivity of free space and μ_{ij} the reduced mass $\mu_{ij} = m_i m_j / (m_i + m_j)$ of the system of colliding particles.

When considering the influence of the cross-section on the values of the transport coefficients D_i , λ_c and σ_{el} it is important to note that Hg atoms form the most dominant species in the discharge; all other species are present in small concentrations.

We begin with the electrical conductivity σ_{el} that is mainly determined by the elastic interactions between electrons with Hg atoms. This electron-Hg interaction is of the third category but fortunately the corresponding cross-section is well known and it is generally expected that the values from Rockwood [38] are correct within a few percent. We studied whether this is indeed the case by comparing the results using Rockwood values and Langevin cross-sections. As the value of this cross-section determines the lamp resistance and the ohmic dissipation we calculated the voltage drop over the lamp when the ohmic dissipation equals 110 W. This was done for two cases, one based on the Rockwood values and the other on the Langevin cross-section. Using the Rockwood values the model predicts a voltage drop of 99 V, which is consistent with the measured value. The calculations done with the Langevin cross-section, however, produces a voltage drop of 71 V, which is much too low. We may therefore conclude that the model gives a good description of the potential distribution over the lamp and the corresponding ohmic heating by using the Rockwood values.

Next we study the choice of cross-section for the thermal heat conductivity λ_c . Due to the low elemental concentration of Dy and I we can neglect the heat generation that is liberated in the formation of DyI_x molecules. The reactive part of heat conductivity can therefore be neglected and only the frozen part remains (see [27]) which is determined by the collisions of Hg atoms mutually. These Hg-Hg collisions are of the second category and experimental results given in [36] confirm that the hard sphere approach is valid here.

Finally, we look at the diffusion of Dy. The diffusion of Dy containing species is determined by the collisions with Hg atoms. In case of the neutral species we deal with the second category for which the hard sphere approach can be used. Much less clear are the collisions between Hg atoms and Dy ions. These are of the third category and since there are no QM or experimental results available we have to use the expression of the Langevin cross-section. However, it is known from literature that this is not always a good approximation and errors in the order of 30% or more [39] are frequently reported. To study the impact of the $\sigma(Hg, Dy^+)$ -value on the model results we performed two sets of calculations, one with the Langevin cross-section σ_{LV} and one with a value that is 20% larger, i.e. $1.2 * \sigma_{LV}$. In this way we can determine the importance of this Hg-Dy⁺ cross-section and test the possible errors introduced by the approximation.

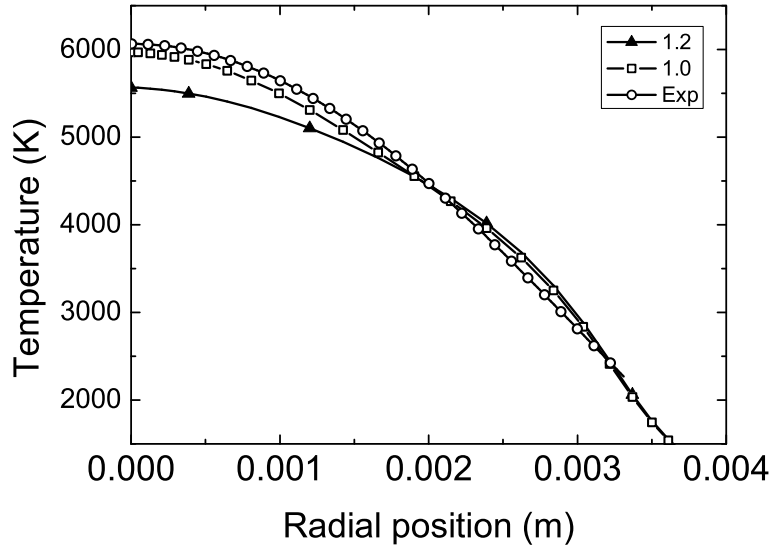


Figure 5.5: Radial temperature profile for a lamp containing 10 mg Hg and 4 mg DyI_3 at the midplane of the lamp. The numbers 1.0 and 1.2 refer to the two Langevin cross-sections that were used, the normal Langevin cross-section σ_{LV} and $1.2 \cdot \sigma_{LV}$. Exp denotes the experimental results.

5.5 Results and discussion

The experiment and model results are compared in this section. Both model and experiments were done for a lamp in micro-gravity, so without convection, operating at 130 W (of which 110 W dissipated in the discharge and 20 W spend on electrode losses) and containing 10 mg Hg and 4 mg DyI_3 . The sensitivity of the model results for the choice of $\sigma(\text{Hg}, \text{Dy}^+)$ is examined. To that end two different cross-sections were used for the model, namely the Langevin cross-section σ_{LV} and $1.2 \cdot \sigma_{LV}$. This discussion will follow the line of the theory presented in section 5.3 where the three atomic systems were introduced, namely the Hg atom, the Dy ion and Dy atom. The Hg-system is used for the determination of the temperature, and the atomic and ionic Dy system for the spatial distribution of Dy atoms and ions and the radial Dy segregation.

The temperature profile

The temperature profile as deduced from the Hg line is given in figure 5.5 and shows that the model based on the Langevin cross-section is in good agreement with the experiment. Both profiles have an axis temperature of 6000 K and nearly the same shape. If we take $\sigma(\text{Hg}, \text{Dy}^+) = 1.2 \cdot \sigma_{LV}$ this results in a broader temperature profile with a lower axis

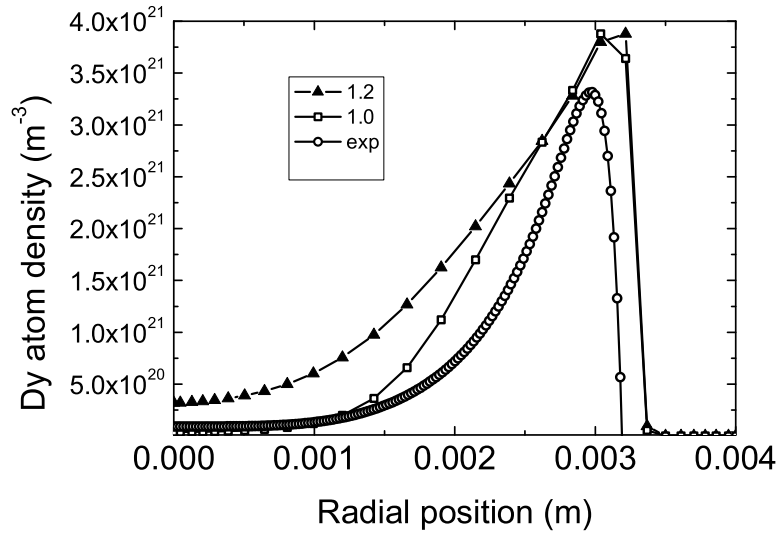


Figure 5.6: Radial Dy atom system density profile for a lamp containing 10 mg Hg and 4 mg DyI₃ at the midplane of the lamp. The numbers 1.0 and 1.2 refer to the two Langevin cross-sections that were used, the normal Langevin cross-section σ_{LV} and a value that is 20% larger: $1.2 \cdot \sigma_{LV}$. Exp refers the experimental results.

temperature. The reason why the higher $\sigma(Hg, Dy^+)$ value influences the temperature profile is the following. By increasing $\sigma(Hg, Dy^+)$ the ambipolar diffusion in the central region is being hampered which causes the Dy particles to be accumulated in the centre. The temperature then decreases slightly as Dy has a lower ionisation potential than Hg (5.93 eV versus 10.43 eV). However, the change in the temperature distribution remains in the error margin of 10% [9] so that no conclusions can be drawn about the optimum value for $\sigma(Hg, Dy^+)$ from the temperature value.

The Dy atom

Figure 5.6 shows the absolute system density of atomic Dy for both the experiment and two model results for $\sigma(Hg, Dy^+) = \sigma_{LV}$ and $\sigma(Hg, Dy^+) = 1.2 \cdot \sigma_{LV}$. Both numerical and experimental curves have a steep slope at nearly the same radial position (about 3.3 mm) where the Dy atom associates into the DyI₃ molecule, see figure 5.2. The experimental curve has a steep slope partially because, in order for the Abel fit to yield physical results, the fit was forced to zero near the edges of the lateral profile [9]. It shows that the experimental and theoretical values of the maximum of the atomic Dy system agree with each other within 20%. This is in fairly good agreement in view of the fact that the uncertainty of the transition probability from which the density is determined is in the order 20%. Also important is the uncertainty related to the cold spot temperature. A small change in this

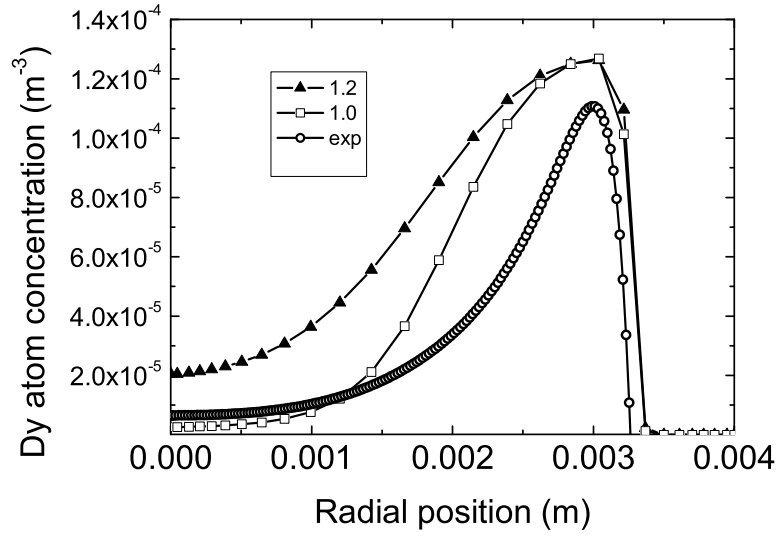


Figure 5.7: The atomic Dy concentration obtained by dividing the Dy atom density by the Hg density. The lamp contains 10 mg Hg and 4 mg DyI₃ at the midplane of the lamp. The numbers 1.0 and 1.2 refer to the two Langevin cross-sections that were used, the normal Langevin cross-section σ_{LV} and $1.2 \cdot \sigma_{LV}$. Exp denotes the experimental results.

temperature will lead to a significant variation of the elemental Dy density.

By dividing the Dy atom density by the Hg atom density distribution (which is the bulk species) the atomic Dy concentration is found, see figure 5.7. The atom concentration gives an indication of the radial segregation. The concentration profile clearly shows radial segregation for both experiment and model. Compared to the experiment, the model predicts more profound radial segregation. However, by increasing the cross-section from σ_{LV} to $1.2 \sigma_{LV}$ we see that the theoretical central Dy concentration increases drastically; with more than a factor of 8. This implies that the amount of radial segregation is diminished and becomes much smaller than what is found experimentally. By increasing the cross-section, the diffusion is reduced, resulting in a decreased radial segregation.

The above clearly shows that the atom concentration at the centre is very sensitive to the choice of the cross-section; an increase of the cross-section by 20% leads to an increase of the central atomic density of a factor of 8.2 and the figure suggests that $\sigma(Hg, Dy^+)$ will have a value somewhat larger than σ_{LV} but smaller than $1.2 \cdot \sigma_{LV}$. However, care should be taken with this theory-experiment comparison since the experimental values result from an Abel inversion which is quite sensitive for errors at the centre of a hollow profile.

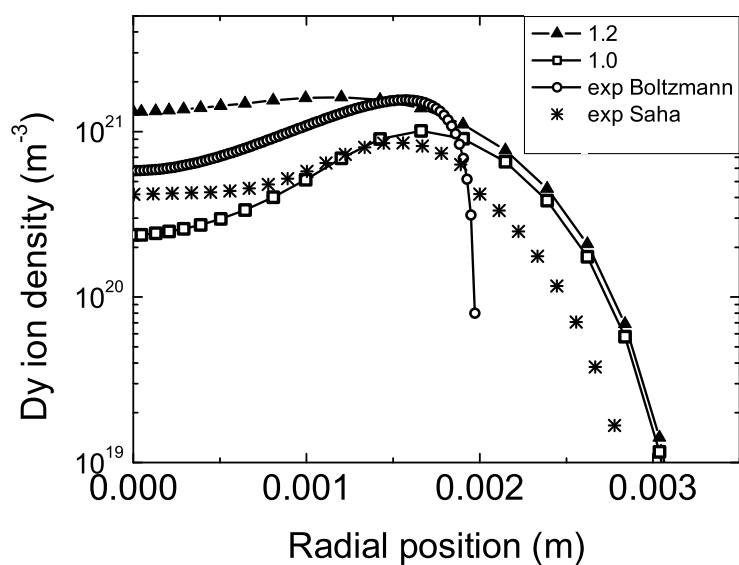


Figure 5.8: Radial Dy ion system density profile for a lamp containing 10 mg Hg and 4 mg DyI₃ at the midplane of the lamp. The numbers 1.0 and 1.2 refer to the two Langevin cross-sections that were used, the normal Langevin cross-section σ_{LV} and $1.2 \cdot \sigma_{LV}$. Exp denotes the experimental results. The experimental value for the Dy ion density was determined by either Boltzmann, denoted as exp Boltzmann; or by Saha, then denoted by exp Saha.

The Dy ion

The comparison of the model and experiment with respect to the Dy ion density is given in figure 5.8. We first focus on the central region where we find that, just as the Dy atom density, the theoretical value of central ion density is very sensitive to the value of $\sigma(Hg, Dy^+)$. The change from σ_{LV} to $1.2 \cdot \sigma_{LV}$ leads to an increase of the central density with a factor 5.4. This is smaller than in the atomic case where a ratio of 8.2 is found.

The reason that both the Dy atom and ion density increase is that, as a consequence of the decrease in the ambipolar diffusion coefficient, the amount of Dy is more easily 'trapped' in the centre. This causes the temperature in the centre of the discharge to become lowered (as shown in figure 5.5) which as a result will cause the Saha balance between the atomic and ionic system to shift with respect to the atomic system. This is why the atomic Dy increases more strongly than the Dy ion as $\sigma(Hg, Dy^+)$ is being increased.

Leaving the central region and moving outwards we see that the experimental Dy ion density in figure 5.8 has a much steeper slope than what the model predicts. In part this is caused by the Abel fitting as mentioned before. However, a more important aspect is the validity of LTE away from the centre. The experimental Dy ion density as shown in figure 5.8, denoted by "exp Boltzmann", is based on the application of the Boltzmann balance (equation 5.2) in the ionic system; this gives the Dy ion system density using the emission of a Dy ion line.

However, since the charge of the core of the ion system ($Z = 2$) is twice as large as that of the atom system ($Z=1$), we can expect that the transition frequency induced by electron collisions will be smaller (this scales as Z^{-2}) [18] whereas the radiative decay transition (scaling as Z^4) [18] will be higher than in a comparable atomic system. This means that as n_e decreases (in the direction toward the wall) the electron-ruled Boltzmann balance of excitation and de-excitation will no longer be in equilibrium. The spontaneous emission will then become the most dominant de-population process and the level is in the so-called Corona balance [18]. This causes the density of radiating states to decline. This implies that the ionic system density as deduced from these levels will decline as well.

We first investigate a possible departure from equilibrium by calculating the ion density using the Saha relation between the atomic and ionic system. This density is in fact based on the atomic radiation and thus the atomic system. For this system we can expect that, due to the lower Z value ($Z=1$), it will not easily be effected by a drop in n_e . The Saha relation between n_i , the system density ion stage, and n_s , the system density of Dy atoms, reads

$$\frac{n_e n_i}{n_s} = 2 \frac{Q_i}{Q} \left(\frac{2\pi m_e k T}{h^2} \right)^{3/2} e^{-I_p/kT} \quad (5.12)$$

where Q is the partition function for the neutral species and Q_i the partition function for the ion, m_e the electron mass, T the temperature, I_p the ionisation potential of the atomic ground state, k the Boltzmann and h the Planck constant. The density of the Dy ion system can be found by inserting in this equation for n_e the sum of the Hg ion and the Dy ion density and for the atom density n the measured Dy atoms as shown in figure 5.6.

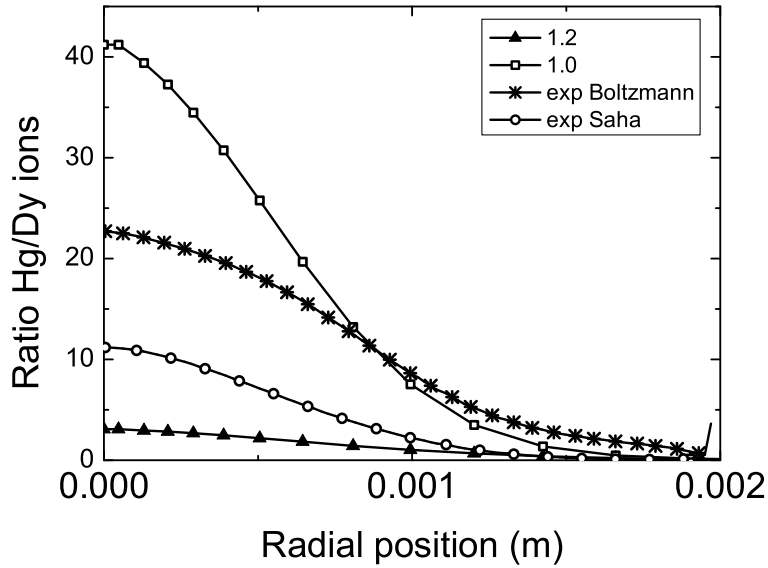


Figure 5.9: The Hg ion and Dy ion ratio for a lamp containing 10 mg Hg and 4 mg DyI₃ at the midplane of the lamp. The numbers 1.0 and 1.2 refer to the two Langevin cross-sections that were used, the normal Langevin cross-section σ_{LV} and $1.2 \cdot \sigma_{LV}$. Exp denotes the experimental results. The ratio is calculated from either the measured Dy ion density (calculated from Boltzmann) or from the measured Dy atom density (calculated from Saha).

The results of this equation given in figure 5.8, denoted with "exp Saha" show a much better agreement between the calculated ion density using Saha's equation and the model results in the outer region. In contrast to the curve found by employing the Boltzmann relation (equation 5.2), the Saha value of the ion system density declines more gradually in the outer region. There is a factor of 2 difference between the Saha calculation and the model results. This may be caused by a number of factors. First, there is more atomic Dy in the model than in the real lamp as was shown in figure 5.6. Second, there may be an error in the transition probability, leading to an error in the atom density calculated with equation 5.2. Finally, an error may be introduced by the Abel inversion.

The Hg/Dy ratio

As stated above in dealing with the Saha equation, we have to take n_e equal to the sum of the Hg ion and the Dy ion density¹. In contrast to commercial lamps with PCA tubes for which the Dy vapour pressure is higher than in our model lamp used in the experiments we can not neglect the contribution of the Hg ions. In fact it was found experimentally from

¹this was not the case in [8] and [9], where $n_e = n_{Hg+}$

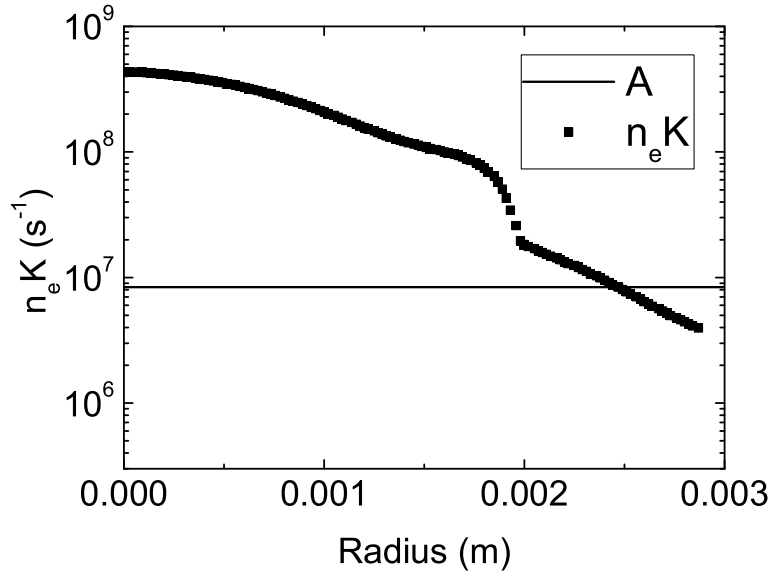


Figure 5.10: The collision frequency $n_e K$ compared to the radiative frequency which is represented by the transition probability A .

the Hg^+/Dy^+ ion ratio [9] that the Hg ions dominate in the centre, see figure 5.9 where the experimental values of the Hg^+/Dy^+ ratio are given. Two ratio's are shown, one of which the Dy ion calculation is based on Boltzmann (cf. equation 5.2) the other of which the calculation is based on Saha (cf. equation 5.12). These are compared to two model results based on $\sigma(\text{Hg}, \text{Dy}^+) = \sigma_{LV}$ and $\sigma(\text{Hg}, \text{Dy}^+) = 1.2 \cdot \sigma_{LV}$.

It is clear the model predicts the ratio Hg^+/Dy^+ to be high for a normal Langevin cross-section. At higher cross-section ($1.2 \cdot \sigma_{LV}$) this ratio is much lower, as there are more Dy ions in the centre (cf. figure 5.8). A higher cross-section causes Dy ions to be accumulated in the centre so that the central temperature will decrease. This will radically reduce the number of Hg ions, as they have a much higher ionisation potential.

It can be concluded from the above that the Hg^+/Dy^+ ion ratio is the most effective parameter for finding the optimum value of $\sigma(\text{Hg}, \text{Dy}^+)$ when comparing the results of the model with that of the experiment. An advantage of using the ion ratio is that the Abel inversion is more reliable for the Dy ion than for the atom as the latter contains a hollow structure. Figure 5.9 suggests that the best value of the $\sigma(\text{Hg}, \text{Dy}^+)$ will in the order of $1.1 \cdot \sigma_{LV}$.

Departure from LTE

We now return to the topic of the rapid decay in the Dy^+ density at $r=0.002$ m as shown in figure 5.8, which was found using Boltzmann's law. The Dy ion system density is

determined by that of an excited Dy ion state which decreases rapidly due to the sudden decrease of the electron density. This under-population of the excited Dy ions has been previously reported [8] and is, as mentioned before, expected near the wall where the number of electrons is dramatically reduced. This causes the Boltzmann balance to shift to a Corona balance and this leads to a departure in LTE. A deviation from LTE in the outer region of the discharge has already been observed for the high pressure sodium lamp [40].

The transition from the Boltzmann-Saha balance to the Corona balance, happens when the collision frequency $n_e K_p$ is about equal to the radiative frequency (i.e. transition probability) A_p .

$$n_e K_p \simeq A_p \quad (5.13)$$

where A_p and $n_e K_p$ are the rates for total radiative and collisional destruction. We estimate the collision frequency by treating the Dy ion as hydrogen-like. The collision rate can then be written as [18]

$$K_p = 4\pi a_0^2 (p/Z)^4 \left(\frac{3kT}{m_e} \right)^{1/2} \quad (5.14)$$

where a_0 is the Bohr radius, Z the charge number of the core (which is 2 for the ion) and m_e the electron mass. The effective principal quantum number p of the level in question is calculated from $Z\sqrt{Ry/E_p}$ with Ry the Rydberg energy and E_p the ionisation potential of the level in question (thus in this case the energy needed for Dy²⁺ formation) [18]. For A_p we use the radiative transition probability of $A_p = 8.4 \cdot 10^6 \text{ s}^{-1}$ as used in the experiment.

The results are depicted in figure 5.10. It shows that the assumption of LTE is no longer valid after $r/R > 50\%$. This results in the excited Dy ions to be underpopulated. An under-population of the excited states with respect to Boltzmann means that equation 5.2 will underestimate the density of the ions. Thus we have found deviations from LTE. However, this departure of LTE only has a limited effect on the main plasma parameters such as the temperature and the electron density. It will also not change the spectrum emitted by the plasma substantially. This means that using an LTE model is justified to describe the phenomena in this type of lamp. When we calculate the threshold in equation 5.13 for the Dy atom we find that the Boltzmann balance still holds.

It should be realized that in the way we employ equation 5.13 a hydrogen-like system is assumed and we thus ignore the fact that the Dy ion has much more lower lying levels that will facilitate step-wise excitation instead of direct excitation from the ground level. For a proper description of the experimental results a full collisional radiative model would be needed which is beyond the scope of this study.

5.6 Conclusions

There is a reasonable agreement between model and experiment. The model is based on the following elementary parameters, the electrical conductivity is based on the electron-Hg cross-section from Rockwood, the thermal conductivity is determined from hard-sphere

collisions and the Hg-Dy⁺ collisions are determined from the Langevin cross-sections. The temperature profiles are in good agreement and are not very sensitive to the Langevin cross-section. Dy atom profiles show an abrupt transition between atom and molecule for both model and experiment. The comparison between the experiment and model results for the Dy atom concentration shows that the model predicts more radial segregation.

The ratio Hg^+/Dy^+ was found to be extremely sensitive for the cross-section of the elastic interaction $\sigma(Hg, Dy^+)$ between Dy^+ and Hg atom. The sensitivity analysis reveals that equating $\sigma(Hg, Dy^+)$ to a value that is 10% higher than the Langevin cross-section is the best choice. There is a clear discrepancy between experiment and the LTE-based model for the Dy ion density profiles. The experiment shows the Dy ion density to decrease much more rapidly. Further analysis showed deviations from LTE in the outer regions of the plasmas for relative radial positions of $r/R > 50\%$. These deviations are manifest in the excited part of the Dy^+ system that for relatively low n_e is ruled by the Corona rather than by the Boltzmann balance. However, this departure of LTE only has a limited effect on the main plasma parameters which means that using an LTE model is justified.

In order to also study the effect of convection, experiments have also been done at hyper-gravity [11] and normal gravity [10], the future plan is to compare numerical results of the model to these experiments.

Bibliography

- [1] Waymouth J, Electric discharge lamps, MIT press, Cambridge, 1971
- [2] Coaton J R, Marsden A M, Lamps and Lighting, Arnold, London, 4th edition, 1997
- [3] Lister G G, Lawler J E, Lapatovich W P and Godyak V A 2004 Rev. Mod. Phys. **76**, 541
- [4] Fischer E 1976 J. Appl. Phys. **47**, 2954
- [5] Zhu X 2005 Ph.D. thesis, Eindhoven University of Technology
- [6] Flikweert A J, Van Kemenade M, Nimalasuriya T, Haverlag M, Kroesen G M W and Stoffels WW 2006 J.Phys.D **39**, 1599
- [7] Flikweert A J, Nimalasuriya T, Groothuis C H J M, Kroesen G M W and Stoffels W W 2005, J. Appl. Phys. **98** 073301
- [8] Nimalasuriya T, Pupat N B M, Flikweert A J, Stoffels W W, Haverlag M and Van der Mullen J J A M 2006 J. Appl. Phys. **99** 053302, **see chapter 2**
- [9] Nimalasuriya T, Flikweert A J, Haverlag M, Kemps P C M, Kroesen G M W, Stoffels W W, Van der Mullen J J A M 2006 *J. Phys D: Appl Phys* **39** 2993, **see chapter 3**
- [10] Nimalasuriya T, Curry J J, Sansonetti C J, Ridderhof E J, Shastri S D, Flikweert A J, Stoffels W W, Haverlag M, Van der Mullen, J J A M 2007 J.Phys.D **40**, 2831, **see chapter 6**
- [11] Nimalasuriya T, Thubé G M, Flikweert A J, Haverlag M, Kroesen G M W, Stoffels W W, Van der Mullen 2007, J.Phys.D 2007 **40** 2839, **see chapter 4**
- [12] Stoffels W W, Baede A H F M, Van der Mullen J J A M, Haverlag M and Zissis G 2006 Meas. Sci. Technol. **17** N67
- [13] Benoy D A, 1993 *Modelling of Thermal Argon Plasmas* PhD Thesis Eindhoven University of Technology, the Netherlands
- [14] Van Dijk J 2001 *Modelling of plasma light sources* PhD Thesis Eindhoven University of Technology, the Netherlands
- [15] Beks M L, Hartgers A, Van der Mullen J J A M 2006 J.Phys.D **39**, 4407
- [16] Beks M L, Van Dijk J, Hartgers A, Van der Mullen J J A M accepted for publication
- [17] Lieberman M A, Lichtenberg A J 1994, *Principles of Plasma Discharges and Materials Processing*, Wiley & Sons, New York
- [18] Van der Mullen J J A M 1990 Phys. Rep. **191** 109

- [19] Mitchner M and Kruger Jr C H 1973 *Partially ionized gases*, 1st ed., (John Wiley and Sons).
- [20] Kemps P C M, 2004 An experimental study of the radial additive density and plasma temperature profiles, and the effect of this on the integral light output of metal-halide lamps as a function of gravity *Master's thesis* Eindhoven University of Technology
- [21] Kroesen G M W, Haverlag M, Dekkers E, Moerel J, de Kluijver R, Brinkgreve P, Groothuis C H J M, Van der Mullen J J A M, Stoffels W W, Keijser R, Bax M, Van den Akker D, Schiffeleers G, Kemps P C M, Van den Hout F H J, Kuipers A 2005 *Microgravity sci. technol.* XVI-1
- [22] Stoffels W W, Haverlag M, Kemps P C M, Beckers J and Kroesen G M W 2005 *Appl. Phys. Lett.* **87** 1
- [23] Atomic Line Data (Kurucz R L and Bell B) Kurucz 1993 CD-ROM No. 23. Cambridge, Mass.: Smithsonian Astrophysical Observatory
- [24] Wickliffe M W and Lawler J E 2000 *J. Quant. Spectrosc. Radiat. Transfer* **66**, 363
- [25] http://www.thespectroscopynet.com/Theory/Partition_Functions.asp
- [26] Van der Heijden H W P, Van der Mullen J J A M 2002 *J. Phys. D* **35**, 2112
- [27] Johnston C W, Van der Heijden H W P, Van der Mullen J J A M 2002 *J. Phys. D* **35**, 342
- [28] Bellows A H, Feuersanger A E, Rogoff G L, and Rothwell H L, 'HID convection studies: a space shuttle experiment,' 1984 Illuminating Engineering Soc. Meeting
- [29] Bellows A H, Feuersanger A E, Rogoff G L, and Rothwell H L, 'Convection and Additive segregation in High pressure lamp arcs: Early results from a space shuttle experiment,' 1984 Gaseous electronics Conf., 1985 *Bull. Amer. Phys. Soc.* Vol **30**, p 141
- [30] Elenbaas W 1951 *The high pressure mercury vapour discharge*, 1st ed., (North-Holland publishing company)
- [31] Fischer E 1978 *Influences of External and Self-Magnetic Fields on the behaviour of discharge lamps*, Philips GmbH Forschungslaboratorium Aachen Lobornotiz nr 13/78.
- [32] Curry J J, Sakai M and Lawler J E 1998 *J. Appl. Phys.* **84**, 3066
- [33] Benck E C, Lawler J E and Dakin J T 1989 *J. Opt. Soc. Am. B* **6**, 11
- [34] Stoffels W W, Kroesen G M W, Groothuis C H J Mv, Flikweert A J, Nimalasuriya T, Van Kemenade M, Kemps P C M, Bax M, Van den Hout F H J, Van den Akker D, Schiffelers G, Beckers J, Dekkers E, Moerel J, Brinkgreve P, Haverlag M, Keijser R and Kuipers A 2005 *Proceedings of the XXVIIth International Conference on Phenomena in Ionised Gases Eindhoven (16-342)*, july 17-22, 2005, E.M. Van Veldhuizen, Eindhoven University of Technology.
- [35] Beks M L, Van der Mullen J J A M, to be submitted
- [36] Hirschfelder J O, Curtiss C F and Bird R B 1966, *Molecular Theory of Gases and Liquids*, 3rd edition, (John Wiley and Sons Inc.)
- [37] Chapman S and Cowling T G 1970 *The Mathematical Theory of Non-uniform Gases*, Cambridge University press third edition
- [38] Rockwood S D 1973, *Phys. Rev. A.*, **8** 2348
- [39] Chen C L Raether M 1962 *Phys. Rev.* **128** 2679

- [40] de Groot J, Van Vliet J 1986, *the high pressure sodium lamp*, Philips technical library, kluwer technische boeken, Deventer, Antwerpen

X-Ray induced fluorescence measurement of segregation in a DyI₃-Hg metal-halide lamp.

Abstract. Segregation of elemental Dy in a DyI₃-Hg metal-halide high-intensity discharge lamp has been observed with x-ray induced fluorescence. Significant radial and axial of Dy segregation are seen, with the axial segregation characterized by a Fischer parameter value of $\lambda = 0.215 \pm 0.002 \text{ mm}^{-1}$. This is within 7% of the value ($\lambda = 0.20 \pm 0.01 \text{ mm}^{-1}$) obtained by Flikweert *et al* (J. Appl. Phys. **98** 073301 (2005)) based on laser absorption by neutral Dy atoms. Elemental I is seen to exhibit considerably less axial and radial segregation. Some aspects of the observed radial segregation are compatible with a simplified fluid picture describing two main transition regions in the radial coordinate. The first transition occurs in the region where DyI₃ molecules are in equilibrium with neutral Dy atoms. The second transition occurs where neutral Dy atoms are in equilibrium with ionized Dy. These measurements are part of a larger study on segregation in metal-halide lamps under a variety of conditions.

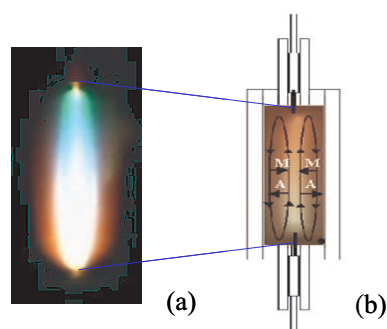


Figure 6.1: (a) Colour separation in a metal-halide lamp burner caused by axial segregation. (b) Schematic view of a metal-halide lamp; diffusion and convection of atoms (A) and molecules (M) are indicated by arrows. See figure 1.1 for full colour.

6.1 Introduction

Metal-halide lamps are compact, high-intensity light sources with high luminous efficacy and good colour rendering [1]. They consist of an electric discharge through a high-pressure Hg vapour containing a relatively small amount of additives consisting of metal-halide salts. Two or more salts are typically used to maximize the colour rendering index. Mixtures such as $(\text{NaI} + \text{ScI}_3)$, $(\text{NaI} + \text{TlI} + \text{InI})$ or $(\text{NaI} + \text{TlI} + \text{DyI}_3 + \text{HoI}_3 + \text{TmI}_3)$ are common in commercial lamps. Although the additives are present in densities much smaller than that of Hg, they dominate the ionization and power balances of the discharge because they have excitation and ionization potentials much lower than those of Hg. At operating temperatures, metal-halide molecules diffuse into the Hg vapour where they are dissociated to varying degrees depending on the local temperature. In the core of the arc, where temperatures are highest, the additive metal-halides are completely dissociated and even partially ionized. Excitation of additive metal atoms and ions in the core of the discharge is the primary source of visible radiation from these lamps.

The spatially inhomogeneous distribution of atomic and molecular species in metal-halide arcs can combine with complex transport mechanisms to produce an effect called segregation, or de-mixing [2]. Segregation refers to a non-uniform distribution of additives relative to the Hg buffer gas. It can lead to deficiencies in colour uniformity (see figure 6.1) and a reduction in luminous efficacy. In order to gain a better understanding of the segregation phenomena, we have used x-ray induced fluorescence [3,4] to measure the spatial distributions of both the additives and the Hg in a test lamp specifically designed to enhance segregation.

The lamp type in question has been studied previously by Nimalasuriya *et al* [5] using optical techniques, yielding density distributions of atomic and ionic species of the additives and Hg. This technique, however, does not provide molecular densities and requires extensive data analysis. The lamp was also studied using laser absorption [6], which yields only the density of Dy in its ground state. In the present study, x-ray induced fluorescence

was used to directly measure elemental densities. Elemental density includes the contribution of the ions, atoms and molecules. X-ray induced fluorescence consists of irradiation of an atom using photons with energy sufficient to eject an inner shell electron. X-ray fluorescence, with energy characteristic of the atomic number of the atom, is emitted when an outer shell electron fills the inner shell vacancy created by the incident photon. This technique allows for a direct measurement of elemental density independent of the state of the atom such as excitation, ionisation or molecular bonding.

Previous x-ray induced fluorescence measurements of a metal halide lamp were made by Curry *et al* [3] on a ceramic metal halide lamp of a different burner geometry and filling. The lamp type used in the present study was previously observed under both reduced and enhanced gravity [7, 8, 10, 11] and studied by x-ray absorption techniques [12]. The lamp was filled with a Hg buffer gas and one salt, namely DyI₃. The simplicity of this salt system makes it easier to compare measurements with results of a numerical model.

6.2 Theory

Only a small fraction of the DyI₃ salt evaporates and enters the discharge, leaving a liquid salt pool at the coldest spot of the burner wall. The temperature of the liquid salt pool determines the vapour pressure of the additive in the vicinity of the cold spot. The temperature of the arc, which varies from more than 6000 K in the core to less than 1200 K near the wall [12], leads to varying degrees of dissociation, and even ionization, of the evaporated additive. Here we signify species produced by varying states of dissociation and ionization by a subscript i and the number density of a particular species by n_i . Elements are signified by a subscript in braces $\{\alpha\}$. The number density of a particular element, $n_{\{\alpha\}}$, is the sum over all species containing that element

$$n_{\{\alpha\}}(r, z) = \sum_i R_{i\{\alpha\}} n_i(r, z). \quad (6.1)$$

where R is the stoichiometric coefficient.

The distributions of elemental densities are influenced by three principal factors. First, the gas temperature affects densities through partial pressures

$$p_{\{\alpha\}} = n_{\{\alpha\}}(r, z)kT(r, z) = \sum_i R_{i\{\alpha\}} n_i(r, z)kT(r, z). \quad (6.2)$$

where k is Boltzmann's constant and $T(r, z)$ is the heavy particle temperature. It is assumed that the latter is identical to the chemical equilibrium temperature. It may also coincide with the electron gas temperature, the atomic/molecular excitation temperature, or radiation temperature in certain regions of the discharge. The spatial distribution of $T(r, z)$, which peaks on the arc axis, produces a heavy particle distribution which has a minimum on the axis.

Second, the distributions of elemental densities are influenced by radial segregation. This effect is produced by the different radial diffusion velocities of different atomic and

molecular species. Ambipolar diffusion [13], in particular, causes ions to diffuse out of the core faster than neutral atoms or molecules diffuse inward. A steady-state can only be achieved when the elemental density of Dy is lower in the core than it would be in the absence of the difference in diffusion velocities [3].

Third, the distributions of elemental densities are influenced by axial segregation, an effect produced by a combination of radial diffusion and gravity-driven axial convection. It usually leads to an accumulation of radiating additives near the bottom of the arc, sometimes with a significant impact on the colour uniformity (figure 6.1). Fischer characterised axial segregation with a parameter λ such that [2]:

$$p_{\{\alpha\}}(z) = p_{\{\alpha\}}(0) \exp(-\lambda_{\{\alpha\}}z), \quad (6.3)$$

where z is the axial position relative to the tip of the lower electrode. $\lambda_{\{\alpha\}}$ is called the segregation parameter for the element α . Since densities, and not partial pressures, are measured experimentally, it is useful to reformulate equation 6.3 in terms of the mixing ratio, $n_{\{\alpha\}}/n_{\{Hg\}}$. Dividing equation 6.3 by the total lamp pressure $p_0 \approx n_{\{Hg\}}(r, z)kT(r, z)$, which is not a function of position, gives

$$\frac{n_{\{\alpha\}}(z)}{n_{\{Hg\}}(z)} = \frac{n_{\{\alpha\}}(0)}{n_{\{Hg\}}(0)} \exp(-\lambda_{\{\alpha\}}z). \quad (6.4)$$

Here, the r -dependence has been suppressed because the Fischer model is one-dimensional. In a well-mixed system, $\lambda_{\{\alpha\}} = 0$ for all additives, i.e. the mixing ratios do not depend on z , even if $n_{\{\alpha\}}$ and $n_{\{Hg\}}$ do. Spatial variations in the mixing ratios signify segregation.

Three principal regions can be identified within the radial density distribution of elemental Dy (see figure 6.2). These are 1) the region near the wall where DyI_3 molecules are predominant, 2) the mantle region between the wall and the arc core where Dy atoms predominate, and 3) the core where the Dy is almost completely ionized in the form of Dy^+ . The molecules DyI_2 and DyI are relatively unstable and do not have a dominant presence in any region of the discharge [15].

It is interesting to examine the balance of radial fluxes of the additive elements and the resulting behaviour of elemental density distributions at the two transitions between these regions. Following Hartgers *et al* [14], the radial flux $\Gamma_{\{\alpha\}}$ of element α can be written

$$\Gamma_{\{\alpha\}} = \sum_i R_{i\{\alpha\}} \left[-\frac{D_i}{kT} \frac{\partial p_i}{\partial r} + \frac{p_i}{kT} u_r + \frac{D_i}{kT} \frac{q_i}{q_e} \frac{p_i}{p_e} \frac{\partial p_e}{\partial r} \right]. \quad (6.5)$$

The summation in equation 6.5 is over each species i containing element α and e refers to the electron population. The diffusion coefficient, D_i , characterizes diffusion of species i through the Hg vapour; elastic collisions with other species are ignored because of the low density of other species compared to Hg. u_r is the radial convective flow and q designates charge. The first term on the right hand side of equation 6.5 represents the diffusion of species due to partial pressure gradients. The second term on the right hand side represents the flux arising from convective flow. Although, as mentioned earlier, axial convective flow can give rise to segregation, in analyzing radial segregation we will ignore the radial

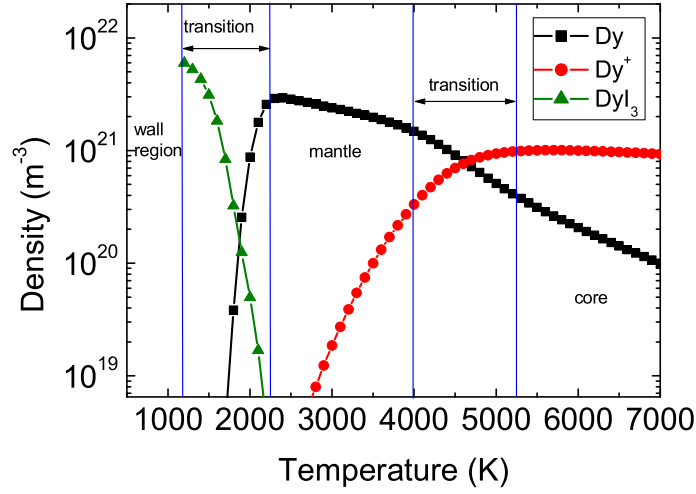


Figure 6.2: Theoretical density distribution of Dy atoms, ions and molecules as a function of temperature at the midplane of a metal-halide lamp containing $2 \cdot 10^6$ Pa (20 atm) of Hg. For clarity, DyI_2 and DyI have been omitted. (*courtesy to M L Beks*)

convective flow, u_r . Finally, the third term on the right hand side describes ambipolar diffusion of the charged species and arises from the relatively rapid movement of electrons outward from the core and the subsequent charging of the core, which in turn, produces the ambipolar electric field. Hereafter we will assume that for the relevant regions the different forms of radial transport must balance so that in these transition regions the net flux of each element vanishes i.e.,

$$\Gamma_{\{\alpha\}} = 0. \quad (6.6)$$

The transition region between the wall and mantle is characterized by the reaction



The tri-iodide molecule is stable in the region closest to the wall and diffuses inward as a result of a positive partial pressure gradient, while the atomic species are stable in the mantle region and diffuse outward due to a negative partial pressure gradient. Ions and electrons have negligible densities at this transition. Therefore ambipolar diffusion is not significant here. Equation 6.5 gives for Dy

$$\Gamma_{\{\text{Dy}\}} = - \left(\frac{D_{\text{DyI}_3}}{kT} \right) \frac{\partial p_{\text{DyI}_3}}{\partial r} - \left(\frac{D_{\text{Dy}}}{kT} \right) \frac{\partial p_{\text{Dy}}}{\partial r} = 0. \quad (6.8)$$

Assuming the ratio of diffusion coefficients is constant, equation 6.8 can be integrated over the transition region to yield

$$p_{Dy}|_h = \left(\frac{D_{DyI_3}}{D_{Dy}} \right) p_{DyI_3}|_c \quad (6.9)$$

where c and h refer to the hot and cold side of the transition region. Using $n_{Dy}|_h \approx n_{\{Dy\}}|_h$ and $n_{DyI_3}|_c \approx n_{\{Dy\}}|_c$, and employing $p_i = n_i kT$ this can be rewritten as

$$\frac{n_{\{Dy\}}|_h}{n_{\{Dy\}}|_c} \approx \left(\frac{D_{DyI_3}}{D_{Dy}} \right) \frac{T_c}{T_h}. \quad (6.10)$$

Equation 6.10 suggests that the density of elemental Dy will change across this transition region by the factor, $\left(\frac{D_{Dy}}{D_{DyI_3}} \right) \approx 3$. That is, radial segregation of a factor of three is expected just inside the discharge wall, simply because the tri-iodide molecule diffuses more slowly than the Dy atom. The same argument holds for the other rare-earth tri-iodides commonly used in metal-halide lamps.

The same analysis for I across this transition does not suggest radial segregation because, although the tri-iodide molecule diffuses approximately three times more slowly than the I atoms, the molecule carries three times as many I atoms.

The second transition region, between the mantle and the core, is characterized by the reaction



Here, Dy atoms are stable in the outer, cooler region and diffuse inward as the result of a positive partial pressure gradient, while Dy ions are stable in the core and diffuse outward as the result of a negative partial pressure gradient. In addition, Dy ions are subject to the ambipolar field, which enhances their diffusion out of the core. The balance of fluxes at this transition is

$$\left(\frac{D_{Dy}}{kT} \right) \frac{\partial p_{Dy}}{\partial r} + \left(\frac{D_{Dy^+}}{kT} \right) \frac{\partial p_{Dy^+}}{\partial r} + \left(\frac{D_{Dy^+}}{kT} \right) \frac{p_{Dy^+}}{p_e} \frac{\partial p_e}{\partial r} = 0. \quad (6.12)$$

In the lamp used for the present study, where segregation is severe and the density of Dy in the core is not sufficient to lower the core temperature significantly from what is seen in a pure Hg discharge [5,7], the electron density can be replaced in the preceding equation by the Hg ion density, i.e., $p_e \approx p_{Hg^+}$. Rewriting equation 6.12 in terms of elemental densities yields

$$D_{Dy} n_{\{Hg\}} \frac{\partial}{\partial r} \left(\frac{n_{Dy}}{n_{\{Hg\}}} \right) + D_{Dy^+} n_{\{Hg\}} \frac{\partial}{\partial r} \left(\frac{n_{Dy^+}}{n_{\{Hg\}}} \right) = -D_{Dy^+} n_{\{Hg\}} \frac{n_{Dy^+}}{n_{Hg^+}} \frac{\partial}{\partial r} \left(\frac{n_{Hg^+}}{n_{\{Hg\}}} \right). \quad (6.13)$$

Assuming $D_{Dy} \approx D_{Dy^+}$ and $n_{Dy} + n_{Dy^+} = n_{\{Dy\}}$ in this region, the two terms on the left hand side of equation 6.13 can be combined,

$$[D_{Dy} n_{\{Hg\}}] \frac{\partial}{\partial r} \left(\frac{n_{\{Dy\}}}{n_{\{Hg\}}} \right) = - [D_{Dy} n_{\{Hg\}}] \frac{n_{Dy^+}}{n_{Hg^+}} \frac{\partial}{\partial r} \left(\frac{n_{Hg^+}}{n_{\{Hg\}}} \right). \quad (6.14)$$

The term on the left hand side represents the flux arising from partial pressure gradients, while the term on the right hand side represents the flux arising from ambipolar diffusion. Although there is no simple analytic integration of equation 6.14, the terms on each side of the equation may be evaluated using experimental data. Elemental densities have been measured in the present work with x-ray induced fluorescence, while the Hg and Dy ion densities have been measured with optical emission spectroscopy [5, 7].

6.3 The experiment

6.3.1 The Lamp

The lamp we examined was designed to maximize segregation in order to facilitate the study of this effect. Observations of this and other lamps designed for the same purpose have been reported previously [6, 6, 12], including observations under micro- and hyper-gravity conditions [7, 8]. The lamp consists of an 8 mm inner diameter quartz arc tube surrounded by a quartz outer vacuum jacket. The electrode gap is 18 mm. The lamp contains 10 mg of Hg and 3.7 mg of DyI₃ [15]. For the measurements presented here, the lamp was operated vertically at a power of 145 W. Power was supplied by an electronic square-wave ballast at a frequency of 122 Hz. The lamp voltage and current waveforms were monitored with a digital oscilloscope and lamp power was calculated from their time-averaged product. The latter was stable to better than 1%.

6.3.2 X-ray induced fluorescence

Use of x-ray induced fluorescence (XRF) to obtain spatially-resolved, absolute densities of additives in metal-halide lamps has been described by Curry *et al* [3]. This method measures elemental density, the density of a particular element summed over all atomic and molecular species. It is therefore able to directly observe mixing ratios without resorting to assumptions about partition functions. We measured the elemental densities of fluorescence at the Sector 1 Insertion Device beam line at the Advanced Photon Source, Argonne National Laboratory [16]. A beam of monochromatic, high-energy photons (70 keV or 86 keV) was used to excite fluorescence in the arc constituents. The incoming photon flux was measured by a nitrogen-filled ionization chamber and the fluorescence photons were detected with an energy-resolving Ge detector situated to observe photons emitted in a direction perpendicular to the incident beam. The energy response of the detector is flat from approximately 20 keV to approximately 80 keV, falling off by only about 15% between 80 keV and 100 keV.

Spatial resolution was obtained by using a small beam cross section (0.5 mm wide by 1.0 mm high) and restricting the field of view of the detector to a small length of the incident beam (figure 6.3) using a 500 μm diameter pinhole aperture and the 11.3 mm diameter aperture of the detector. Absolute calibration of densities was obtained by comparing fluorescence intensities from Dy, I, and Hg in the lamp described above with fluorescence

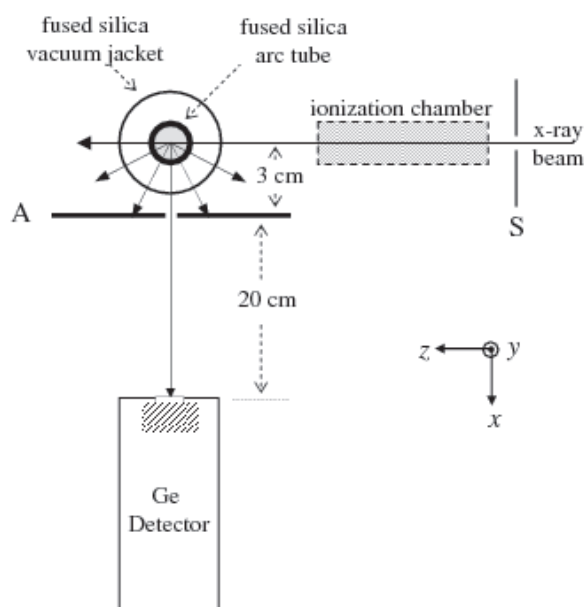


Figure 6.3: Experimental setup for x-ray induced fluorescence in a metal-halide lamp. The x-ray beam is extracted from the Sector 1 Insertion Device beam line at the Advanced Photon Source.

intensity from a cell containing a known density of Xe atoms.

The density of Hg was obtained using an incident photon energy of 86 keV. The small cross-sections for excitation of Dy and I at this energy and the much stronger signal from Hg made it difficult to measure the much lower densities of the additives with good signal-to-noise. The densities of Dy and I were observed, instead, with an incident photon energy of 70 keV, where the cross-sections of the additives are larger and Hg fluorescence is not excited. The two sets of data were acquired on slightly different radial spatial grids, so mixing ratios are computed using Hg densities obtained from radial polynomial fits to the Hg data.

The densities of the additives were corrected for absorption of fluorescence by Hg atoms. This correction is most significant for I because of its lower energy fluorescence, but never exceeds 12%. For Dy, it never exceeds 4%.

A spectrum taken near the bottom electrode at a beam energy of 70 keV is shown in figure 6.4; it clearly shows Dy and I peaks. Ce fluorescence peaks are also seen. Ce is present in the lamp vacuum jacket and multiple photon scattering events allow it to be seen by the detector.

6.4 Results and Discussion

Elemental densities for Hg, Dy, and I are shown in Figures 6.5, 6.6, and 6.7. The error bars in these figures indicate typical random uncertainties. For both Hg and I, relative

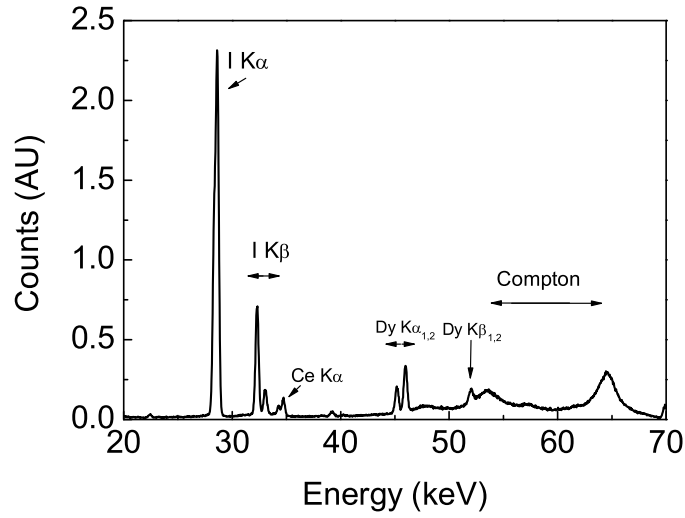


Figure 6.4: X-ray induced fluorescence spectrum excited by 70 keV photons at $x/R = 0.3$, where x is the displacement from the arc axis in the direction of the detector and $R = 0.004$ m is the radius. The horizontal arrow indicates the spectral range of broad peaks due to Compton scattering by the arc tube and vacuum jacket. Counts are given in arbitrary units.

random uncertainties are less than 1% and the error bars are too small to be seen clearly on the scale of the figures. The random component of uncertainty in the present case is due entirely to the precision with which a baseline can be determined for the fluorescence peaks and is influenced by both random detector noise and by any interfering spectral feature. Although the latter might be more properly considered a systematic uncertainty, at least for a given data point, it is much more natural to assign to the same category as detector noise.

Systematic uncertainties in x-ray fluorescence measurements of this kind are discussed in [4]. In dealing with plasma systems, it is rarely worth the effort to make absolute measurements with uncertainties of less than 5% because plasmas are seldom reproducible at a higher level. For the present discussion, we emphasize the density of elemental components relative to each other, a process that eliminates many of the possible systematic errors. The ratio of Dy to I at a given location, for example, is derived from a single spectrum in which all features are acquired simultaneously.

Comparison of Xe calibration spectra and of I fluorescence intensities acquired at the two different excitation energies indicates that the efficiency of our fluorescence collection system changed at some point during data acquisition at high energy, most likely as a result of the detector being bumped. Normally, a small movement of the detector is not important because it is under-filled. In this case, however, it was a limiting aperture. Any movement of the detector must have occurred between data runs, because the experimental chamber is

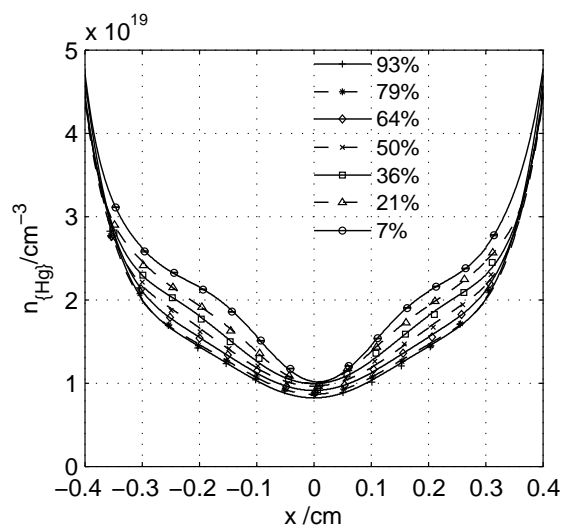


Figure 6.5: Radial profiles of elemental Hg at different axial positions. The axial positions are given as a percentage of the total length of the arc relative to the lower electrode.

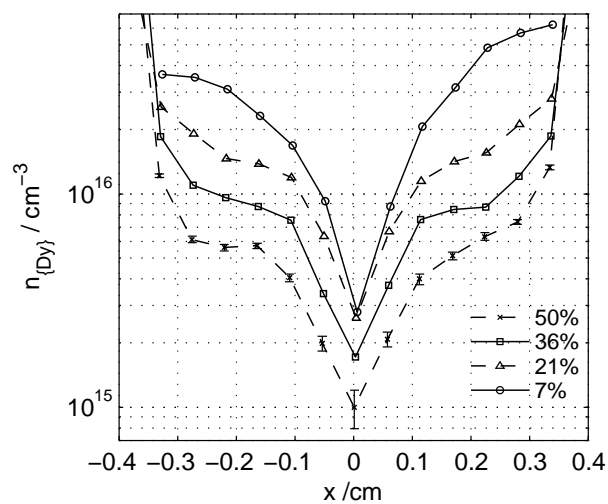


Figure 6.6: Radial profiles of elemental Dy at different axial positions. The axial positions are given as a percentage of the total length of the arc relative to the lower electrode.

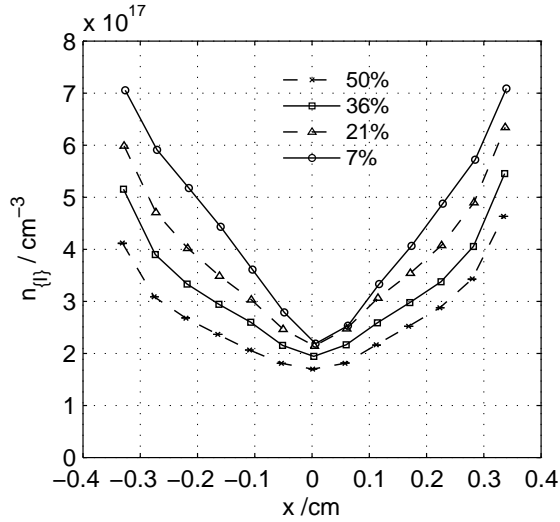


Figure 6.7: Radial profiles of elemental I at different axial positions. The axial positions are given as a percentage of the total length of the arc relative to the lower electrode.

inaccessible during data acquisition. Therefore, spatial distributions and relative intensities are not affected. In addition, we have scaled the measurements at high energy to match those at low energy using the iodine fluorescence, which was adequately strong in both cases. This gives an estimated systematic uncertainty of $\pm 20\%$.

The measured Hg densities in figure 6.5 have been fit to radial polynomials. The fitted radial profiles are extended to the discharge wall by using wall densities obtained by combining pyrometrically-measured wall temperatures from Zhu, T_{wall} , [12] and an estimated lamp pressure of $p_0 = 8 \times 10^5$ Pa (8 atmospheres) to obtain $n_{\{Hg\}}(wall) = p_0/kT_{wall}$. The Hg density shows a clear constriction of the arc core (high temperature region) in the vicinity of the lower electrode and a steady decrease in density as one moves upward, indicative of increasing temperature with increasing height. The primary cause of the constricted core at the bottom of the arc is the presence of Dy atoms and ions. The broad optical emission spectra of Dy atoms and ions efficiently radiate power, thereby cooling the arc core and causing the arc to constrict [17]. On the other hand, axial segregation has considerably reduced the Dy density at points higher in the arc, as will be seen in figure 6.6. Constriction near the lower electrode was also observed in this lamp design using optical emission [5, 7].

Zhu [12] measured the Hg density in a nominally identical lamp under similar conditions using x-ray absorption imaging. She did not publish the Hg density data, but instead published temperature profiles, T_{Zhu} , derived from that data. Using her reported lamp pressure of $p_0 = 10 \times 10^5$ Pa (10 atmospheres), we compare p_0/kT_{Zhu} with our own measured Hg densities in Figures 6.8 and 6.9. Radial distributions near both the upper and the lower electrode are shown. Our measurements are generally about 40% lower than that implied by Zhu. The narrow core is also better resolved by x-ray induced fluorescence than by x-ray

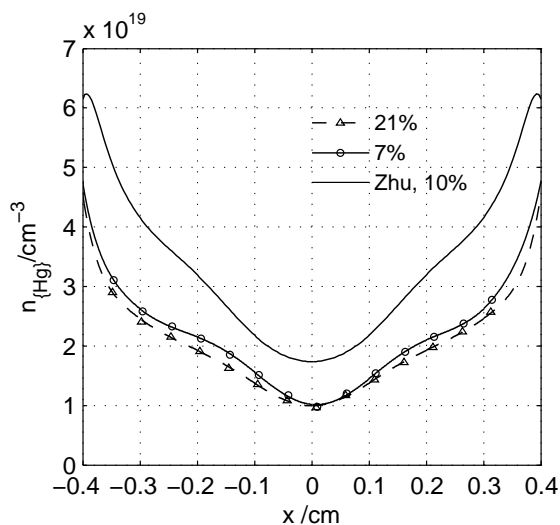


Figure 6.8: Comparison of elemental Hg densities with measurements made by Zhu [12] using x-ray absorption imaging. Axial positions are given as a percentage of the total length of the arc relative to the lower electrode.

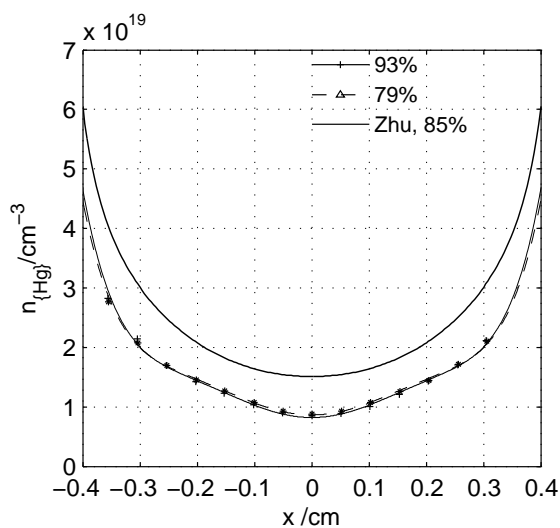


Figure 6.9: Comparison between Hg densities measured with x-ray induced fluorescence and densities measured with x-ray absorption imaging by Zhu [12]. Axial positions are given as a percentage of the total length of the arc relative to the lower electrode.

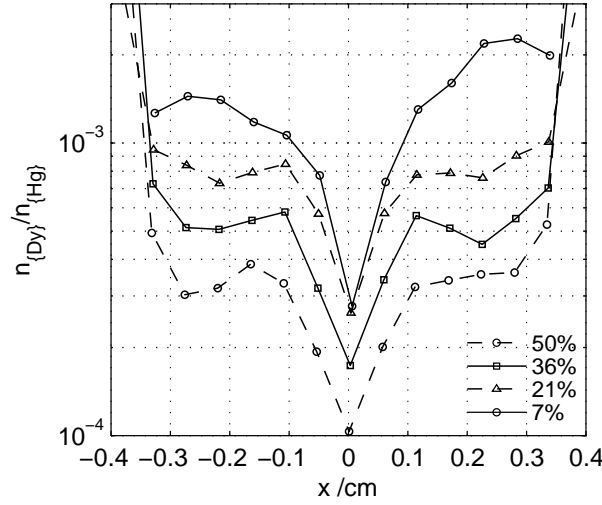


Figure 6.10: The mixing ratio $n_{\{Dy\}}/n_{\{Hg\}}$, with the axial positions given as a percentage of the total length of the arc relative to the lower electrode.

absorption imaging. Although x-ray absorption imaging, in principle, has better spatial resolution, it can be limited in practice by the need to reduce measurement noise that would be unacceptably amplified by the Abel inversion.

The measured elemental Dy densities (see figure 6.6) are of the same order of magnitude as seen in laser absorption measurements of the neutral atomic ground state densities obtained by Flikweert *et al* [6] in a nominally identical lamp, in the region where neutral atomic Dy is the dominant Dy species.

The measured elemental I densities (see figure 6.7) are on the order of 100 times larger than the Dy densities. Two causes are suggested for this large factor. First, the segregation of Dy is extremely large because the experimental lamp was designed to maximize this effect. Second, both x-ray fluorescence measurements with the lamp off and a post-experiment chemical analysis confirm the formation of Dy-silicates on the arc tube. The permanent removal of Dy from the discharge leaves an excess of free I.

The Dy mixing ratio as a function of both radial and axial position is shown in figure 6.10. There are two distinct transition regions in the radial profiles, corresponding to the transition regions discussed in Section 6.2. Near the wall, the mixing ratio drops precipitously for three of the four profiles. This corresponds to the transition from DyI_3 molecules near the wall to Dy atoms in the mantle. The simple theoretical model discussed in Section 6.2 suggested a factor of three drop in the mixing ratio across this transition. Three of the four profiles show a much larger drop, while the lowest profile shows a smaller drop. At least some of the larger drop for the upper profiles in the Dy mixing ratio is attributable to the permanent accumulation of Dy on the wall in the form of Dy-silicates. In other words, measurements made at the wall contained some contribution from the much higher density of Dy attached to the wall. Visual inspection indicated that accumulation

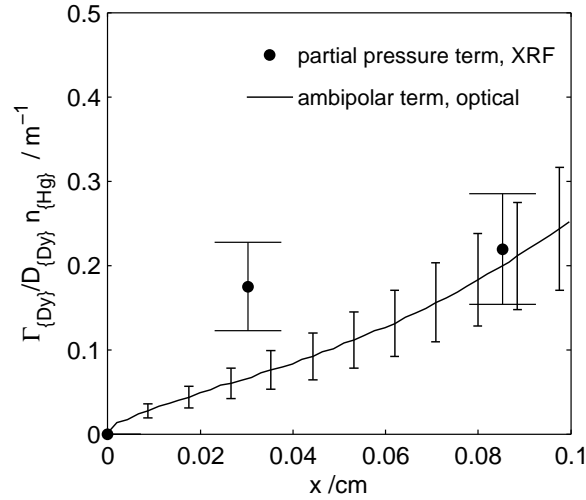


Figure 6.11: The radial gradients giving rise to the Dy elemental flux density (see equation 6.14) in the core of the arc at the midplane are evaluated. The partial pressure term (left hand side of equation 6.14) is evaluated with the x-ray induced fluorescence measurements presented here, while the ambipolar term (right hand side of equation 6.14) is evaluated with data from optical emission measurements [5, 7].

of Dy silicates on the wall was considerably less at the height of the lower electrode and below, presumably as a result of lower wall temperatures. For the lowest radial profile in figure 6.10, partial overlap of the x-ray beam with the wall at the largest radial values would reduce the measured Dy density, rather than increase it, as would be the case at higher axial positions. A clear distinction between the wall and the transition region where Dy molecules are dissociated requires a finer spatial resolution than we used.

The second distinct transition region occurs at the edge of the core. The Dy mixing ratio decreases by a factor of 3 or more over this transition. Here we used our measured Dy mixing ratio to evaluate the gradient in the partial pressure flux density term on the left-hand side of equation 6.14. We also used published measurements of n_{Hg^+} and n_{Dy^+} densities from optical emission observations [5, 7] to evaluate the gradient in the ambipolar flux density term on the right hand side of equation 6.14. These latter measurements were acquired in a lamp of the same design as the one used here, although at a lower power of 100 W. This difference in operating power could significantly affect the cold spot temperature and therefore the amount of Dy in the arc. The results are shown in figure 6.11 for the core region ($r \leq 1$ mm, where equation 6.14 is expected to be valid) in the midplane of the arc. In this limited range of r , there are only two data points from the x-ray induced fluorescence measurements. Considering the different operating powers under which the two data sets were obtained, the agreement between the two flux terms is surprisingly good. The comparison near $r = 0.8$ mm shows excellent agreement between the partial pressure gradient flux term and the ambipolar flux term, while the comparison near $r = 0.3$ mm shows the partial pressure flux term to be approximately twice as large as the ambipolar

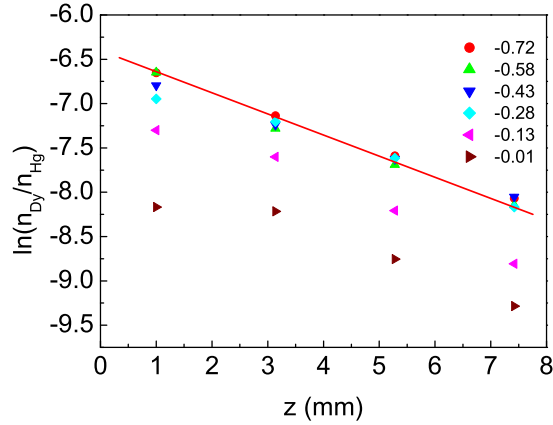


Figure 6.12: Natural logarithm of the Dy mixing ratio versus axial position, z , for several radial positions. The tip of the lower electrode is located at $z = 0$ mm. The radial positions are given as a fraction of the full radius of the arc tube. The straight line is a fit to data at a normalized radius $x/R = 0.72$.

term. A more thorough study of the radial fluxes in the core of metal-halide lamps would be interesting.

Substantial axial segregation of Dy is also apparent in figure 6.10. The Dy mixing ratio is at least a factor of three lower at the midplane of the lamp than at the bottom. The Fischer segregation parameter characterizing axial segregation was determined by least squares fit (see figure 6.12). A weighted average over all radial positions gives $\lambda_{\{Dy\}} = 0.215 \pm 0.002 \text{ mm}^{-1}$. This result is 7% larger than the $\lambda_{\{Dy\}} = 0.20 \pm 0.01 \text{ mm}^{-1}$ found by Flikweert *et al* [6] using laser-absorption.

Radial segregation of I is practically non-existent. As discussed in Section 6.2, theory suggests there should not be a rapid change in the I mixing ratio across the transition region where DyI_3 is dissociated. In addition, I has an ionization energy slightly higher than Hg and much higher than Dy. The fractional ionization of I is very low, even in the core of the arc. Therefore, the ambipolar term for Dy that leads to equation 6.14 is negligible for I. The simplified theoretical picture of Section 6.2 does not suggest any radial segregation for I.

The absence of significant radial segregation for I, in turn, limits axial segregation of I. The Fischer axial segregation parameter for I, a weighted average over all radial positions, was found to be $\lambda_{\{I\}} = 0.056 \pm 0.001 \text{ mm}^{-1}$. This is a factor of 4 less than for the axial segregation parameter for Dy.

6.5 Conclusions

Absolute elemental densities of Dy and Hg have been obtained in a metal-halide lamp as a function of radial and axial location using x-ray induced fluorescence. The mixing ratio $n_{\{Dy\}}/n_{\{Hg\}}$ shows significant axial and radial segregation of Dy. The Fischer segregation parameter for Dy, averaged over radial position, is determined to be $\lambda_{\{Dy\}} = 0.215 \pm 0.002 \text{ mm}^{-1}$. Both Dy density and Fischer parameter are in agreement with laser absorption measurements done by Flikweert *et al* [6] where neutral atomic Dy densities were measured. An excess of I in the gas phase is created as Dy reacts with the burner wall and forms Dy silicates. I shows less radial and axial segregation than Dy, in agreement with theory. The axial segregation parameter for I, averaged over radial position, is $\lambda_{\{I\}} = 0.056 \pm 0.001 \text{ mm}^{-1}$. This is 4 times less than for Dy.

A simplified theoretical description of radial fluxes is partially successful in describing the measured mixing ratios and earlier observations of optical emission.

6.6 Acknowledgements

Use of the Advanced Photon Source was supported by the U. S. Department of Energy, Office of Science, Office of Basic Energy Sciences, under Contract No. DE-AC02-06CH11357. The authors thank M.L. Beks and A. Hartgers for theoretical discussions. T.N. acknowledges support from Technologiestichting STW (project ETF. 6093).

Bibliography

- [1] Lister G G, Lawler J E, Lapatovich W P and Godyak V A 2004 *Rev. Mod. Phys.* **76**, 541
- [2] Fischer E 1976 *J. Appl. Phys.* **47**, 2954
- [3] Curry J J, Adler H G, Shastri S D, Lee W -K 2003 *J. Appl. Phys.* **93**, 2359
- [4] Curry J J, Adler H G, Shastri S D, J.E. Lawler 2001 *Appl. Phys. Lett.* **79**, 1974
- [5] Nimalasuriya T, Pupat N B M, Flikweert A J, Stoffels W W, Haverlag M and Van der Mullen J J A M 2006 *J. Appl. Phys.* **99** 053302 **see chapter 2**
- [6] Flikweert A J, Nimalasuriya T, Groothuis C H J M, Kroesen G M W and Stoffels W W 2005, *J. Appl. Phys.* **98** 073301
- [7] Nimalasuriya T, Flikweert A J, Haverlag M, Van der Mullen J J A M, Kemps P C M, Kroesen G M W, Stoffels W W, Van der Mullen J J A M 2006 *J. Phys D: Appl Phys* **39** 2993 **see chapter 3**
- [8] Flikweert A J, Van Kemenade M, Nimalasuriya T, Haverlag M, Kroesen G M W and Stoffels W W 2006 *J.Phys.D* **39**, 1599
- [9] Nimalasuriya T, Thubé G M, Flikweert A J, Haverlag M, Kroesen G M W, Stoffels W W, Van der Mullen 2007, *J.Phys.D* 2007 **40** 2839, **see chapter 4**
- [10] Kroesen G M W, Haverlag M, Dekkers E, Moerel J, de Kluijver R, Brinkgreve P, Groothuis C H J M, Van der Mullen J J A M, Stoffels W W, Keijser R, Bax M, Van den Akker D, Schiffeleers G, Kemps P C M, Van den Hout F H J, Kuipers A 2005 *Microgravity sci. technol.* XVI-1
- [11] Stoffels W W, Haverlag M, Kemps P C M, Beckers J and Kroesen G M W 2005 *Appl. Phys. Lett.* **87** 1
- [12] Zhu X 2005 Ph.D. thesis, Eindhoven University of Technology
- [13] Raizer Y P, 1991 *Gas Discharge Physics*, 1st ed., (Springer verlag).
- [14] Hartgers A, Van der Heijden H W P, Beks M L, Van Dijk J, Van der Mullen J J A M 2005 *J. Phys D: Appl Phys*, **38** 3422-29, equation (36)
- [15] Stoffels W W, Flikweert A J, Nimalasuriya T, Van der Mullen J J A M, Kroesen G M W, Haverlag M, 2006 *Pure Appl. Chem.* **78** No 6
- [16] <http://www.aps.anl.gov/>
- [17] Elenbaas W 1951 *The high pressure mercury vapour discharge*, 1st ed., (North-Holland publishing company)

Chapter 6.

- [18] Kenty C 1938 J. Appl. Phys. **9**
- [19] Van der Mullen J J A M 1990 Phys. Rep. **191** 109
- [20] <http://www.csrrri.iit.edu/>

X-ray absorption of the mercury distribution in metal-halide lamps

Abstract. Spatial temperature profiles of metal-halide lamps have been acquired using x-ray absorption of the Hg density distribution. The temperature profiles were determined by combining the measured absorption of the spatially resolved Hg density with the wall temperature. The data analysis of x-ray absorption is extensive. After the necessary image reconstruction, the line integrated density profile needs to be Abel inverted. The solution from the Abel inversion is stabilized with the Tikhonov regularization parameter. The previous method for x-ray absorption developed in our group has been modified and improved by utilising the following 1) a larger outer bulb, 2) the corrections for x-ray scattering on the lamp materials, 3) an optimum value of Tikhonov regularisation parameter μ , 4) employing a higher degree of polynomials used for the Abel inversion. For a similar lamp as reported previously by X. Zhu [1] we found an axis temperature that is 6200 K instead of 5200. The higher temperature is similar to what is found using optical spectroscopic methods. Typical results from a metal-halide lamp with and without salts are shown.



Figure 7.1: Colour separation in a metal-halide lamp burner. The lamp is burned vertically upright. See figure 1.1 for full colour.

7.1 Introduction

The metal-halide lamp [2] originated from the need to improve the colour properties and efficiency of the high pressure Hg lamp by adding other metals to the discharge. The metals improve spectral balance and therewith the colour properties and aid luminous efficacy. These metals are added in the form of metal-halide salts, in order to protect the burner wall and to increase the vapour pressure [3]. The metal-halide lamp contains a buffer gas of Hg and a relatively small amount of a mixture of metal-halide additives such as DyI_3 , CeI_3 and/or NaI salts, which supply the prime radiators. At least two salt components are necessary for a good colour rendering index, therefore mixtures such as (NaI + ScI_3), (NaI + TII + InI) or (NaI + TII + DyI_3 + HoI_3 + TmI_3) are commonly used in metal-halide lamps. Due to the competition between diffusive and convective processes these additives are non-uniformly distributed over the lamp, which in a vertical burning position results in a undesirable segregation of colours [4], see figure 7.1.

For a proper understanding of the relation between the plasma transport phenomena and the energy coupling of high intensity discharge (HID) lamps we need insight in the temperature distribution over the plasma. Therefore x-ray absorption was used to measure the distribution of Hg atoms. This is done by irradiating the lamp with x-rays and by detecting the absorption of the x-ray photons in the whole lamp-burner. A temperature profile at different axial positions of the discharge can then be obtained by applying the ideal gas law combined with the wall temperature.

The application of x-ray absorption spectroscopy has the following advantages: Firstly, x-ray photons can penetrate all regions of the lamp. Secondly, the x-ray absorption cross-section depends only weakly on the electronic or chemical state of the atom. Thirdly, x-ray absorption measurements only depend on the absolute density of the detected element.

Other plasma parameters such as electron density, electron temperature, do not influence the absorption directly. [5]

Previous measurements were performed by Fohl *et al* [6] and Curry *et al* [5]. The temperature for the latter was calibrated using an optical technique to determine the axis temperature. Our approach is different in the sense that the obtained relative temperature field is calibrated with an absolute measurement of the wall temperature. The temperature that is acquired can therefore be considered a pure gas-temperature, obtained without the use of any optical techniques that is based on the interpretation of emission spectra. It is therefore of interest to compare the results with that of optical emission spectroscopy measurements [7], which yield the electron (excitation) temperature. This will give insight in a possible deviation from local thermal equilibrium [8].

The XRA experiment on metal-halide lamps asks for high spatial resolution, high dynamic range and a more or less monochromatic x-ray spectrum. Also data-analysis is complex as the absorption signal of Hg is relatively small compared to the absorption signal of the quartz wall material. Moreover, the lamp materials give rise to scattering of the x-rays, resulting in an offset. This offset is not constant over the lateral position. Finally the image itself needs to be processed and reconstructed.

The experiment and data-handling was designed by Zhu [1]. The temperature profiles she reported had an axis-to wall ratio of about 3.6. There is a discrepancy between this ratio and the ratio that was obtained from the temperature profile measured by means of optical emission spectroscopy on a nominally identical lamp [9]. These optical emission measurements showed an axis temperature that, combined with the wall temperature as measured by Zhu [1], led to a ratio of 4.6 [9].

The current study is an extension of the work of Zhu and is especially dedicated to the improvement of the data analysis. Phenomena such as beam-hardening and x-ray scattering on quartz have been studied and the latter incorporated. The inverse procedure used to extract radial information from the line-of-sight measurements was extended and implemented.

This chapter is organized as follows. Section 7.2 describes the image processing and fitting procedures necessary to obtain the temperature of the arc. Section 7.3 describes the lamps used in the experiments and the experimental setup. Results from the experiments are presented and discussed in section 7.4. These results include important improvements made to the data analysis and two temperature distributions for a lamp with and without salt filling (i.e. DyI₃). Finally, section 7.5 offers conclusions and future plans.

7.2 Theory

7.2.1 Image processing and reconstruction

The basic process of XRA is that due to the interaction with inner-shell electrons x-ray photons are removed from the beam. Since the density of the buffer gas Hg is much larger than that of the other species, the primary observable is the Hg density distribution n_{Hg} .

Therefore we can use the ideal gas law $p = n_{Hg}kT$ to translate the n_{Hg} -field into a spatial temperature profile [5]. This profile is calibrated with a wall temperature measurement. The wall temperature was measured by infra-red pyrometry using the known emissivity of the burner material [1].

The x-ray absorption measurement of the Hg concentration in metal-halide lamps requires two images: one for the lamp on and the other for the lamp off. By taking the ratio of these images, the absorption of Hg is obtained for each line-of-sight, i.e. for each lateral position. The radial density profile can then be reconstructed by using an inversion procedure called Abel inversion [5]. However, before we can take the ratio of the on-and off images, we have to correct for a variety of image-disturbing influences that are caused by each part of the three-component setup.

The setup consists of three parts: the x-ray source for lamp irradiation, the lamp itself, and the CCD camera for imaging. Each of these components gives cause for its own disturbance of the image. These are listed as follows [1].

The source

1. is of finite dimension that leads to a blurring of the image;
2. has a divergent cone-like beam that makes the CCD image larger than the object;
3. has a non-monochromatic spectrum which will cause a "beam-hardening" effect.

The lamp

1. will shift and expand due to the temperature rise in the on-situation;
2. brings an offset signal due to scattering of the x-rays.

The CCD camera

1. has a dark current;
2. has a non-uniform pixel sensitivity.

Therefore several corrections have to be made in the data-handling before subtraction of the logarithmic on- and off images can take place and Abel inversion can be applied.

We will first focus on the imperfections of the source. The point-source character of the x-ray source causes the image to be magnified. A coordinate transformation is necessary to acquire the correct lateral position needed for the Abel inversion, see [1]. However, since the x-ray source is not a perfect point source but of finite dimension this also results in blurring of the image. We tried to reduce blurring by using a deconvolution technique but we found that this was counter productive as the noise level was increased, so no deconvolution was applied. Beam-hardening [1] has been avoided by choosing an acceleration voltage that results in a quasi-monochromatic beam. Measurements were performed and reported in section 7.4 to examine the severity of this effect.

The lamp itself also causes difficulties in the image reconstruction. The lamp has an unstable position and will move and expand after it is switched on. The thermal expansion also causes the density of the burner wall to decrease. The result of this is that the on-image will have a slightly higher intensity than the off-image. This means that the difference of the absorption between lamp-on and lamp-off can not only be attributed to the presence of an Hg vapour. When the lamp is on, the burner shifts, rotates and expands, a correction is made for these effects in the fitting procedure.

7.2.2 Fitting procedure

The signal on the CCD camera that is created by the intensity of the x-ray beam that, after being partially absorbed by the lamp material reads,

$$I(x, E) = I_0(E)e^{-\tau(x,E)} \quad (7.1)$$

where E equals the photon energy, $I_0(E)$ the intensity of the source, x is the lateral position, and τ the optical depth. The optical depth τ , which is a dimensionless quantity which can be described as $\tau = kd$ with k the absorption coefficient and d the depth; it can also be written as $\tau = \rho\sigma_\rho d$ with σ_ρ the mass absorption coefficient and ρ mass the density. The optical depth has basically has three contributions that it originates from, first the outer bulb, second the wall material of the burner and third the Hg vapour. As we are mainly interested in the Hg vapour the first two contributions have to be removed. This is done by means of lamp-off measurements. The contribution of the outer bulb is minor and is removed before the burner is fitted. The outer bulb curvature is fitted with a parabola which is then subtracted to give a straight profile outside the burner. For the sake of convenience the optical depth of the wall material is cast in an analytical expression of the function

$$y = -\ln(I) \quad (7.2)$$

For the lamp-off situation we can describe the fitting function for two different regions, inside the burner, $0 \leq |x - x_0| < r_1$ and inside the burner wall: $r_1 \leq |x - x_0| \leq r_2$, see figure 7.2 [1];

$$y^{off}(x) = y_0^{off} - 2k \left(\sqrt{r_2^2 - (x - x_0)^2} - \sqrt{r_1^2 - (x - x_0)^2} \right), 0 \leq |x - x_0| < r_1 \quad (7.3)$$

$$y^{off}(x) = y_0^{off} - 2k \left(\sqrt{r_2^2 - (x - x_0)^2} \right), r_1 \leq |x - x_0| \leq r_2 \quad (7.4)$$

where k is an absorption coefficient independent of position. By fitting the experimental data with a non-linear least-squares fit (Levenberg-Marquardt [10]), the parameters y_{off} , k , x_0 , r_1 , r_2 are found. Especially the r_1 -value is important, since it defines the inner-burner wall, which is the boundary of the Abel inversion procedure later in the data-handling.

Before the τ -value of the lamp-off can be subtracted we have to transform the on-fitting function y_0 into y_0^* given by [1]

$$y^{*on}(x, \mathbf{c}) = c_4 + c_3[y^{on}(c_1x + c_2)] \quad (7.5)$$

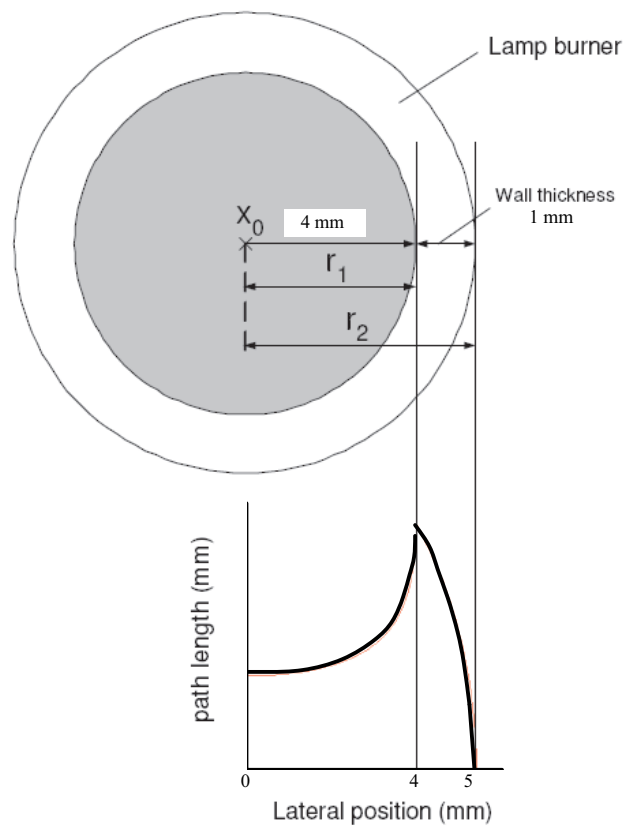


Figure 7.2: The path length through the burner as a function of lateral position [1]. The burner inner radius $r_1 = 4\text{mm}$, the burner outer radius $r_2 = 5\text{mm}$.

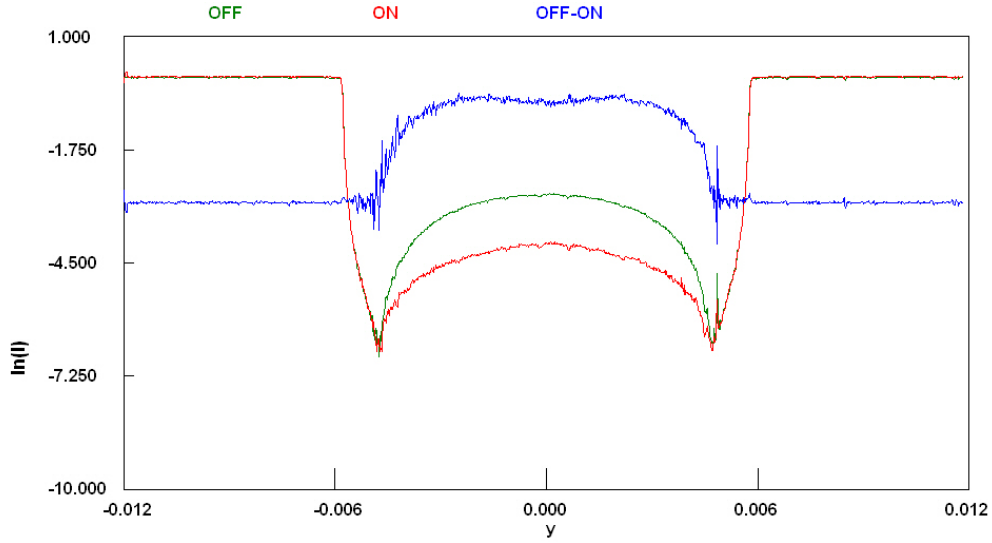


Figure 7.3: Lamp-on and off fitting of at one axial position, the difference between the fitted lamp-on and off profile, also shown, provides the absorption contribution of Hg. The line showing the difference between the on-and off profiles has been moved up by -3 and enlarged for clarity.

Where fitting-vector $\mathbf{c} = (c_1, c_2, c_3, c_4)$ corrects for the expansion and shift of the burner after the lamp is switched on. c_1 corrects for expansion, c_2 for the burner shift, c_3 for the wall-density decrease (due to expansion), c_4 for both dose-inequality (difference between x-ray dose produced by the source between on-and off measurements) and density decrease. These values for \mathbf{c} are found using the same non-linear least-squares fitting method as for the off-profile fitting of equations 7.3 and 7.4.

The total fitting procedure is as follows. First the lamp-off data is fitted using equations 7.3 and 7.4 which yields y_{off} , k , x_0 , r_1 and r_2 . Then the lamp-on data is fitted using equation 7.4 in the area outside the burner-inner wall $|x - x_0| > r_1$, yielding r_1, r_2, x_0 for the lamp-on situation and therefore the initial values for c_1 and c_2 in equation 7.5. These values are then used to determine the density decrease and offset c_3, c_4 and c_1, c_2 by fitting the on-profile onto the off-profile in the area $r_1 < |x - x_0| < r_2$.

The scattering correction was recently introduced in order to correct for the offset I_{off} of the measured intensity profile I_{meas} caused by the scattering of the x-ray photons on the quartz. The offset is subtracted from the measured intensity

$$I = I_{meas} - I_{off}, \quad (7.6)$$

during fitting, thereby adjusting equation 7.2. The laterally integrated Hg density profile $F(x)$ can now be found using [1], see figure 7.3,

$$F(x) = \frac{y^{off}(x) - y^{*on}(x)}{c_3 \bar{\sigma}_{Hg}} \quad (7.7)$$

where $\bar{\sigma}_{Hg}$ is the mean absorption cross-section of Hg [1].

7.2.3 Tikhonov regularized Abel inversion

Radial information can be extracted from the lateral profile $F(x)$ with the Abel inversion procedure. The radial density function is represented by the even-order polynomial function

$$n(r) = \sum_{i=0}^N a_{2i} r^{2i} \quad (7.8)$$

The column density $F(x)$ can be described as [11]

$$F(x) = 2 \cdot \sum_{i=0}^N a_{2i} h_{2i}(x) \quad (7.9)$$

where N determines the order of the fitting-function, i.e. the number of h_{2i} -terms

$$h_{2i}(x) = \int_x^R \frac{r^{2i+1}}{\sqrt{r^2 - x^2}} dr \quad (7.10)$$

The coefficients a_{2i} are evaluated from the data $f_{meas}(x_k)$, which is measured at M points, using a least square estimation

$$\sum_{k=1}^M (F(x_k) - f_{meas}(x_k))^2 \rightarrow \min \quad (7.11)$$

The partial derivative of this condition to the unknown coefficients a_{2i} yields a set of equations. [11]

$$\sum_{i=1}^N a_{2(i-1)} \sum_{k=1}^M h_{2(m-1)}(x_k) h_{2(i-1)}(x_k) = \sum_{k=1}^M h_{2(m-1)}(x_k) f_{meas}(x_k) \quad (7.12)$$

In matrix notation this can be written as

$$\mathbf{M} \cdot \mathbf{a} = \mathbf{b} \quad (7.13)$$

where \mathbf{a} is given by $(a_0, \dots, a_N)^T$ and where \mathbf{b} is the measured data f_{meas} and can be written as

$$\mathbf{b} = (b_1, \dots, b_N)^T, \text{ where } b_m = \sum_{k=1}^M h_{2(m-1)}(x_k) f_{meas}(x_k) \quad (7.14)$$

and \mathbf{M} contains the even-order fitting-polynomials and is given by

$$M_{mi} = \sum_{k=1}^M h_{2(m-1)}(x_k) h_{2(i-1)}(x_k), \text{ for } 1 \leq m \leq N, 1 \leq i \leq N \quad (7.15)$$

where \mathbf{M} is

$$\begin{pmatrix} M_{11} & M_{12} & \dots & M_{1N} \\ M_{21} & M_{22} & \dots & M_{2N} \\ \dots & \dots & \dots & \dots \\ M_{N1} & M_{N2} & \dots & M_{NN} \end{pmatrix}$$

Equation 7.13 can also be written as

$$\mathbf{M}^T \mathbf{M} \cdot \mathbf{a} = \mathbf{M}^T \cdot \mathbf{b} \quad (7.16)$$

Now the unknown coefficients a_{2i} can be found by

$$\mathbf{a} = (\mathbf{M}^T \mathbf{M})^{-1} \mathbf{M}^T \cdot \mathbf{b} \quad (7.17)$$

It would seem that large N (order of fitting function) would be sufficient to fit the data, however, because of the high noise level in the data near the wall, the fit tends to oscillate around the noise instead of following the actual profile. This can be remedied by using a regularisation method that allows for the dampening of such oscillations. A trade-off then needs to be made between the 'size' of the regularised solution and the quality of the fit that it provides to the given data [12]. The regularisation method used to stabilise the solution is called Tikhonov regularisation [13]. Now the fitting parameters \mathbf{a} can be found by

$$\mathbf{a} = (\mathbf{M}^T \mathbf{M} + \mu I)^{-1} \mathbf{M}^T \cdot \mathbf{b} \quad (7.18)$$

where \mathbf{M}^T denotes the transposed matrix (which is equal to \mathbf{M} due to symmetry), μ the Tikhonov parameter which restricts all solutions to the ones with minimum norm. In the inverse procedure, two types of errors are introduced, the approximation error and the noise-propagation error. Since the approximation error increases with μ , whereas the noise-propagation error decreases with μ , there is an optimum value of μ for the inverse problem. A numerical test has to be made for each case in order to get an optimum μ value.

7.3 Experimental setup

A quasi-monochromatic x-ray beam generated by the Mo-anode x-ray tube (equipped with a Zr filter), is directed towards the metal-halide lamp under investigation, see figure 7.4. Part of the radiation will be absorbed while the remaining photons are detected by an x-ray CCD camera. CCD images are taken for two situations, a burning lamp (lamp on) and a non-burning lamp (lamp off). In the off-situation, the Hg is not present in the volume of the burner, but is condensed in small droplets on the wall or (usually) on the electrodes. When the lamp is burning, it is filled with Hg vapour. The Hg in the lamp-on situation causes an additional absorption of the x-ray photons. Therefore, the difference of the absorption signal between the lamp-on and lamp-off cases gives information about the Hg density. In the following sections we discuss the setup, consisting of a source and CCD camera, and the lamp used for the experiments.

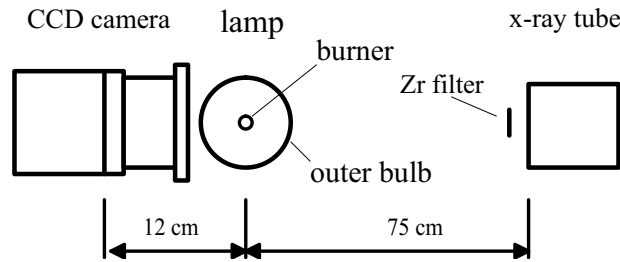


Figure 7.4: Top view of the x-ray absorption spectroscopy setup. The setup consists of a CCD camera, an x-ray tube and a lamp. The camera is shown in more detail in figure 7.5. The entire setup is encased in a box made of lead.

7.3.1 X-ray source

A commercial x-ray source, a Philips PW 1130, initially designed for crystallography, was used for our x-ray absorption experiment of metal-halide lamps. This source has a high brightness and a small focal spot size. The system has a standard tube tower housing, in which different x-ray tubes can be installed. In our XRA experiment, the Mo-anode x-ray tube has been used. The x-ray generator/source operated at 20 mA and 25 kV with an x-ray spot size of 0.4 by 8 mm.

In order to obtain a high spatial resolution, the dimensions of the x-ray emitting area (the anode) must be as small as possible, especially in the horizontal direction, that is in the direction parallel to the lateral dimension x of the metal-halide lamp under investigation. Therefore a fine focus (FF) x-ray tube was used with a focus size of 0.4 mm by 8 mm. The 8 mm refers to the depth, this dimension pointing more or less in the direction of the x-ray source lamp. The 0.4 mm size is parallel to the lateral direction x . See [1] for more details.

To reach a good spatial resolution ($100 \mu\text{m}$) with an x-ray focal spot of relatively large dimensions (0.4 mm in lateral direction), the vertically positioned metal-halide lamp has been placed far from the source, namely at a distance of 75 cm. Typical integration time is 120 s per image, multiple images (typical 100) are taken to increase the signal to noise ratio.

The Mo anode x-ray tube has a spectrum that contains two typical Mo K-lines ($K\alpha$: 17.5 keV, $K\beta$: 19.6 keV). The Zr filter has a K-absorption edge at 18 keV, causing the X-ray spectrum above 18 keV to be strongly absorbed. Thus the spectrum from the X-ray source is expected to consist mainly of the Mo $K\alpha$ (17.5 keV) line super-imposed on a continuous background of Bremsstrahlung radiation. The energy below 15 keV will be further attenuated by the outer bulb of the metal-halide lamp. Therefore we can assume that the spectrum of the radiation offered to the burner is quasi-monochromatic and mainly consisting of the Mo $K\alpha$ line [1]. Beam-hardening occurs when the source is not monochromatic enough, this was studied by placing several slides of quartz in front of the CCD in consecutive order, the results of this test is presented in section IV.

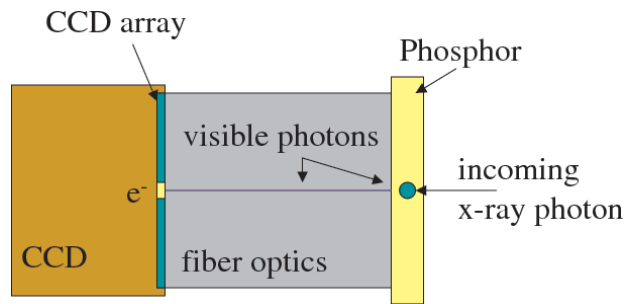


Figure 7.5: The PI-SCX1300 CCD consists of three parts, a phosphor sheet, fiber optics and the CCD array. The CCD array contains 1340 x 1300 pixels of $20\mu\text{m}$ by $20\mu\text{m}$ each.

7.3.2 CCD camera

In order to detect the x-ray photons that have passed through the metal-halide lamp we use an x-ray CCD camera, a PI SCX 1300. The crucial part of this device is a CCD-array of a type that is well-known for applications of image registration. However, since the CCD-array is not sensitive for hard x-ray radiation the x-ray quanta have to be converted into visible photons. During that conversion, effectuated by a phosphor plate, the x-ray photon generates a large number of visible photons as the energy of an x-ray photon (typically 17 keV) is much larger than that of a visible photon. [1]. Figure 7.5 shows the main parts of which of the x-ray CCD camera consists, a phosphor sheet, fiber optics and the CCD-array.

7.3.3 The lamp

The lamp consists of an 8 mm inner diameter quartz arc tube surrounded by a quartz outer bulb. The inner diameter of the outer bulb is 120 mm. This is much larger than in the previous measurements done by Zhu [1], there the outer bulb of the metal-halide COST lamp [14] [15] had an inner diameter of 20 mm. The wall thickness of both burner and outer-bulb is typically 1 mm. The benefits of a larger outer bulb are twofold. First, by using a larger outer bulb the effect of the curvature of the outer bulb on the detected absorption signal can be much better approximated with a parabolic fit. Second, there is less wall material to traverse through near the edge which results in a higher signal. The electrode gap is 18 mm. Two different lamps were investigated, one containing only 10 mg of Hg, the other 10 mg of Hg with 4 mg of DyI_3 . For the measurements presented here, the lamp was operated vertically at a power of 145 W. The power was supplied by a square-wave ballast programmed at a frequency of 122 Hz.

7.4 Results and Discussion

The experiment and principle method were developed by Zhu [1] in order to obtain the temperature distribution from the measured absorption of the x-rays by the Hg in the

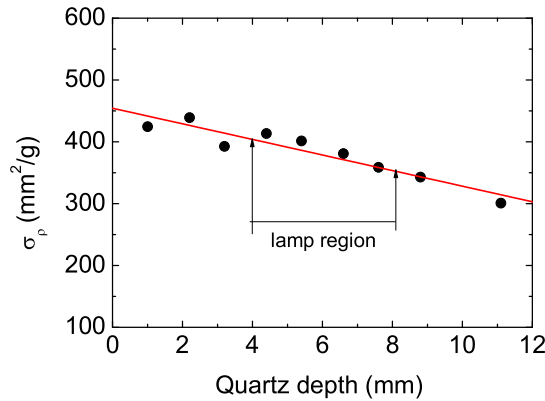


Figure 7.6: Mass absorption coefficient as a function of quartz thickness. At the centre of the burner the quartz thickness is 4mm at the wall this is 8 mm. It is shown that, due to beam-hardening, the absorption coefficient decreases for increasing path lengths; however this effect is limited as long as we stay below a quartz depth of 8 mm.

arc. However, a number of remaining problems had yet to be addressed. These are beam-hardening, scatter of x-rays by the lamp materials and an optimum value for the Tikhonov parameter μ . In this section we discuss these three aspects and the resulting temperature distribution of two lamps, without and with salt (DyI_3).

7.4.1 Beam-hardening

Beam-hardening occurs when low energy photons are absorbed more readily than high energy photons as the path length increases. As a consequence each absorbing material will act as a filter; the 'soft' (low energy) photons are removed from the beam; the 'hard' (high energy) photons remain. This not only alters the transmitted spectrum but changes the mean cross-section. For longer path-lengths the material will become relatively more transparent. This might affect the measurement near the wall of the burner, where the amount of quartz that is traversed by the x-ray is highest. To examine the significance of this effect in our measurements, a set of 10 quartz slides were placed consecutively in front of the CCD. An image was taken after each placement of a slide. The photon energy of the beam is partly absorbed by the quartz, the transmitted intensity is measured by the CCD camera and can be described as

$$I(d) = I_0(E)e^{-\sigma_p \cdot \rho \cdot d} \quad (7.19)$$

where I is the intensity of the beam, I_0 is the intensity of the beam before traversing through quartz, E the beam energy, σ_p the mass absorption coefficient for quartz [1], ρ the quartz mass density d and the quartz depth.

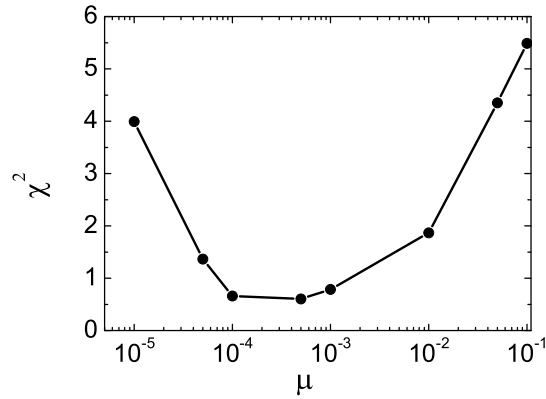


Figure 7.7: A typical curve of the chi-square as a function of the different μ -values. The minimum of the curve is found at $\mu \approx 10^{-4}$.

The mass absorption coefficient σ_ρ is plotted as a function of the quartz thickness in figure 7.6. It shows that the absorption coefficient decreases as the thickness increases. In the case of the lamp, the minimum quartz thickness that is penetrated by the x-rays is 4 mm (through the centre), the maximum is 8 mm (directly at the inner-burner wall). Figure 7.6 shows that this leads to an error of around 5% at the minimum thickness and 16% at the maximum thickness, this is comparable to the error made during fitting near the wall and can therefore be neglected. The systematic error caused by the beam-hardening effect leads to an underestimation of the axis temperature of about 10%.

7.4.2 Tikhonov regularisation parameter μ

The Abel inversion was regularised as was discussed in section 7.2.3 with Tikhonov parameter μ . The optimum value of μ was found by comparing the temperature profile generated by a model with a measured temperature profile. This model was created by R. Cornelis *et al* [16] to simulate the x-ray measurement procedure. A theoretical temperature profile, based on the one proposed by Fischer [9] was used as input data. The program then simulated the lamp images on-and off. The simulated images were then analysed using the same method as was used for the measurements. The measured temperature profile was determined with different values for μ . A chi-square evaluation was then performed for the difference between the model and experimental profiles

$$\chi^2 = \frac{1}{T_{eff}N} \sum_i (T_i^{sim} - T_i^{meas})^2, \quad (7.20)$$

where T_{eff} is the effective temperature [9] taken as 3000 K, N is the number of datapoints, and T_i^{sim} and T_i^{meas} are the simulated and measured temperature profile respectively.

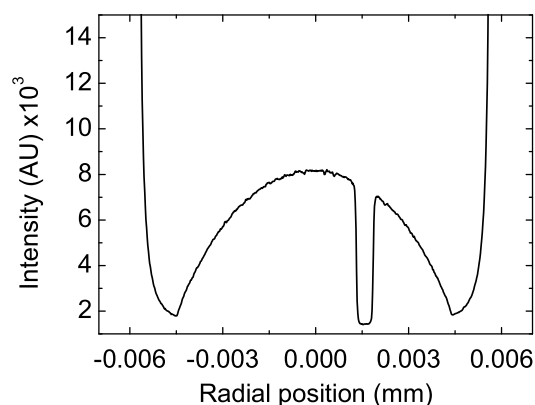


Figure 7.8: The lamp intensity after it is blocked by the messing strip, taken at the midplane of the lamp. The lamp was moved with respect to the strip.

A typical curve of the chi-square as a function of the different μ -values is shown in figure 7.7. The minimum of the curve is found at $\mu \approx 10^{-4}$. This value was subsequently used as the Tikhonov parameter for the Abel fitting of the intensity curves necessary for the calculation of the temperature profiles. Finally, 16 Abel terms were used instead of the previous 11 terms [1], allowing for a better approximation of the lateral profile.

7.4.3 Scattering of x-rays

The offset, as was discovered by X Zhu, was investigated. She found this offset when horizontal brass strips were placed in front of the camera. The strips were expected to block the signal completely, however a signal of about 14% of the unblocked signal was found [1]. This phenomenon is most likely caused by the scatter of x-ray photons by the quartz burner. This was further examined by placing a strip of 500 microns wide vertically between the CCD and the lamp. See figure 7.8. The (non-burning) lamp was then moved laterally so that the strip blocked the incoming x-rays for different horizontal positions of the lamp. The average value of the signal found behind the blocking strip as a function of lateral position is depicted in figure 7.9. The values found were used for the scattering correction in the data-analysis program. This allowed for a much better fit of the intensity profile near the wall. This part of the profile has a very steep gradient, so that an appropriate determination of this region is of the utmost importance. The new scattering correction resulted in an increase of the axis temperature with more than 1000K compared to previously reported temperature profiles [1].

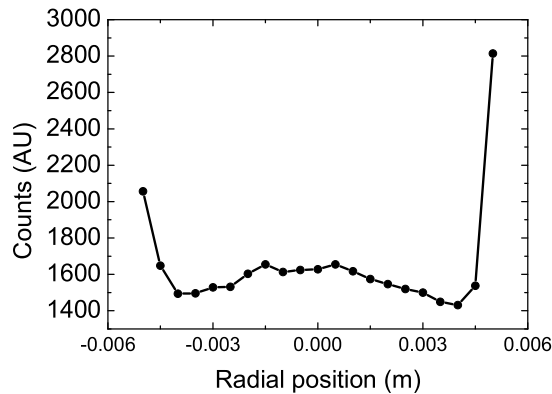


Figure 7.9: Offset found after a thin messing strip of $500 \mu\text{m}$ wide has been placed in front of the CCD camera (see figure 7.8). The lamp was moved with respect to the strip. The values found near the wall (about 1450 counts) were used for the scattering correction factor in the data analysis. This provided a much better fitting near the wall of the burner.

7.4.4 Temperature distribution

Two typical examples of a temperature distribution are shown in figure 7.10 and 7.11. Figure 7.10 shows the temperature distribution of an metal-halide lamp containing 10 mg of Hg. The axis temperature at the midplane of the lamp is 6000 K. The error is approximately 10%. Near the electrodes the arc contracts due to the shape of the electric field. In between the shape of the profile is near-parabolic.

Figure 7.11 shows the temperature distribution of an metal-halide lamp containing 10 mg of Hg and DyI_3 . The axis temperature at the midplane is about 6200 K. This is more than 1000 K higher than reported by Zhu [1], but comparable to the results obtained by optical emission spectroscopy [7] [9] [18]. The ratio of the axis temperature and the wall temperature is 4.7. This is much closer to the ratio of 4.6, which was obtained with the temperature profile obtained by emission spectroscopy [9] combined with the wall temperature measurement [1], than the ratio of 3.6 measured by Zhu [1].

Like the lamp containing pure Hg, the arc contracts near the electrodes and is near-parabolic in between. However, comparing the profile close to the lower electrode to that close to the top electrode, it is clear that the profile close to the lower electrode shows more contraction [9]. Axial segregation causes most of the Dy, which is an excellent radiator, to be present at the bottom of the lamp. Dy causes the arc to cool locally near the flank of the discharge resulting in contraction [9] [18]. This contraction near the lower electrode of a nominally identical lamp was also reported by X. Zhu [1].

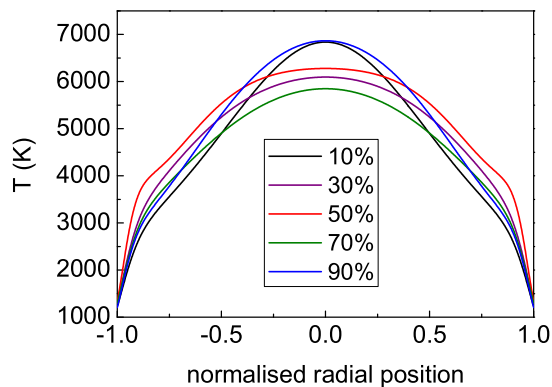


Figure 7.10: Radial temperature profiles at different axial positions for a Hg pure lamp. The radius is 4 mm and the electrode distance 18 mm. The axial positions are given as a fraction of the total arc-length starting with the bottom electrode. From top to bottom, at the central radial position, the axial positions are as follows, 90 %, 10 %, 50 %, 30 %, 70 %

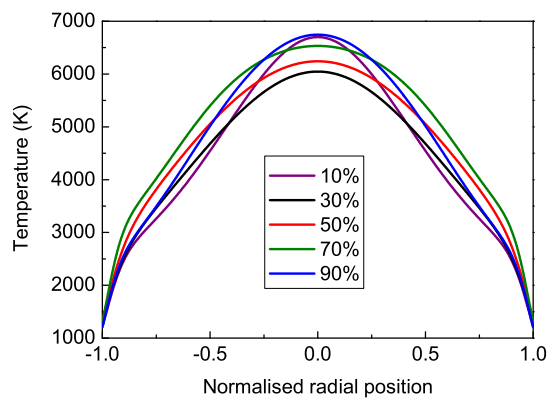


Figure 7.11: Radial temperature profiles at different axial positions for a lamp containing Hg and DyI₃. The radius is 4 mm and the electrode distance 18 mm. The axial positions are given as a fraction of the total arc-length starting with the bottom electrode. From top to bottom, at the central radial position, the axial positions are as follows, 90 %, 10 %, 70 %, 50 %, 30 %

7.5 Conclusions

The data-analysis of the x-ray absorption technique has been improved, leading to an axis temperature of about 6200 K in a metal-halide lamp containing Hg and DyI₃. This is in agreement with optical emission spectroscopy measurements done previously. The axis-to-wall temperature ratio of the x-ray absorption is also much more comparable to the emission spectroscopy measurements than earlier reported results obtained with the same setup [13]. It is the scattering of the x-rays on the quartz burners that were found to have such a profound effect. Taking this effect into account allowed for a much better fitting, causing the temperature profiles to be 1000 K higher than the previously reported temperatures of the same setup.

The Abel inversion was regularized with an optimised Tikhonov parameter $\mu = 10^{-4}$. Beam-hardening was found to be negligible, which led to the conclusion that the source is near mono-chromatic due to the combined effect of the Zr filter and the absorption of the wall material. The temperature profile of the lamp containing DyI₃ was mostly contracted near the bottom of the lamp. This is where most of the atomic Dy is present and causes local cooling of the flank of the discharge. Future plans include x-ray absorption of metal-halide lamps with a variety of fillings such as NaI, TII, DyI₃ and a combination of these.

7.6 Acknowledgments

This research is sponsored by the Technologiestichting STW (project No. ETF 6093) and COST (project 529).

Bibliography

- [1] Zhu X, PhD thesis: *active spectroscopy on HID lamps*, Eindhoven University of Technology,(2005)
- [2] Lister G G, Lawler J E, Lapatovich W P and Godyak V A 2004 Rev. Mod. Phys. **76**, 541
- [3] Coaton J R, Marsden A M, Lamps and Lighting, Arnold, London, 4th edition, 1997
- [4] Fischer E 1976 J. Appl. Phys. **47**, 2954
- [5] Curry J J, Sakai M and Lawler J E 1998 J. Appl. Phys. **84**, 3066
- [6] Fohl T, Kramer J M and Lester J E 1993 J Appl Phys 73 46
- [7] Nimalasuriya T, Pupat N B M, Flikweert A J, Stoffels W W, Haverlag M and Van der Mullen J J A M 2006 J. Appl. Phys. **99** 053302 **see chapter 2**
- [8] J.A.M. Van der Mullen, Phys. Rep. **191** 109 (1990)
- [9] Nimalasuriya T, Flikweert A J, Haverlag M, Kemps P C M, Kroesen G M W, Stoffels W W, Van der Mullen J J A M 2006 *J. Phys D: Appl Phys* **39** 2993 **see chapter 3**
- [10] Press W H, Flannery B P, Teukolsky S A 1989 *Numerical recipes in Pascal, the art of scientific computing* Cambridge University Press.
- [11] Pretzler G, *A New Method for Numerical Abel-Inversion*, Z. Naturforsch. 46a, 1991, pages 639-641
- [12] Hansen P C, The L-curve and its use in the numerical treatment of inverse problems
- [13] M.Bertero and Boccacci P 1998 Introduction to inverse problems in imaging (Bristol and Philadelphia: Institute of Physics Publishing)
- [14] Stoffels W W, Flikweert A J, Nimalasuriya T, Van der Mullen J J A M, Kroesen G M W, Haverlag M, 2006 Pure Appl. Chem. **78** No 6
- [15] Nimalasuriya T, Curry J J, Sansonetti C J, Ridderhof E J, Shastri S D, Flikweert A J, Stoffels W W, Haverlag M, Van der Mullen, J J A M 2007 J.Phys.D **40**, 2831 **see chapter 6**
- [16] Cornelis R 2006, MSc Thesis, X-Ray Absorption measurements and measurement simulations on HID lamps, Eindhoven University of Technology
- [17] Denisova N, Haverlag M, Ridderhof E J, Nimalasuriya T, Van der Mullen J J A M, to be submitted

- [18] Nimalasuriya T, Thubé G M, Flikweert A J, Haverlag M, Kroesen G M W, Stoffels W W, Van der Mullen 2007, *J.Phys.D* 2007 **40** 2839 see **chapter 4**

X-ray absorption of the mercury distribution in a commercial metal-halide lamp

Abstract. The radial temperature profile of a commercial metal-halide lamp and of lamps containing its individual components have been acquired using x-ray absorption (XRA) of the Hg density distribution. The temperature profiles were determined by combining the measured absorption of the spatially resolved Hg density with the wall temperature. The lamps studied were a commercial lamp, i.e. the Philips CDM-T 70 W/830; and identically shaped lamps containing NaI, DyI₃ and TlI separately. It was found that the element Dy contracts the arc, Na broadens the arc while Tl causes the arc to have so-called 'shoulders'. Combined in the commercial lamp this lead to a wall-stabilised arc without the contraction and 'shoulders'. A reproducibility test with identical lamps was also made and showed that the error in the temperature profile is about 8 % for the absolute temperature and only 1.6% for the actual shape of the profile.



Figure 8.1: Colour separation in a metal-halide lamp burner. The lamp is burned vertically upright. See figure 1.1 for full colour.

8.1 Introduction

The metal-halide lamp [1] consists of a buffergas of Hg and a small amount of metal-halide additives. The metals generate a myriad of lines in the visible part of the spectrum which results in high luminous efficacy and colour rendering. The metals themselves have low vapour pressure and tend to attack the walls of the burner at high temperatures [2]. These problems are avoided by using metal-halide salts such as DyI_3 , TlI and/or NaI . In the metal-halide lamp a mixture of such salts are used in order to obtain a good colour rendering index. Mixtures such as $(\text{NaI} + \text{ScI}_3)$, $(\text{NaI} + \text{TlI} + \text{InI})$ or $(\text{NaI} + \text{TlI} + \text{DyI}_3 + \text{HoI}_3 + \text{TmI}_3)$ are commonly used in metal-halide lamps. Due to the competition between diffusive and convective processes these additives are non-uniformly distributed over the lamp, which in a vertical burning position results in a undesirable segregation of colours [3], see figure 8.1.

It is currently beyond our capabilities to fully understand a commercial metal-halide lamp with its complex shape and chemistry. Therefore poly-diagnostic experiments [4–10] have been performed on a reference lamp with a simple geometry and chemistry [11]. This reference lamp contains only one salt, which makes it easier to model. It would, however, be interesting to investigate a commercial lamp, which contains a mixture of species.

In order to gain a better understanding of the temperature distribution of the commercial lamp, it is also necessary to study its individual components. Therefore three salt components that make up the commercial lamp, TlI , NaI , DyI_3 have been placed in separate lamps and measured by x-ray absorption. All lamps contain the same dosage of Hg as a buffer-gas. X-ray absorption (XRA) [4] [12–14] was used to measure the distribution of Hg atoms. This is done by irradiating the lamp with x-rays and by detecting the absorption of the x-ray photons in the whole lamp-burner. A temperature profile at different axial

positions of the discharge can then be obtained by applying the ideal gas law combined with the wall temperature.

The experiment and data-handling was designed by Zhu [4] and has been extensively examined and improved [14]. The latter study only investigated the two reference lamps as described earlier, namely the pure Hg and the Hg with DyI₃ lamp. Now the method has been improved it is of interest to focus on the application of XRA on a variety of lamps, such as the commercial Philips CDM-T 70 W/830 lamp.

Several methods are available for the determination of the temperature distribution in a discharge. Optical methods such as the determination of spectral line profiles [15–17] yield good results, but are limited to the central region of the discharge. X-ray induced fluorescence measurement of the Hg density distribution [9] performed earlier can measure the entire lamp but does not have the required spatial resolution to deal with the steep temperature gradient near the wall. XRA, however, has the benefit of both high spatial resolution and the ability to measure the entire lamp. Previous XRA measurements were performed by Fohl *et al* [18] and Curry *et al* [19]. The temperature for the latter was calibrated using an optical technique to determine the axis temperature. Our approach is different in the sense that the obtained relative temperature field is calibrated with an absolute measurement of the wall temperature, by infrared pyrometry [4]. In this paper the wall temperature is based on previous measurements done at Philips Lighting on similar lamps.

This chapter is organized as follows. Section 8.2 describes briefly the data-analysis necessary to obtain the temperature of the arc. Section 8.3 describes the lamps used in the experiments and the experimental setup. Results from the experiments are presented and discussed in section 8.4. These results include temperature profiles for the commercial lamp and its individual components and a reproducibility study. Finally, section 8.5 offers conclusions.

8.2 Theory

The basic process of XRA is that due to the interaction with inner-shell electrons x-ray photons are removed from the beam. Since the density of the buffer gas Hg outranges that of the other species, the primary observable is the Hg density distribution n_{Hg} . Therefore we can use the ideal gas law $p = n_{Hg}kT$ to translate the n_{Hg} -field into a spatial temperature profile [19]. This profile is calibrated with a wall temperature measurement.

The x-ray absorption measurement of the Hg concentration in metal-halide lamps requires two images: one for the lamp on and the other for the lamp off. By taking the ratio of these images (see figure 8.2), the absorption of Hg is obtained for each line-of-sight, i.e. for each lateral position. The radial density profile can then be reconstructed by using an inversion procedure called Abel inversion [20] [21], where the radial density function is represented by the even-order polynomial function.

We have to correct for a variety of image-disturbing influences that are caused by each part of the setup before the the ratio of the on and off-images can be taken. The main

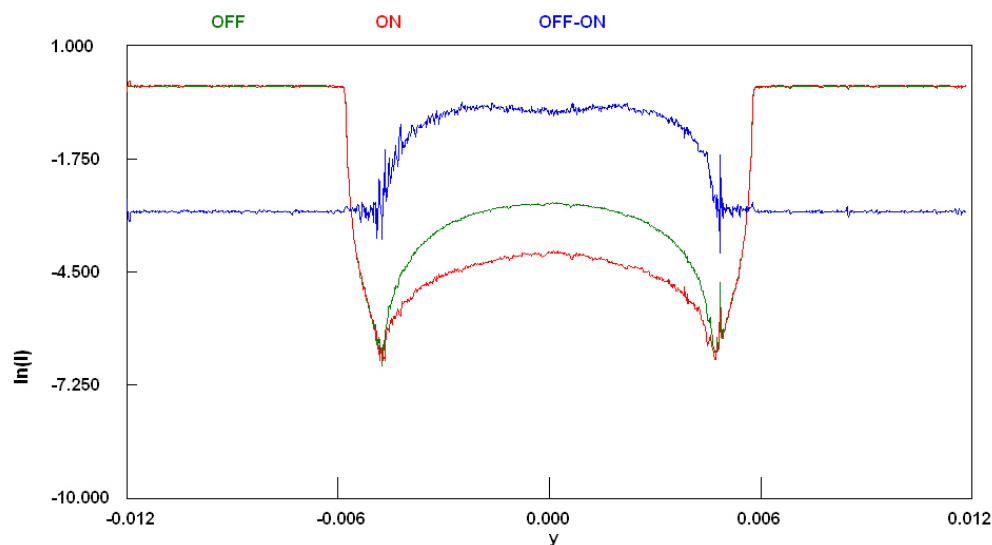


Figure 8.2: Lamp-on and off fitting of at one axial position, the difference between the fitted lamp-on and off profile, also shown, provides the absorption contribution of Hg. The line showing the difference between the on-and off profiles has been moved up by -3 and enlarged for clarity.

disturbing influences include the movement of the lamp during imaging, the blurring of the image caused by the finite dimension of the source and the scattering of the x-rays on the lamp materials. All disturbances are dealt with in the data-analysis procedure. The image disturbance and data-analysis has been studied extensively and reported in [4] [14].

8.3 Experimental setup

The setup, see figure 8.3, consists of three parts: the x-ray source for lamp irradiation, the lamp itself, and the CCD camera for imaging. A quasi-monochromatic x-ray beam generated by the Mo-anode x-ray tube, equipped with a Zr filter, is directed towards the metal-halide lamp under investigation, see figure 8.3. Part of the radiation will be absorbed while the remaining photons are detected by an x-ray CCD camera. CCD images are taken for two situations, a burning lamp (lamp on) and a non-burning lamp (lamp off). In the off-situation, the mercury is not present in the volume of the burner, but is condensed in small droplets on the wall or (usually) on the electrodes. When the lamp is burning, it is filled with mercury vapour. The mercury in the lamp-on situation causes an additional absorption of the x-ray photons. Therefore, the difference of the absorption signal between the lamp-on and lamp-off cases gives information on the mercury density [4]. It has been established that the vapour pressure of the salt-components are too low to contribute to the measurement of Hg. In the following sections we discuss the setup, consisting of a source and CCD camera, and the lamp used for the experiments.

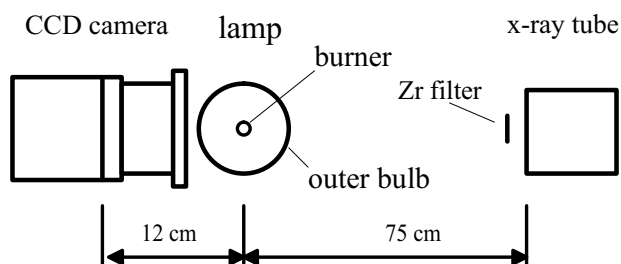


Figure 8.3: Top view of the x-ray absorption spectroscopy setup. The setup consists of a CCD camera, an x-ray tube and a lamp. The entire setup is encased in a box made of lead.

8.3.1 The lamp

The lamp consists of an 6.8 mm inner diameter PCA arc tube surrounded by a quartz outer bulb. The inner diameter of the outer bulb is 120 mm. The wall thickness of the burner is 0.55 mm. This is somewhat smaller than the 0.8 mm wall thickness that is used in the actual 70 W lamps on the market and were especially made for this experiment. A thin burner wall allows more x-rays to penetrate the area near the wall, dramatically improving signal-to-noise. The outer-bulb thickness is typically 1 mm. The inner length of the burner is 7 mm, as the electrodes do not protrude much above this, the electrode gap is therefore also approximately 7 mm.

Six different lamps were investigated, three pure Tl lamps containing 3.2, 5.6 and 8.0 mg TII; one DyI_3 lamp, one NaI lamp and finally a lamp containing a mixture of NaI, DyI_3 , TII, HoI_3 , TmI_3 . The latter is a commercial lamp mix, which is used in the Philips CDM-T 70 W/830. All lamps were built in the large quartz outer bulb for the experiment, see [14]. All six lamps contain 4.5 mg of Hg yielding a lamp pressure of about 30 bar. For the measurements presented here, the lamp was operated vertically at a power of 70 W. The power was supplied by an electronic square-wave ballast at a frequency of 122 Hz.

8.4 Results and Discussion

In order to gain a better understanding of the behaviour of the commercial lamp, both the individual chemical components were studied in individual lamps as was the commercial lamp itself, which is a mixture of these components. The components that are studied separately are DyI_3 , NaI, and TII. The commercial lamp contains these components plus the salts HoI_3 and TmI_3 but given the character of these rare earth components and their spectra it is expected that a DyI_3 lamp is representative for the $\text{DyI}_3/\text{HoI}_3/\text{TmI}_3$ mix.

The wall temperature is estimated to be 1350 K for these type of lamps. This temperature however is based on infrared pyrometry measurements done on a commercial lamp with a burner thickness of 0.8 mm. Because our lamps have a thinner burner thickness of 0.55 the wall temperature is estimated to be slightly higher and to be approximately 1400 K.

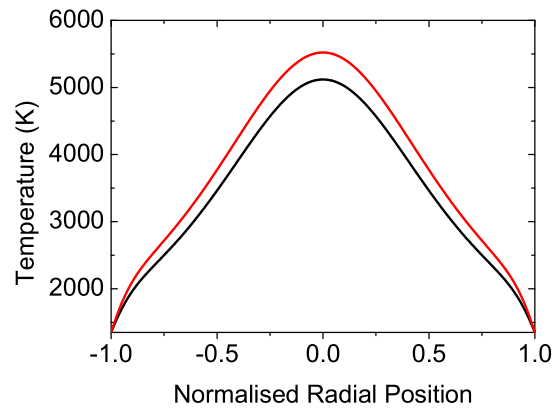


Figure 8.4: Radial temperature profiles at the midplane for two nominally identical lamps containing NaI and 4.5 mg Hg.

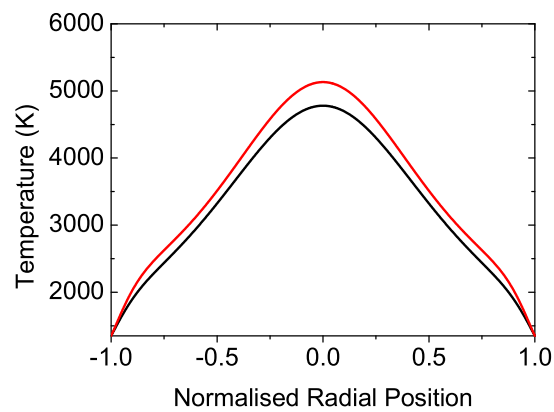


Figure 8.5: Radial temperature profiles at the midplane for two nominally identical commercial CDM-T 70 W/830 lamps.

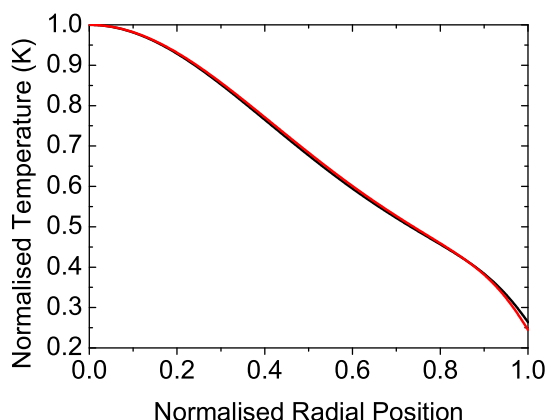


Figure 8.6: Normalised radial temperature profiles at the midplane for two nominally identical lamps containing NaI and 4.5 mg Hg.

In order to estimate the error of the temperature profiles two sets of identical lamps were measured, one set of two pure NaI lamps and the other of commercial lamps. The results of the radial temperature profiles are shown in the figures 8.4 and 8.5 for the NaI and the commercial lamps respectively. The axis temperatures show a difference of 8%, this is therefore assumed to be an indication of the error in the axis temperature. The error in the actual shape of the profile is studied by normalising the axis temperatures, see figures 8.6 and 8.7 for the NaI and commercial lamp. The difference between the temperature profiles are taken mid-radius and show that the error in shape is much smaller than the error in the axis temperature, namely 1.6%.

The radial temperature distribution of the mixture and the individual components were determined at the midplane and are shown in figure 8.8. In order to get a better view of each of the components the radial temperature profiles were normalised at the centre of the lamp, see figure 8.9.

The figure shows that Dy contracts the arc. The Dy spectrum consists of a myriad of optically thin lines. This means that most of the molecular and atomic radiation can escape the discharge which leads to cooling. Since this is mostly at the flanks, the arc contracts. The temperature of the pure DyI_3 lamp at the centre is about 4900. In contrast, Na has a spectrum that consists mainly of a few self-reversed resonance lines. The re-absorption of the Na lines occurs along the whole radius of the discharge, so the profile broadens as is shown in figure 8.9. The temperature at the centre of the pure NaI lamp is 5100 K. It is not possible to assess which of DyI_3 and NaI axis temperatures are actually higher given the limited accuracy of the experiment.

The results for a lamp containing 3.2 mg TII show that the temperature gradient at the wall is about twice as high for TII than for any of the other salts. Between 2500 and 3500 K the gradient sharply decreases thereby creating a 'shoulder'. The decrease in

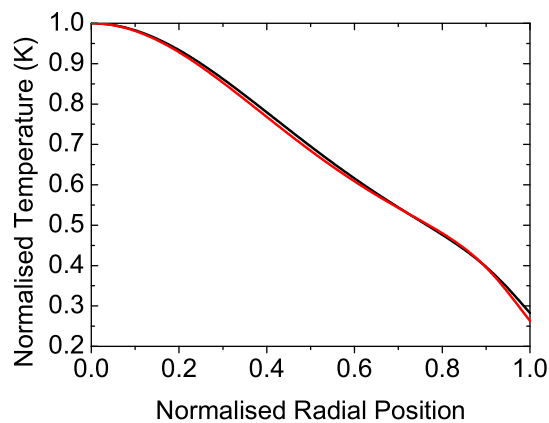


Figure 8.7: Normalised radial temperature profiles at the midplane for two nominally identical commercial CDM-T 70 W/830 lamps.

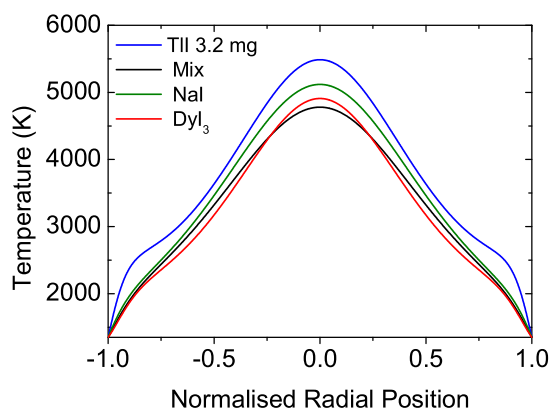


Figure 8.8: Radial temperature profiles at the midplane for lamps with 4 different fillings: pure NaI, pure DyI₃, pure Tl (3.2 mg) and a commercial CDM-T 70 W/830 lamp that contains a mixture of these, all lamps also contained 4.5 mg Hg. At the central radial position, the order of the profiles from the top is as follows, TII, NaI and DyI₃; the lowest profile is from the commercial lamp

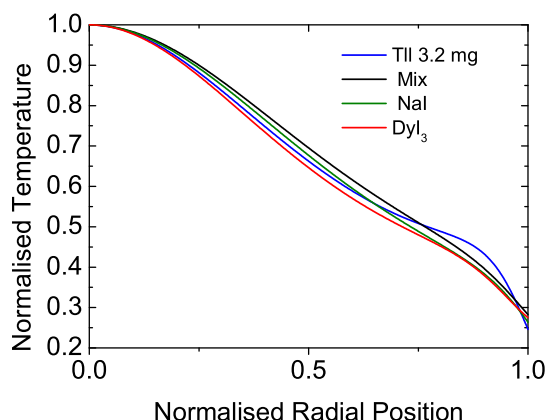


Figure 8.9: Normalised radial temperature profiles at the midplane of lamps with 4 different fillings: pure NaI, pure DyI₃, pure Tl (3.2 mg) and a commercial CDM-T 70 W/830 lamp that contains a mixture of these, all lamps also contained 4.5 mg Hg. At mid-radius, the order of the profiles from the top is as follows, the commercial lamp, the NaI, TII and DyI₃ lamps.

temperature gradient occurs in the temperature interval where the TII molecules dissociate into Tl atoms. Chemical calculations [22] show that the region where the equilibrium shifts from Tl molecules to Tl atoms is between 2000 and 4000 K, see figure 8.10. This shift is accompanied by the release of chemical enthalpy causing an increase in thermal conductivity [26], leading to the 'shoulder' in the temperature profile. This shoulder is not observed in the other pure salt-lamps because the vapour pressure is too low.

The commercial CDM-T 70 W/830, which consists of a mixture, combines the effects of the DyI₃ (and thereby of HoI₃ and TmI₃), NaI and TII which results in a non-constricted arc with a temperature at the centre of around 4800 K.

In contrast to DyI₃ and NaI, it is more likely for TII to evaporate completely in the lamp, so it is of interest to investigate lamps with different fillings. A total of three lamps with 8.0, 5.6 and 3.2 mg of TII were measured. The results are shown in figure 8.11. The profiles are determined at the midplane of the lamp. The average axis temperature for all three lamps is around 5500 K within the 8% error margin. To aid comparison the temperature profiles were normalised, see figure 8.12. The profiles are nearly identical, it is therefore of interest to find out how much Tl is actually in the discharge.

Emission spectra of the lamps containing Tl give insight in the amounts of Tl in the discharge. Four spectra of the three Tl lamps and the commercial lamp, containing the mixture, are shown in figure 8.13. The intensity is normalised at 535 nm. The line widths for the three different pure Tl lamps at 535 nm show that the amount of Tl in the discharge is comparable. This is consistent with the nearly identical temperature profiles of the three lamps. It is clear not all TII has entered the discharge. Apparently, in all cases the TII forms a saturated vapour at a similar cold-spot temperature in all three lamps. The spectra

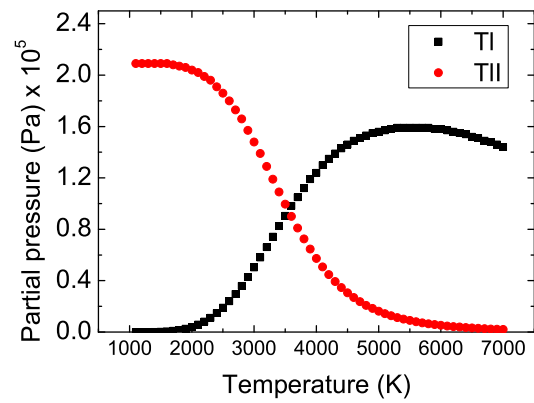


Figure 8.10: Chemical calculation [22] where 8 mg TII, 8 bar Hg, a lamp volume of 1 cm³ and a cold-spot temperature of 1100 K were assumed.

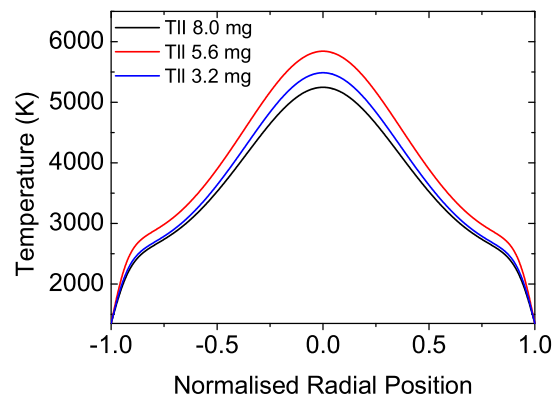


Figure 8.11: Radial temperature profiles at the midplane of lamps containing pure Tl and 4.5 mg Hg. At the central radial position, the TII filling is in the following order, 5.6 mg, 3.2 mg and 8.0 mg.

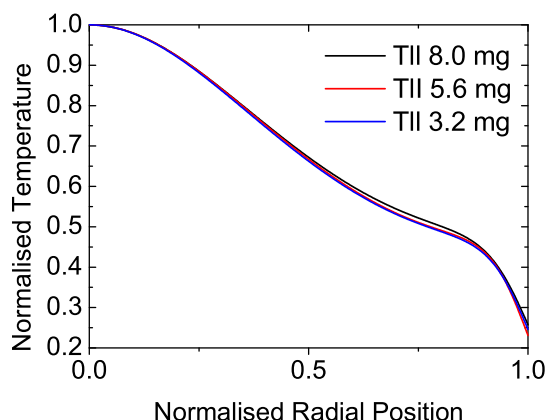


Figure 8.12: Normalised radial temperature profiles at the midplane for three different TII lamps containing 8.0, 5.6 and 3.2 mg of Tl and 4.5 mg of Hg. At mid-radius the order of the profiles is 8.0 mg, 5.6 mg and 3.2 mg.

also show that the vapour pressure of Tl in the commercial lamp is much lower than in the three pure Tl lamps. This explains why the shoulder of the Tl vapour is much less pronounced in the discharge containing the mixture.

Finally, a check of the validity of the experiments is made by the calculation of the absolute Hg density [4]. For this the x-ray absorption cross-section of $3.74 \cdot 10^{-24} \text{ m}^2$ [24] for the mean x-ray photon energy absorbed by the Hg at 17.6 keV is used. The density of the commercial lamp is shown in figure 8.14. It shows a density of $4.0 \cdot 10^{25} \text{ m}^{-3}$ at the centre and $1.4 \cdot 10^{26} \text{ m}^{-3}$ at the wall of the discharge. This leads to a pressure of 26 bar, this is consistent with the 30 bar of Hg in the lamp within the error margin, which is mainly related to the uncertainty of the cross-section and the effective x-ray energy.

8.5 Conclusions

The commercial metal-halide lamp temperature profile combines the effects of its various salt constituents. The metals in these lamps are mainly Dy, Na and Tl. Dy causes the profile to contract, whereas Na tends to broaden the profile, cancelling the contraction caused by the Dy. Tl has a pronounced effect on the shape of the temperature profile of a pure Tl lamp. The temperature profiles clearly show a region where the atoms associate into molecules and vice versa. This region has a sharply decreased temperature gradient and occurs between 2500 and 3500 K. The commercial lamp on the other hand has much less Tl in the discharge than the pure Tl lamps, causing the influence of Tl to be much less severe. The pure Tl lamps contain the same amount of Tl pressure, despite the fact that they have different fillings. The results are found to be reproducible for different identical lamps of the same filling, the error is axis temperature is found to be 8 % and for the

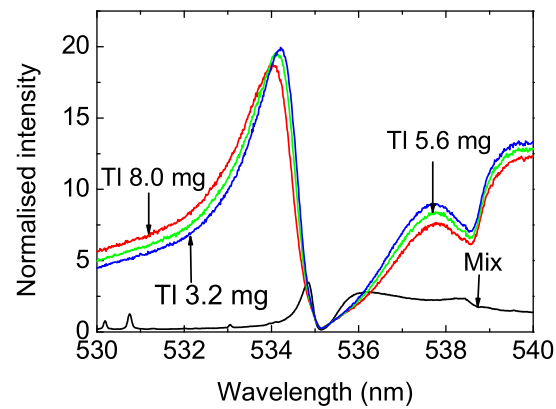


Figure 8.13: Spectra measured for three Tl lamps and one commercial CDM-T 70 W/830 lamp containing a mixture of NaI, DyI₃ and TlI. The intensity of the spectrum is normalised at 535 nm.

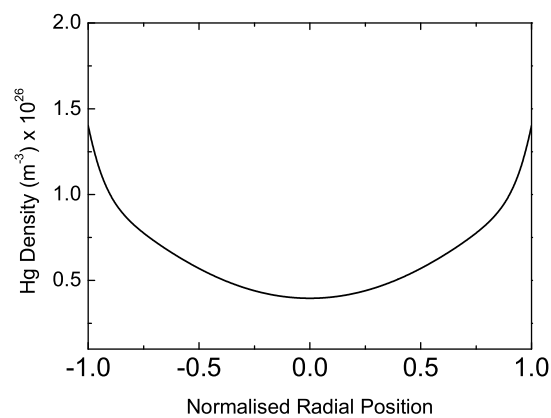


Figure 8.14: Density for the commercial CDM-T 70 W/830 lamp, determined from the mid-plane.

profile shape 1.6 %.

8.6 Acknowledgments

This research is sponsored by the Technologiestichting STW (project No. ETF 6093) and COST (project 529). The authors would like to thank M. van Grunsven and F. Vermeulen of Philips Lighting for supplying the lamps used in this study.

Bibliography

- [1] Lister G G, Lawler J E, Lapatovich W P and Godyak V A 2004 Rev. Mod. Phys. **76**, 541
- [2] Flesch P, *Light and light sources High intensity discharge lamps*, Springer-verlag, Berlin Heidelberg, 2006
- [3] Fischer E 1976 J. Appl. Phys. **47**, 2954
- [4] Zhu X 2005 Ph.D. thesis, Eindhoven University of Technology
- [5] Flikweert A J, Van Kemenade M, Nimalasuriya T, Haverlag M, Kroesen G M W and Stoffels W W 2006 J.Phys.D **39**, 1599
- [6] Flikweert A J, Nimalasuriya T, Groothuis C H J M, Kroesen G M W and Stoffels W W 2005, J. Appl. Phys. **98** 073301
- [7] Nimalasuriya T, Pupat N B M, Flikweert A J, Stoffels W W, Haverlag M and Van der Mullen J J A M 2006 J. Appl. Phys. **99** 053302 **see chapter 2**
- [8] Nimalasuriya T, Flikweert A J, Haverlag M, Kemps P C M, Kroesen G M W, Stoffels W W, Van der Mullen J J A M 2006 *J. Phys D: Appl Phys* **39** 2993 **see chapter 3**
- [9] Nimalasuriya T, Curry J J, Sansonetti C J, Ridderhof E J, Shastri S D, Flikweert A J, Stoffels W W, Haverlag M, Van der Mullen, J J A M 2007 J.Phys.D **40**, 2831 **see chapter 6**
- [10] Nimalasuriya T, Thubé G M, Flikweert A J, Haverlag M, Kroesen G M W, Stoffels W W, Van der Mullen 2007, J.Phys.D 2007 **40** 2839 **see chapter 4**
- [11] Stoffels W W, Baede A H F M, Van der Mullen J J A M, Haverlag M and Zissis G 2006 Meas. Sci. Technol. **17** N67
- [12] Cornelis R 2006, MSc Thesis, X-Ray Absorption measurements and measurement simulations on HID lamps, Eindhoven University of Technology
- [13] Denisova N, Haverlag M, Ridderhof E J, Nimalasuriya T, Van der Mullen J J A M, to be submitted
- [14] Nimalasuriya T, Zhu X, Ridderhof E J, Haverlag M, Denisova N, Stoffels W W and Van der Mullen, *submitted for publication in JPhysD*. **see chapter 7**
- [15] Bartels H Z 1950 Z. Phys. **127** 243
- [16] Karabourniotis D 1983 J. Phys D **16** 1267
- [17] Kettlitz M, Wendt M, Schneidenbach H and Krylova O 2007 J. Phys D **40**3829

- [18] Fohl T, Kramer J M and Lester J E 1993 J Appl Phys 73 46
- [19] Curry J J, Sakai M and Lawler J E 1998 J. Appl. Phys. **84**, 3066
- [20] Hansen P C, The L-curve and its use in the numerical treatment of inverse problems
- [21] Pretzler G, A New Method for Numerical Abel-Inversion, Z. Naturforsch. 46a, 1991, pages 639-641
- [22] Thermodynamic Database Philips Lighting
- [23] Van den Hoek W J, Van den Nieuwenhuizen H C M, Stormberg H P, *the estimation of additive densities in metal-halide arcs from self-reversed emission line contours*, (Philips Eindhoven 1982)
- [24] database for x-ray absorption cross-sections, <http://www.csrii.iit.edu/periodic-table.html>
- [25] Nimalasuriya T, Beks M L, Flikweert A J, Haverlag M, Stoffels W W, Kroesen G M W, Van der Mullen J J A M, *to be submitted to Special Edition of J.Phys D. see chapter 5*
- [26] Johnston C W 2003 PhD Thesis *Transport and equilibrium in molecular plasma's: the sulfur lamp* Eindhoven University of Technology.

Conclusions

9.1 Introduction

The aim of the research described in this thesis was to obtain a better understanding of the transport phenomena of the chemically complex plasma of the metal halide lamp. By comparing the model results to the experiments we can gain insight into the complex transport phenomena in the metal-halide lamp. The experiments verify the model results, whereas the model gives insight and aids the interpretation of the experimental results. The experiments at micro-gravity are part of a poly-diagnostic study [1–9] of the metal-halide lamp. The individual results of the experiments also validate each other and give insight into the plasma processes. This thesis has dealt with the experimental investigations. In this chapter we give an overview of the conclusions of the different chapters. This can be divided into three parts, the optical emission spectroscopy measurements (OES), the comparison to the model, and the x-ray spectroscopy experiments. The LTE (Local Thermal Equilibrium) assumption is investigated by comparing the results from the x-ray spectroscopy and the emission spectroscopy, and by combining the latter results at micro-gravity with the results from the numerical model. We conclude this chapter with a general outlook.

9.2 Overview of the thesis

9.2.1 Optical emission spectroscopy

The optical emission spectroscopy (OES) experiments can be divided into two types of diagnostics. The first type of measurement was done using a 1-m Czerny-Turner monochromator under normal gravity conditions. The monochromator was used to measure the transitions of Hg and a large number of transitions for Dy for a majority of the visible range (between 400 and 700 nm). The second type of measurement was done using an Echelle spectrometer at gravity conditions ranging from micro-gravity up to hyper-gravity. The Echelle spectrometer was chosen because it is small, compact and does not contain

moving parts. Several interference filters were used for wavelength selection, in this way a few transitions of atomic and ionic Dy, and atomic Hg have been measured. In both cases the lines were measured along the line of sight, yielding a profile of the line intensity as a function of lateral position for each line. This profile was then Abel inverted so that the radial intensity profile was obtained.

The OES measurements showed the distribution of atomic and ionic states of Dy and atomic Hg. Both the lateral and radial profile of the individual lines show that there is a clear separation between the ionic and atomic regions of Dy. The Dy atoms have a hollow density profile whereas in the centre the atoms are ionised. The Dy ions also show a dip in the centre, there Hg ions are found to dominate. In the outer parts of the lamp molecules dominate.

Absolute line intensity measurements at normal gravity

As reported in chapter 2, a myriad of Dy lines were measured with the 1-m Czerny-Turner monochromator, a total of 39 of these lines were chosen. From these atomic and ionic Dy lines, the radial intensity profiles were determined. With the help of these atomic and ionic Dy intensity profiles we constructed the radially resolved Atomic State Distribution Function (ASDF). From these ASDFs several quantities were determined as function of radial position, such as the (excitation) temperature, the ion ratio Hg^+/Dy^+ , the electron density, the ground state and total density of Dy atoms and ions. The density of the Dy atoms is found to be 10^{20} m^{-3} for a lamp burning at 100W. The ion ratio Hg^+/Dy^+ showed that in the centre Hg ions dominate. The axis temperature measured with atomic Dy, ionic Dy and Hg showed an axis temperature of 6000 K within the 10 % error margin. The ASDF of Dy^+ also showed that LTE is no longer valid in the outer regions of the discharge.

MH lamps at gravity conditions ranging from 0-*g* to 10-*g*

The investigated lamp was designed such that axial segregation is at its maximum value under normal gravity conditions. In order to study the roles of the competing processes of convection and diffusion separately, the lamp was subjected to extreme gravity conditions. Two extreme conditions were created during the parabolic flight experiment, i.e. no convection (micro-gravity) and enhanced convection (2-*g*). At micro-gravity there is no convection, so that the segregation is only present in radial direction. At hyper-gravity, convection dominates and axial segregation can be varied depending on different gravity conditions. Because the gravity conditions could not be maintained long enough during the parabolic flights for the discharge to stabilise, and because it is of interest to increase the dynamic range of the hyper-gravity experiments, the lamp was placed in the international space station (ISS) and the centrifuge. The results from the extended micro-gravity conditions are reported in chapter 3. The centrifuge can increase acceleration up to 10*g*, the results of the experiments done under these conditions are reported in chapter 4.

Microgravity

An Echelle spectrometer was used for the optical emission spectroscopy (OES) measurements at prolonged micro-gravity conditions at the international space station (ISS). At 0- g there is no convection, only diffusion. The webcam images taken at the ISS showed, as expected, that there is no axial segregation, only radial.

The atomic Hg line was calibrated and in combination with the vapour pressure used to calculate the radial temperature profile. By combining the radial temperature profile with the calibrated radial intensity profile of the additive, the absolute radial density profile of the total atomic and ionic density of Dy was obtained. Lamps containing Dy showed contraction of the arc, which increased for higher powers. Comparison between 0- g and 1- g showed that there is more radial segregation at 0- g . This is because of the absence of convection at 0- g , which promotes mixing of the species. The temperature profile of a lamp containing both Hg and Dy showed an axis temperature of 6100K at 1- g , which is comparable to the axis temperature at 0- g within the error margin. The difference between 1- g and 0- g of the radial temperature, intensity and density profiles, decreased for high powers. Atomic density for a lamp operating at 110 W at 1- g is found to be about 10^{20} m^{-3} at the centre of the lamp, which is comparable to what is found by the absolute line intensity measurements done in chapter 2.

Hypergravity

The setup, comparable to the one used at the ISS, was placed on a centrifuge. This centrifuge accelerated the OES setup and lamp between 1 and 10- g , thereby enhancing the role of convection.

Several transitions of atomic and ionic Dy, and atomic Hg have been measured at different lateral positions from which we obtained atomic and ionic Dy and atomic Hg intensity profiles. These profiles were determined at different axial positions in the lamp. Both ionic and atomic Dy profiles showed, for burners with low aspect ratio that at higher g , the amount of Dy decreases near the bottom and increases near the top.

Atomic lateral profiles of Dy at different axial positions in the lamp were used for the calculation of Fischer's axial segregation parameter. The theoretical model of the Fischer curve, which shows the axial segregation parameter as a function of convection, was verified along the full range by measuring lamps of different filling and geometry. Moreover, the radial temperature profile of the arc for the different gravitational accelerations was determined. The temperature profile near the lower electrode, showed contraction at high g . This is caused by the increase of convection.

9.2.2 Comparison with the numerical model

The numerical simulations done by M.L Beks with Plasimo were compared to the experimental results in order to verify the results of the model and to gain a better understanding of the transport processes, which is the final goal of the overall project. A start with the

validation was made in chapter 5 where the results of the model were compared to the micro-gravity experiments. As there is no convection this allows for easier modelling.

The model and experiment are in reasonable agreement with each other. The cross-section for the elastic collision between the Dy ion and Hg atom was approximated by the Langevin cross-section. The sensitivity of the plasma properties for this cross-section was investigated. The temperature profile is in agreement and not too sensitive for the choice of cross-section. Dy atom profiles showed an abrupt transition between atom and molecule for both model and experiment. The comparison between the experiment and model results for the Dy atom concentration showed that the model predicts too much radial segregation. Both the atom and ion distribution is very sensitive to the choice of cross-section for the collision between the Dy ion and Hg atom. The ratio Hg^+/Dy^+ was found to be extremely sensitive for the cross-section of the elastic interaction $\sigma(Hg, Dy^+)$ between Dy^+ and Hg atom. The sensitivity analysis reveals that equating $\sigma(Hg, Dy^+)$ to a value that is 10% higher than the Langevin cross-section is the best choice.

There is a clear discrepancy between experiment and the LTE-based model for the Dy ion density profiles. The experiment shows that the Dy ion density decreases much more rapidly. Further analysis into the Boltzmann-Saha balance suggested that after $r/R > 50\%$ LTE is no longer valid.

9.2.3 X-ray diagnostics for MH lamps

It is desirable to use a technique that can penetrate all regions of the lamp and can directly measure the absolute density of the detected element. It is because of these advantages that two different x-ray diagnostic techniques were used. X-ray induced fluorescence (XRF) is capable of directly measuring all elemental densities of the arc constituents so no Abel inversion is needed. The data-analysis is therefore much less complicated. Unfortunately the spatial resolution of XRF is not very high. The experiment and results are discussed in chapter 6. X-ray absorption measures the Hg density, combined with the wall temperature and the ideal gas law $p = nkT$, the temperature profile was obtained. XRA has much higher spatial resolution compared to XRF. A high spatial resolution is needed near the wall because of the steep temperature gradients. However, in contrast to XRF, the data-analysis XRA is much more complex. The x-ray absorption of Hg are described in chapter 7 and 8. The latter deals with the measurement of a commercial lamp.

X-ray induced fluorescence

Synchrotron radiation from the Advanced Photon Source at the Argonne National Laboratory was used to excite fluorescence in the arc constituents. Elemental densities of Hg, Dy and I were measured. In order to study the segregation effect the elemental concentration of I and Dy were determined.

Significant radial and axial segregation of Dy were observed. Elemental I is seen to exhibit considerably less axial and radial segregation. Some aspects of the observed radial segregation are compatible with a simplified analytical fluid model describing two main

transition regions in the radial coordinate. The first transition occurs in the region where DyI_3 molecules are in equilibrium with neutral Dy atoms. The second transition occurs where neutral Dy atoms are in equilibrium with ionized Dy. The segregation parameter of Fischer for Dy and the Dy elemental density is in agreement with Laser Absorption Spectroscopy (LAS) measurements done by Flikweert. The LAS measurements also reported 10^{21} m^{-3} at the centre for a lamp burning at 151 W, which is comparable to the 10^{21} m^{-3} measured with XRF at the centre for a lamp operating at 145 W; both were measured at the midplane.

X-ray absorption

The experiment and data-analysis devised by X. Zhu was improved. Three phenomena were investigated that have an effect on the final outcome of the experiment. The ideal Tikhonov parameter was found and the Abel inversion was improved by increasing the number of polynomial terms.

Beam-hardening, which occurs when the source is not monochromatic, was studied and found to be negligible within our error margin. The scatter of the x-rays on quartz was studied experimentally and was found to be significant. By incorporating the scatter-correction, and optimising the regularised Abel inversion, we found that the axis temperature is 6000 K for the lamp containing DyI_3 . This is in agreement with the optical emission spectroscopy studies mentioned above and in chapters 2,3 and 4.

Two sets of measurements were done. The first set included two lamps both containing quartz burners, with and without salt (DyI_3). This and the investigations described above were presented in chapter 7.

Chapter 8 deals with x-ray absorption measurements of 4 ceramic lamps with different fillings, namely, DyI_3 , TlI , NaI and a commercial lamp containing a mixture of these three. The commercial metal-halide lamp temperature profile combines the effects of its various salt constituents. These are mainly Dy, Na and Tl. Dy causes the profile to contract, whereas Na tends to broaden the profile, cancelling the contraction caused by the Dy. Tl has a pronounced effect on the shape of the temperature profile of a pure Tl lamp. The temperature profiles clearly show a region where the atoms associate into molecules, and vice versa, which results in the presence of 'shoulders' in the temperature profile. A reproducibility study pointed out that the error in axis temperature is about 8 %, while for the profile shape an error around 1.6% was found.

9.2.4 LTE validation

A system is said to be in Local Thermal Equilibrium (LTE) when two conditions are fulfilled, 1) all material particles (species) have the same temperature, 2) The distribution of atoms, ions and molecules over internal states obey the laws of equilibrium statistical mechanics. This is of particular importance for the numerical model. If the LTE assumption is justified this can substantially simplify the numerical model. It is therefore of interest to verify the validity of the LTE assumption. Optical emission spectroscopy measured the

excitation temperature. Assuming most of the excitation occurs by electron collision and that transport phenomena are negligible, we can presume that the excitation temperature equals the electron temperature.

We used x-ray absorption of the Hg density in the lamp to determine the gas temperature. Both the electron (excitation) and gas temperature is found to be around 6000 K. This would suggest that the LTE assumption in these lamps is valid within the experimental error of the methods. However, both the ASDF of the Dy ion and the comparison between numerical model and experiment revealed that in the outer regions the LTE assumption is no longer justified. However, this departure of LTE only has a limited effect on the main plasma parameters such as the temperature and the electron density. It will also not substantially change the spectrum emitted by the plasma. This means that using an LTE model is justified to describe the phenomena in this type of lamp.

9.3 General outlook

A large amount of data has been collected using both optical and x-ray diagnostic techniques. The plasma parameters, namely density and temperature, were investigated under different gravity conditions and with two types of x-ray diagnostics. The information gathered can be seen as a basic data set for the validation of numerical models. Also, the data was used to cross-compare the results of the various experiments. Insight into the effect of the metal iodides on the arc, and the diffusion and convection processes was gained.

There are other experimental studies of the metal-halide lamp that are either ongoing or of interest to pursue in the future. Laser Absorption Spectroscopy (ILAS) measurements at gravity conditions of varying degree is currently performed by Flikweert [14]. ILAS measures the ground state density of the Dy atom. Thomson scattering [10, 11], which allows for direct measurement of the electron temperature and density can help shed light on the validity of the LTE assumption, which is of vital importance for the model. It would be interesting to investigate the role of the molecules with emission spectroscopy or Laser Induced Fluorescence (LIF) [12, 13]. Finally, time-resolved measurements have shown interesting effects such as cataphoresis, which require further study.

The final goal would be to obtain a numerical model, so that the metal-halide lamp can be designed to function most efficiently, with more stability, longer lifetime and better colour rendering. The results presented in this thesis here are indispensable for the development and testing of such a model.

Bibliography

- [1] Zhu X 2005 Ph.D. thesis, Eindhoven University of Technology
- [2] Flikweert A J, van Kemenade M, Nimalasuriya T, Haverlag M, Kroesen G M W and Stoffels W W 2006 *J.Phys.D* **39**, 1599
- [3] Flikweert A J, Nimalasuriya T, Groothuis C H J M, Kroesen G M W and Stoffels W W 2005, *J. Appl. Phys.* **98** 073301
- [4] Nimalasuriya T, Pupat N B M, Flikweert A J, Stoffels W W, Haverlag M and van der Mullen J J A M 2006 *J. Appl. Phys.* **99** 053302 **see chapter 2**
- [5] Nimalasuriya T, Flikweert A J, Haverlag M, Kemps P C M, Kroesen G M W, Stoffels W W, van der Mullen J J A M 2006 *J. Phys D: Appl Phys* **39** 2993 **see chapter 3**
- [6] Nimalasuriya T, Curry J J, Sansonetti C J, Ridderhof E J, Shastri S D, Flikweert A J, Stoffels W W, Haverlag M, van der Mullen, J J A M 2007 *J.Phys.D* **40**, 2831 **see chapter 6**
- [7] Nimalasuriya T, Thubé G M, Flikweert A J, Haverlag M, Kroesen G M W, Stoffels W W, van der Mullen 2007, *J.Phys.D* 2007 **40** 2839 **see chapter 4**
- [8] Nimalasuriya T, Zhu X, Ridderhof E J, Haverlag M, Denisova N, Stoffels W W and van der Mullen, *submitted for publication in JPhysD*. **see chapter 7**
- [9] Nimalasuriya T, Zhu X, Ridderhof E J, Haverlag M, Denisova N, Stoffels W W and van der Mullen, *submitted for publication in JPhysD, special issue*. **see chapter 8**
- [10] Zhu X, De Vries N, Kieft E R, van der Mullen J A M, Haverlag M 2005 *J. Phys D*, **38** 1923
- [11] De Vries N, Zhu X, Kieft E R, van der Mullen J A M 2005 *J. Phys D* **38** 2778
- [12] Yang X, Lin M, Zou W, Li Y, Zhang B 2003 *Phys. chem. chem. phys.* **5**, 4786
- [13] Mulders H C J, Stoffels W W, to be submitted
- [14] Flikweert A J, Nimalasuriya T, Stoffels W W, Kroesen G M W 2007, *PSST* **16** 606

Summary

Transport phenomena in metal-halide lamps, a poly-diagnostic study

Worldwide about 20% of all electricity is used for lighting. It is therefore of great interest to develop a lamp that has high efficacy, good colour rendering and long lifetime. The metal-halide lamp is a gas discharge lamp that meets all these demands. Unfortunately there are still issues with this lamp that need to be dealt with in order to maximize its full potential.

One of these issues deals with the orientation dependence of the light-technical properties, such as colour reproduction and efficiency. Moreover, when the lamp is operated vertically, it can become unstable and is non-uniform in colour. The additive metals in the metal-halide lamp are not evenly distributed over the lamp, they are segregated. In this case, most of the metals can be found at the bottom of the lamp. This results in poor colour rendering and a decreased efficiency. It is therefore of interest to gain a better understanding of the complex transport phenomena so that the design of the metal halide lamp can be improved. A good numerical model can help achieve this goal.

The objective of this thesis was to accumulate a large amount of data under a variety of conditions so that the numerical model can be validated and insight into the complex transport phenomena can be improved. It is however currently beyond our capabilities to fully understand and model a commercial metal-halide lamp with a complex shape and chemistry. Therefore, the measurements have been performed on a reference lamp with a simple geometry and chemistry. The lamp that was mainly studied in this thesis contained only one salt, namely DyI_3 . The last chapter of this thesis is devoted to the study of a commercial lamp.

A poly-diagnostic approach was used to investigate the plasma properties of the metal-halide lamp. Optical emission spectroscopy (OES) was used to obtain information of the wavelength spectrum. Compact and robust setups were used under extreme gravity conditions. X-ray diagnostics that were applied were x-ray absorption spectroscopy (XRA) and x-ray induced fluorescence (XRF). X-ray absorption measures the Hg density at high spatial resolution allowing for an accurate measurement of the heavy-particle temperature.

The Advanced Photon Source at the Argonne National Laboratory was used to excite XRF in the metal-halide arc. XRF allows for direct measurement of the arc constituents, Dy, I and Hg. The spatial distribution of the additives and Hg were determined and from

these the concentration profiles of the additives. These showed significant radial and axial segregation for Dy and much less for I.

The OES measurements showed the distribution of the excited states of Dy and Hg. Absolute line intensity measurements were done using a 1-m Czerny Turner monochromator which was used to measure a large part of the visible spectrum. From the radially resolved spectral lines an Atomic State Distribution Function (ASDF) was constructed. From the ASDF several quantities were determined as a function of radial position, such as the (excitation) temperature, the ion ratio Hg^+/Dy^+ , the electron density, the ground state and total density of Dy atoms and ions.

Both the lateral and radial profile of the individual lines show that there is a clear separation between the ionic and atomic regions of Dy. The Dy atoms have a hollow density profile whereas in the centre the atoms are ionised. In the outer parts of the lamp molecules dominate. Ionic Hg is found in the centre of the lamp, where the temperature is highest. The ion ratio Hg^+/Dy^+ showed that the Hg ion dominates in the centre of the lamp.

Prolonged micro-gravity conditions were obtained at the international space station (ISS). At 0-g there is no convection, only diffusion. The webcam images taken at the ISS showed, as expected, that there is no axial segregation, only radial. Because the micro-gravity environment eliminates convection, it is easier to model. The density distributions, concentration profiles and temperature profiles measured at micro-gravity were compared to the model. The model and experiment were in reasonable agreement with each other. The comparison has given us further insight in the various phenomena, the model has guided the interpretation of the experimental results with respect to the deviation of LTE whereas the experiment has indicated which set of elementary parameters is essential for the theoretical description of the lamp as a whole.

When the lamp was placed in a centrifuge and subjected to hyper-gravity up to 10 g , the species are mixed by the increased convection, causing the Dy to be better distributed over the lamp. Atomic lateral profiles of Dy at different axial positions in the lamp were used for the calculation of Fischer's axial segregation parameter. The theoretical model of the Fischer curve, which shows the axial segregation parameter as a function of convection, was verified along the full range by measuring lamps of different filling and geometry.

We used XRA of the Hg density in the lamp to determine the gas temperature, it was found that scattering of the x-rays on the lamp materials have a profound effect. The electron temperature measured by OES and gas temperature measured by XRA shows a central axis temperature of 6000 K. This would suggest that the LTE assumption in these lamps is justified. However, a more in depth study showed that in the outer regions of the discharge a deviation of LTE occurs. Nevertheless, it is expected that the LTE deviation will not have a major impact on the determination of the main plasma parameters.

Related publications

Journals

X-ray induced fluorescence measurement of segregation in a DyI₃ÚHg metal-halide lamp
Nimalasuriya T, Curry J J, Sansonetti C J, Ridderhof E J, Shastri S D, Flikweert A J, Stoffels W W, Haverlag M and van der Mullen J J A M 2007 Journal of Physics D **40** 2831

Axial segregation in metal-halide lamps under gravity conditions ranging from 1g to 10g
Nimalasuriya T, Thubé G M, Flikweert A J, Haverlag M, Kroesen G M W, Stoffels W W and van der Mullen J J A M 2007 Journal of Physics D **40** 2839

X-ray absorption of the Hg density distribution in a metal-halide lamp
Nimalasuriya T, Zhu X, Ridderhof E J, Haverlag M, Denisova N, Stoffels W W and van der Mullen J J A M 2007 submitted for publication in Journal of Physics D

Metal-halide lamps in micro-gravity, experiment and model
Nimalasuriya T, Beks M L, Flikweert A J, Stoffels W W, Haverlag M, Kroesen G M W and van der Mullen J J A M 2007 submitted for publication in Journal of Physics D, Special Issue

X-ray absorption of the Hg density in a commercial lamp
Nimalasuriya T, Zhu X, Ridderhof E J, Beks M L, Haverlag M, Denisova N, Stoffels W W, van der Mullen J J A M 2007 submitted for publication in Journal of Physics D, Special Issue

Optical emission spectroscopy of metal-halide lamps: radially resolved atomic state distribution functions of Dy and Hg
Nimalasuriya T, Pupat N B M, Flikweert A J, Stoffels W W, Haverlag M and van der Mullen J J A M 2006 Journal of Applied Physics. **99** 053302

Metal halide lamps in the international space station ISS
Nimalasuriya T, Flikweert A J, Haverlag M, van der Mullen J J A M, Kemps P C M, Kroesen G M W, Stoffels W W and van der Mullen J J A M 2006 Journal of Physics D

Axial segregation in high intensity discharge lamps measured by laser absorption spectroscopy,

Flikweert A J, Nimalasuriya T, Groothuis C H J M, Kroesen G M W and Stoffels W W 2005 Journal of Applied Physics **98** 073301

Axial segregation in metal-halide lamps under varying gravity conditions during parabolic flights

Flikweert A J, van Kemenade M, Nimalasuriya T, Haverlag M, Kroesen G M W and Stoffels W W 2006 Journal of Physics D **39**, 1599

Imaging Laser Absorption Spectroscopy of the metal-halide lamp in a centrifuge (1-10g)

Flikweert A J, Nimalasuriya T, Stoffels W W and Kroesen G M W 2007 Plasma Sources Science and Technology **16** 606

Colour segregation in metal-halide lamps: experimental and numerical investigations

Brok W J M, Nimalasuriya T, Hartgers A, Beks M L, Haverlag M, Stoffels W W, van der Mullen J J A M 2006 High temperature materials processing **10** (4) 571-582

Metal halide lamps: gravitational influence on color separation

Stoffels W W, Flikweert A J, Nimalasuriya T, van der Mullen J J A M, Kroesen G M W and Haverlag M 2006 Pure and Applied Chemistry **78** (6) 1239-1252

Discharges for lighting

Stoffels W W, Nimalasuriya T, Flikweert A J and Mulders H C J, accepted for publication in Plasma Physics and Controlled fusion.

X-ray absorption tomography of a high-pressure metal-halide lamp with a bended arc due to Lorentz-forces

Denisova N, Haverlag M, Ridderhof E J, Nimalasuriya T and van der Mullen J J A M accepted for publication in Journal of Physics D.

Invited Lectures

Optical and X-ray Diagnostics of Metal-Halide Lamps Nimalasuriya T, Thubé G M, Pupat N B M, Curry J J, Sansonetti C J, Ridderhof E J, Flikweert A J, Stoffels W W, Haverlag M, Kroesen G M W and Van der Mullen J J A M, COST 529 Meeting, Mierlo, The Netherlands, March 30-April 2 2006

Conference contributions

Radial and axial segregation in metal-halide lamps under gravity conditions from 0-10g, Nimalasuriya T, Thubé G M, Pupat N B M, Curry J J, Sansonetti C J, Ridderhof E J, Flikweert A J, Stoffels W W, Haverlag M, Kroesen G M W and Van der Mullen J J A M, 11th international symposium on the science and technology of light sources May 20th-24th 2007, Shanghai, China, oral contribution

Radial Segregation and helical instabilities in metal-halide HID lamps studied under micro-gravity conditions in the international space station
Nimalasuriya T, Haverlag M, Keijser R, Kuipers A, Stoffels W W, Van der Mullen J J A M and Kroesen G M W
11th international symposium on the science and technology of light sources May 20th-24th 2007, Shanghai, China, poster contribution

X-ray induced fluorescence measurement of the additive and Hg densities in a metal-halide lamp
Nimalasuriya T, Curry J J, Sansonetti C J, Ridderhof E J, Flikweert A J, Stoffels W W, Haverlag M and Van der Mullen J J A M
11th international symposium on the science and technology of light sources May 20th-24th 2007, Shanghai, China, poster contribution

Emission Spectroscopy of Metal Halide Lamps under Normal and Microgravity conditions
Nimalasuriya T, Flikweert A J, Stoffels W W, Haverlag M, Kroesen G M W, Van der Mullen J J A M, 7th Euregional WELTPP, Rolduc (Kerkrade), Netherlands, poster contribution (2004)

Additive density distributions and temperature profiles of metal-halide lamps in the International Space Station
Nimalasuriya T, Flikweert A J, Stoffels W W, Haverlag M, Kroesen G M W, Van der Mullen J J A M, 8th Euregional WELTPP, Rolduc (Kerkrade), Netherlands, oral contribution (2005)

Emission Spectroscopy of Metal Halide Lamps under Normal and Microgravity conditions
Nimalasuriya T, Flikweert A J, Stoffels W W, Haverlag M, Kroesen G M W, Van der Mullen J J A M, XVII NNV/CPS-Symposium on Plasma Physics and Radiation Technology Lunteren, Netherlands, poster contribution (2005)

Absolute line intensity measurements of the density distribution of Dy in a metal-halide lamp
Nimalasuriya T, Pupat N B M, Flikweert A J, Stoffels W W, Haverlag M, Van der Mullen J J A M, XXVIII ICPIG 2005, Veldhoven, Netherlands, poster contribution (2005)

X-ray induced fluorescence measurement of the density distribution of Dy and Hg in a metal-halide lamp

Nimalasuriya T, Curry J J, Sansonetti C J., Ridderhof E J, Flikweert A J, Stoffels W W, Haverlag M, Van der Mullen J J A M, XXVIII ICPIG 2005, Veldhoven, Netherlands, poster contribution (2005)

Additive Density distributions and Temperature profiles of Metal-Halide lamps from zero to hyper-gravity

Nimalasuriya T, Thubé G M, Flikweert A J, Stoffels W W, Haverlag M, Kroesen G M W, Van der Mullen J J A M, XVIII NNV/CPS-Symposium on Plasma Physics and Radiation Technology Lunteren , Lunteren, Netherlands, oral contribution (2006)

Additive density distributions and temperature profiles of metal-halide lamps measured in the International Space Station and a centrifuge

Nimalasuriya T, Thubé G M, Flikweert A J, Stoffels W W, Haverlag M, Kroesen G M W, Van der Mullen J J A M, , ESCAMPIG XVIII Lecce, Italy, poster contribution (2006)

Miscellaneous

Women in Science

Front of international ad campaign

12 September 2005

Future lamps in space

Lecture, Publieksdag Technische Universiteit Eindhoven

02 October 2005

Steek je licht op in de ruimte

Interview, Eindhovens Dagblad EDTV, www.eindhovensdagblad.nl/video

24 May 2006

Acknowledgements

I have had the privilege to work with great people.

First, I would like to thank Joost van der Mullen. Thank you for giving me the opportunity to work with you and for letting me profit from your insight, knowledge and experience. I have enjoyed our many discussions which have allowed me to greatly improve my work.

Winfred Stoffels, thanks for all your help and encouragement, for sharing with me your insight, and for showing me how to navigate in the field of science.

Marco Haverlag, thank you for sharing with me your vast knowledge of lamps and for infecting me with your enthusiasm for lamp physics.

Gerrit Kroesen, thank you for your help and for giving me the opportunity to participate in spectacular projects.

I would like to thank Dimitrios Karabourniotis, Antonio Gamero and Leo van IJzen-doorn for taking place in my committee.

I would like to thank John Curry, for introducing me to the fascinating world of x-ray induced fluorescence and giving me the opportunity to do measurements at the Advanced Photon Source of the Argonne National Laboratory. Also thanks to Craig Sansonetti for helping us.

All members of EPG while I was in the group, thanks for the *gezelligheid*, I have always enjoyed the good atmosphere that you guys created. I would especially like to thank the following members:

Xiaoyan Zhu (for the XRA project), Arjan Flikweert (for the centrifuge project), Wouter Brok (for all your help), Mark Beks (for our fruitful discussions), Bart Broks, Hjalmar Mulders (especially for anything related to cars that won't start), Ingrid Kieft, Sander Nijdam, Erik Wagenaars. I would like also like to thank the following people,

The following students for contributing to my work:

Antonio Jurado, Nicolas Papat, Gaelle Thubé, Rob Cornelis, Pedro Almeida (PhD Student), Peter Pasmans, Koen Kuiper.

The people who have taken such good care of my baby boy, de Knorretjes, Marylin, Truus and Marjolein.

Rina Boom, for all your help, I'll miss our talks.

Tanja Briels, for the good times, the moral support, and sharing the unique experience of being pregnant at the same time.

The following technicians, without whom these experiments in physics would not have been possible.

Loek Baede, Charlotte Groothuis, Huib Schouten, Rob de Kluijver and the rest of the GTD, and especially Evert Ridderhof, thank you for all your help and assistance, I can always count on you.

People who made lamps needed for all the experiments: J. Peeraer en J. Heuts (Philips Turnhout), en F. Vermeulen, F. Meeuwsen, W. Dekkers (Philips Lighting)

All my friends (you know who you are!). My family, both nearby and far away, especially my parents.

Finally, I would like to thank my caring husband Jorn Bakker, *mijn lieve held*, whose love and support has been of immeasurable value, and our beloved son, Roshan David Bakker, who makes the sun shine everyday.

Curriculum vitae

13 June 1975

Born in Amsterdam, The Netherlands.

1987 – 1995

Petrus Canisius College, Alkmaar. *Diploma obtained in 1993*

Cornelis Drebbel College, Alkmaar. *Additional subjects*

1995 – 2004

M.Sc. in Applied Physics at Eindhoven University of Technology.

◇ Traineeship at the Plasma and Materials Processing group of the Department of Applied Physics, Eindhoven University of Technology. Subject: *Study of carbon films deposited with a cascaded arc*, supervised by dr. A. de Graaf and prof. dr. ir. M.C.M van de Sanden.

◇ Traineeship at Philips Research, Eindhoven. Subject: *Contamination effects related to EUV production*, supervised by dr.ir. J. Jonkers and prof.dr. J.J.A.M. van der Mullen.

◇ Master thesis project at the Polymer Physics group of the Department of Applied Physics, Eindhoven University of Technology. Subject: *Theory of the nucleation kinetics of nematic droplets*, supervised by dr.ir. P.P.A.M. van der Schoot and prof.dr. M.A.J. Michels.

Extracurricular activities include the founding of a classical guitar ensemble, taking part in several theatre productions and the formation of an alternative rock band.

2004 – 2007

Ph.D. at the Elementary Processes in Gas Discharges group of the Department of Applied Physics at Eindhoven University of Technology. Subject: *Transport phenomena in metal-halide lamps, a poly-diagnostic study*, supervised by dr.ir. W.W. Stoffels, prof.dr.ir. M. Haverlag and prof.dr. J.J.A.M. van der Mullen.

